



# Politecnico di Milano

---

SCHOOL OF INDUSTRIAL AND INFORMATION ENGINEERING  
Department of Aerospace Science and Technology  
Master Degree in Space Engineering

MASTER DEGREE THESIS

## Self-sensing inertial actuators for vibroacoustic plate control: design, analysis and testing

Supervisor  
**Prof. Lorenzo DOZIO**

Candidate  
**Sebastiano Bertini**  
Matr. 928299

---

Academic Year 2020-2021



# Contents

- 1 Introduction** **1**
- 1.1 Motivation of the work . . . . . 1
- 1.2 Aim of this thesis . . . . . 2
- 1.3 Structure of the thesis . . . . . 4
- 2 Mathematical Models** **5**
- 2.1 Vibration speakers . . . . . 5
  - 2.1.1 Dynamics equations . . . . . 6
  - 2.1.2 State space realization . . . . . 7
  - 2.1.3 Static residualization of the electrical dynamics . . . . . 8
  - 2.1.4 Rigid base . . . . . 9
  - 2.1.5 Proof-mass acceleration response . . . . . 10
  - 2.1.6 Electrical input impedance . . . . . 12
- 2.2 Reconstruction of the velocities . . . . . 14
  - 2.2.1 Plate transverse velocity . . . . . 14
  - 2.2.2 Inertial mass velocity . . . . . 17
- 2.3 Pseudo-integrator . . . . . 18
- 2.4 Power amplifiers . . . . . 19
- 2.5 Plate Model . . . . . 19
  - 2.5.1 The Sublaminated Generalized Unified Formulation . . . . . 20
  - 2.5.2 Constitutive equations . . . . . 22
  - 2.5.3 Gradient equations . . . . . 24
  - 2.5.4 Ritz approximation . . . . . 25
  - 2.5.5 Expansion and assembly . . . . . 27

2.5.6	Equivalent single degree of freedom model . . . . .	29
2.6	SDOF plate model with one inertial actuator . . . . .	29
2.6.1	Dynamics equations . . . . .	30
2.6.2	State space realization . . . . .	32
<b>3</b>	<b>Experimental Characterization</b>	<b>35</b>
3.1	Inertial actuators: Dayton DAEX25VT-4 exciters . . . . .	35
3.1.1	Proof-mass acceleration response . . . . .	38
3.1.2	Electrical input impedance . . . . .	44
3.2	Current sensor . . . . .	46
3.3	Power amplifiers . . . . .	50
3.4	Plate . . . . .	53
<b>4</b>	<b>Sensor-actuator model: Numerical Testing</b>	<b>57</b>
4.1	Transverse plate velocity . . . . .	57
4.1.1	High frequency behaviour . . . . .	59
4.1.2	Low frequency behaviour . . . . .	67
4.1.3	Discrete realization . . . . .	70
4.1.4	S-GUF plate simulation . . . . .	74
4.2	Inertial mass velocity . . . . .	77
<b>5</b>	<b>Sensor-actuator model: Experimental Testing</b>	<b>79</b>
5.1	Control scheme . . . . .	79
5.2	Data acquisition system and real-time control . . . . .	81
5.3	Filters . . . . .	82
5.3.1	Low frequency filtering . . . . .	82
5.3.2	High frequency filtering . . . . .	85
5.4	Closed loop control . . . . .	89
5.5	Double loop control logic . . . . .	95
5.6	First order low-pass filter . . . . .	98
<b>6</b>	<b>Conclusions</b>	<b>101</b>
6.1	Future work . . . . .	102

# List of Figures

- 1.1 Vibration speaker . . . . . 2
- 2.1 Schematic representation of the lumped-parameters model of the inertial actuator, when it is attached to a flexible surface. . . . . 5
- 2.2 Schematic representation of the lumped-parameters model of the inertial actuator, when it is attached on a fixed, rigid surface. . . . . 9
- 2.3 On the left: comparison of the proof-mass acceleration response for a voltage driven actuator with complete and residualized electrical dynamics. On the right: proof-mass acceleration response for a current driven actuator. . . . . 11
- 2.4 Comparison of the electrical input impedance of an actuator when complete and residualized electrical dynamics are considered. . . . . 13
- 2.5 Schematic representation of the lumped-parameters model of the inertial actuator, when it is attached on a flexible surface. . . . . 14
- 2.6 S-GUF geometric description . . . . . 20
- 2.7 Schematic of the SDOF plate model with an installed inertial actuator. . . . . 30
- 3.1 Dayton DAEX25VT-4. . . . . 35
- 3.2 Dayton DAEX25VT-4 electrodynamic exciters: manufacturer specifications. . . . . 36
- 3.3 Scheme of the experimental setup adopted for the actuators characterization. . . . . 38
- 3.4 Proof-mass acceleration response computed from experimental data for Dayton A and B. . . . . 40
- 3.5 Comparison of the proof-mass acceleration response computed from experimental data ( $H_{aV}(j\omega)$ ) and the lumped parameters model ( $\hat{H}_{aV}(s)$ ), for Dayton A and B. . . . . 42
- 3.6 Comparison of the proof-mass acceleration response computed from experimental data ( $H_{ai}(j\omega)$ ) and the lumped parameters model ( $\hat{H}_{ai}(s)$ ), for Dayton A and B. . . . . 43

3.7	Comparison of the electrical input impedance computed from experimental data ( $H_{Vi}(j\omega)$ ) and the lumped parameters model ( $\hat{H}_{Vi}(s)$ ), for Dayton A and B. . . . .	45
3.8	Current sensor. . . . .	46
3.9	Current transducer installed on the breadboard, front and rear. . . . .	47
3.10	Hall effect current sensor generic scheme. . . . .	47
3.11	Hysteresis curve. . . . .	48
3.12	Current sensor connection scheme. . . . .	48
3.13	Current sensor sensitivity connection scheme. . . . .	49
3.14	Lepai LP-2020A+. . . . .	50
3.15	Scheme of the experimental setup adopted for the amplifiers characterization. . . . .	51
3.16	Lepai LP-2020A+. . . . .	52
3.17	Reference plate. . . . .	53
3.18	Experimental plate mode shapes. . . . .	54
3.19	Numerical plate mode shapes. . . . .	55
4.1	Comparison of the $\dot{w}_i(s)$ and $\dot{w}_v(s)$ terms. . . . .	58
4.2	Plate velocity reconstruction with different errors in the actuator parameters. . . . .	59
4.3	Bode plot of the two transfer functions for the transverse plate velocity reconstruction, both in the complete and statically residualized formulation. . . . .	60
4.4	Electrical admittance simulated for the simple SDOF plate coupled with the lumped parameters model of the inertial actuator. . . . .	61
4.5	Frequency response to the input voltage of the two terms for the transverse plate velocity reconstruction, both in the complete and statically residualized formulation. . . . .	62
4.6	Reconstructed velocity frequency response, obtained both with the complete and statically residualized formulation, compared with the real velocity of the plate. . . . .	63
4.7	Reconstructed velocity frequency response, obtained with different high frequency poles, compared with the real velocity of the plate. . . . .	66
4.8	Reconstructed velocity frequency response, obtained with different high frequency poles, compared with the real velocity of the plate, when a 1% error in the actuator's parameters is introduced. . . . .	67

4.9	Bode plot of the two transfer functions for the transverse plate velocity reconstruction, for different frequencies of the low frequency poles. . . . .	68
4.10	Reconstructed velocity frequency response, obtained with different low frequency poles, compared with the real velocity of the plate. . . . .	69
4.11	Reconstructed velocity frequency response, obtained with different low frequency poles, compared with the real velocity of the plate, when a 1% error in the actuator's parameters is introduced. . . . .	70
4.12	Comparison of the reconstructed velocity frequency response, obtained both with the modified and the original expression, with the real velocity of the plate. . . . .	75
4.13	Comparison of the velocity reconstructed with the original expression and the real transverse velocity of the plate at the actuator location. . . . .	76
4.14	Comparison of the velocity reconstructed with the modified expression and the real transverse velocity of the plate at the actuator location. . . . .	76
4.15	Comparison of the reconstructed inertial mass velocity frequency response, with the real velocity. . . . .	77
4.16	Comparison of the velocity reconstructed with the modified expression and the real velocity of the inertial mass of the control actuator. . . . .	78
5.1	Scheme of the experimental setup used for the testing of the skyhook control logic with the reconstruction of the plate velocity. . . . .	80
5.2	Velocity frequency response: comparison filtered and unfiltered, with the one obtained by pseudo-integration of the acceleration. . . . .	83
5.3	Effect of the filter cutting frequency on the transient of the velocity. . . . .	83
5.4	Effect of the filter cutting frequency on the transient of the voltage. . . . .	84
5.5	High-pass filter for current and tension. . . . .	85
5.6	Comparison of the velocity frequency response for the reconstructed plate velocity and the one obtained by pseudo-integration of the acceleration. . . . .	86
5.7	Voltage to the control actuator acquired when the control gain is zero. . . . .	87
5.8	Comparison of the velocity frequency response for the reconstructed plate velocity when voltage and current are filtered, with the velocity obtained by pseudo-integration of the acceleration. . . . .	88
5.9	Band-pass filter for current and tension. . . . .	88
5.10	Comparison of the velocity frequency response for the reconstructed plate velocity and the pseudo-integration acceleration, when the disturbance is filtered. . . . .	89

5.11	Acceleration frequency response at different control gains, when the pseudo-integration method is used. . . . .	90
5.12	Acceleration frequency response at different gains, if no filtering of current and voltage is introduced. . . . .	90
5.13	Acceleration frequency response at different gains, if band-pass filtering of current and voltage is introduced. . . . .	91
5.14	Band-pass filter transfer function. . . . .	92
5.15	Comparison of the two band-pass filter transfer function. . . . .	93
5.16	Acceleration frequency response at different gains, if the second band-pass filter for current and voltage is used. . . . .	94
5.17	Acceleration frequency response at different gains, if the second band-pass filter for current and voltage is used and if the disturbance is filtered. . . . .	94
5.18	Comparison between the real and the reconstructed transverse plate velocity in time domain. . . . .	95
5.19	Experimental setup used to test the inertial mass velocity reconstruction. . . . .	96
5.20	Acceleration frequency response for different control gains and a local gain of 5. . . . .	97
5.21	Bode plot of the band-pass filter, composed by a first order low-pass in addition to a second order high-pass. . . . .	99
5.22	Acceleration frequency response with a first order filtering of current and voltage. . . . .	99



# List of Tables

- 2.2 Pseudo-integrator parameters. . . . . 18
- 3.1 Parameters computed through the voltage driven proof-mass acceleration response approach, for both the Dayton exciters. Those on the right end of the table are assumed from the datasheet. . . . . 41
- 3.2 Parameters computed through the current driven proof-mass acceleration response approach, for both the Dayton exciters. Those on the right end of the table are assumed from the datasheet. . . . . 44
- 3.3 Parameters computed through the electrical input impedance approach, for both the Dayton exciters. Those on the right end of the table are assumed from the datasheet. . . . . 45
- 3.4 Parameters used for the real-time simulation. . . . . 46
- 3.5 Parameters computed for the two power amplifiers. . . . . 52
- 3.6 Test plate properties. . . . . 54
- 3.7 1-DOF parameters. . . . . 55
- 4.1 Approximation error of  $H_{i\text{res}}(s)$  with respect to  $H_i(s)$ . . . . . 64



# Abstract

In this thesis, a preliminary investigation on the use of a self-sensing inertial actuator to apply vibroacoustic control on flexible plates is presented. A commercially available vibration speaker, driven by a small audio amplifier, is used as a low-cost proof-mass actuator to reduce the vibration of a thin aluminum plate arranged in the laboratory. A skyhook control strategy is employed, meaning that the transverse velocity of the vibrating structure is fed back to the collocated actuator to reproduce the effect of a damper attached to a fix point in space. The control logic is digitally implemented on a standard desktop computer running a real-time software. A common way to provide the feedback signal could be to obtain the transverse velocity by integration of the plate acceleration, measured placing a small lightweight accelerometer on the bottom side of the plate, in correspondence of the inertial actuator. In this thesis it is investigated the possibility to reconstruct the plate velocity without the need of an accelerometer, therefore without the need to have accessibility to both sides of the plate. An expression for the plate transverse velocity is derived, based only on the characteristics of the actuator and having as inputs only tension and current applied to the actuator itself. This expression is tested both numerically and experimentally, firstly on a single-degree-of-freedom model of the plate, then on a full plate model and eventually on the prototype aluminum plate. Some modifications of the transfer functions for the reconstruction of the velocity are proposed and tested, in order to overcome instability problems arised during the numerical testing. Eventually a digital filtering of the electrical quantities is proposed, discussed and tested, with the aim to delay the onset of high frequency instability due to control spillover. The quality of the model of the self-sensing actuator is addressed comparing its result with the velocity computed by pseudo-integration of the plate acceleration. In the end the limits of the experimental setup are considered and some guidelines for further evaluations are drawn - among which advantages and limitations of the digital control implemented, with respect to a partially, or fully, analogical approach.



# Chapter 1

## Introduction

### 1.1 Motivation of the work

In recent years noise pollution has become more and more a topic of significant concern, partially due to the higher and higher anthropic density, and partially because people are becoming increasingly aware of the concept of vibroacoustic comfort. Recent studies have demonstrated the detrimental effect that prolonged exposure to noise source can have on both the psychological and physical health - going from nuisance and discomfort, troubled sleeping, reduced working performances and lower speech intelligibility in the least severe circumstances [1] - to hypertension, hearing deterioration and ischemic heart disease in the worst cases [2, 3].

Noise pollution affects people's everyday life, their homes, the transportation they use, their working places. Indeed residential and business buildings frequently have large window-like surfaces, often constituting the primary path for external noises, while cabin thin panels and shell structures generate acoustic vibrations inside cars, trains and aircrafts [4].

The unceasing need of relying on thinner and thinner structural elements has exacerbated the problem. The classical approach for noise and vibration reduction consists in the passive addition of mass or damping material over a large area of the radiating structure [5, 6, 7], but this is often not feasible, due to mass or volume requirements. Moreover surface treatments are usually effective in suppressing high frequency vibration, but they would require the addition of too much mass to work in the low frequency range. It is in fact in this peculiar - but not rare - conditions, in which the active vibration controls are a viable option [8]. One of the main drawbacks of active control of radiating surfaces is the fact that a suitable measure of the vibration of the structure is needed. Classically it's obtained with *collocated* accelerometers, but they often require double accessibility on the structure. It is in this context that *sensorless* or *self-sensing* actuators became an interesting solution [9, 10].

## 1.2 Aim of this thesis

The present work can be considered as a preliminary study aimed to assess the possibility to obtain a digitally implemented active vibration control, using self-sensing inertial actuators, to damp the resonance frequencies of an host structure subjected to broadband random disturbances.

This thesis follows from the work of Di Girolamo [11], who developed an active vibration control using commercial and low-cost voice-coil *vibration speakers* as proof-mass actuators.

Vibration speakers are electromechanical transducers capable of turning surfaces into loudspeakers, Figure 1.1.

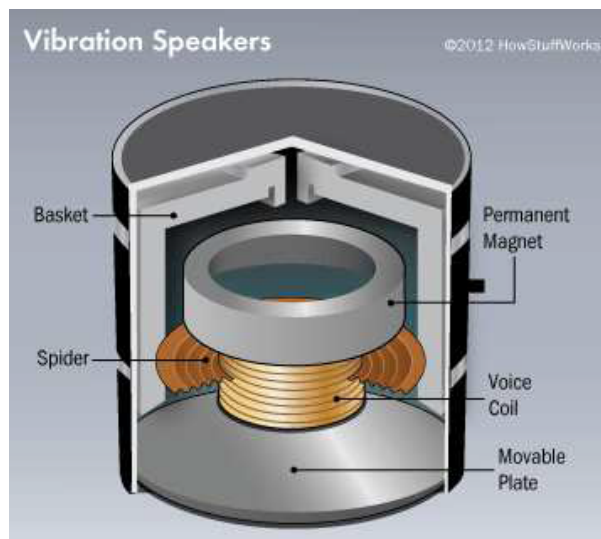


*Figure 1.1: Vibration speaker*

They are mainly composed by a base plate - to be attached to the host structure and solidal to a reversible voice coil - and a free-to-move permanent magnet. The voice coil is essentially an electromagnet that, when the actuator is powered with a time varying voltage, generates an induced magnetic field that interacts with the permanent magnet. The result of this interaction is a force acting on both components with opposite direction, such that if the permanent magnet is pushed away from the host structure, the voice coil is pushed towards it. When the driving voltage changes sign, the forces are reversed. Taking advantage of this phenomenon the vibration speaker is able to cause a vibration on the host structure - usually with the aim of transforming it into a sound radiating surface. According to this physical mechanism, the idea is to use a vibration speaker as a control device instead of a sound device, i.e., introduce vibration waves into the attached surface which can suppress the vibration induced by external noise sources, instead of generating sound.

Vibration speakers could be implemented in different strategies to achieve active vibroacoustic control, according to the specific application [12], but since the current work is focused on the response to broadband random disturbances, the most viable

option is to implement a feedback strategy. The implementation of a feedforward controller, on the contrary, would provide good effects for tonal disturbances, which can be easily characterized in advance allowing to build a reference signal well correlated to the disturbance to be controlled [13].

A feedback logic for vibroacoustic control can be implemented using only one actuator - obtaining a single-input single-output system (SISO) - or using more - obtaining a multi-input multi-output system (MIMO). In the latter case a distinction can be introduced between centralized and decentralized configuration. In the first case the control action provided by one actuator is computed taking into account the readings of all sensors, in the second case each collocated sensor/actuator pair acts independently from the others. The implementation of decentralized control strategies, for which no communication between the control units is permitted, is particularly relevant since the stability is ensured [10]. Previous works on decentralized control of flexible structures, has focused on providing active damping by velocity feedback [14, 15, 16, 17]. This strategy, often called *skyhook control* since it is equivalent of having viscous dampers attached to a fixed point in the sky [18, 17, 19, 20], leads to an unconditionally stable closed-loop system when ideal collocated sensor/actuators pairs are used. Of course in practice both sensors and actuators are far from being ideals, actuators have internal dynamics and the velocity is usually obtained from integration of acceleration measurements.

In the context of decentralized skyhook control, one of the limits is often to achieve truly collocated sensor/actuator pairs, one possibility to overcome this problem and to reduce the complexity of the installation is to use *self-sensing* actuators. A self-sensing actuator is basically a reversible electromechanical transducer which uses simultaneously the function of sensing and actuation [9]. The self-sensing actuation concept was developed by Hagood *et al.* [21] and Dosch *et al.* [22], at the end of the last century. At the beginning only PZT elements were used as self-sensing actuators, reducing implementation, complexity and cost, and achieving truly collocated control. The idea was then expanded to active vibration control on beams [23], plates [24] and vibration damping [25]. Finally in 2000, Leo *et al.* [26], extended the sensorless concept to electrodynamic loudspeakers, and Hanson *et al.* used electromagnetic actuators in 2004 [27]. It shall be pointed out that the vast majority of the works about self-sensing actuators implement fully analogical controls, this could lead to very complex system if a large decentralized self-sensing skyhook control logic has to be implemented on a real structure. It's a relatively new research area and many aspects have to be analyzed yet. This work tries to fill a hole in the present knowledge, focusing on digital implementation of a self-sensing actuator control logic for broadband noise rejection. Indeed as said before only few works have been done using a digital implementation, but for what has been found in literature, they had considered only harmonic disturbances [28]. None of them addresses the combined problem of digital implementation and random disturbances together, that, how will be seen later, give rise to peculiar complications.

## 1.3 Structure of the thesis

**1 - Introduction** A brief introduction regarding the motivation, the aim and the structure of the thesis is presented. The focus is placed on the reasons for choosing a sensorless approach, on its difficulties and on how this work is innovative.

**2 - Mathematical Models** The mathematical derivation of the models used to describe the main components of the experimental system is presented. At first, the lumped-parameters models for the vibration speaker and the audio amplifier are introduced, dynamics equations are derived and peculiar characteristics are presented. Then the core of this work - the formulation that allows to reconstruct the plate transverse velocity and the actuator proof-mass velocity from only current and voltage measurements - is derived. Finally the plate model and the S-GUF formulation on which is based is briefly presented.

**3 - Experimental Characterization** The prototype arranged in the laboratory - plate, actuators and amplifiers - is presented and the experimental characterization performed to build the mathematical models is described.

**4 - Numerical Testing** The velocity reconstruction formulation derived in Chapter 2 is tested numerically. Firstly over a simple model where the plate is described only with its first natural frequency, than on the complete flexible model of the structure, both in frequency and time domain. Some modification to the self-sensing actuator equation will be needed in order to achieve stability even in real operating conditions.

**5 - Experimental Testing** The reconstruction of the velocity derived in Chapter 4 is implemented in a real-time skyhook control logic in laboratory. Many criticalities are found, filters are designed allowing to improve the performances and the basis for future developments are layed.



# Chapter 2

## Mathematical Models

In this chapter the mathematical models used in the following are derived. Firstly the lumped-parameter model of the inertial actuator is described along with the experimental method used to obtain its parameters - then the sensor-actuator formulation is presented. For the vibrating plate two different models are used: at first an advanced sublaminate formulation, then a single degree of freedom model. Although much less complete, the latter can be useful to gain some insight on the problem under analysis. Eventually plate and actuator models are merged together, giving rise to a complete description of the problem under analysis, that can be implemented both in frequency and in time domain.

### 2.1 Vibration speakers

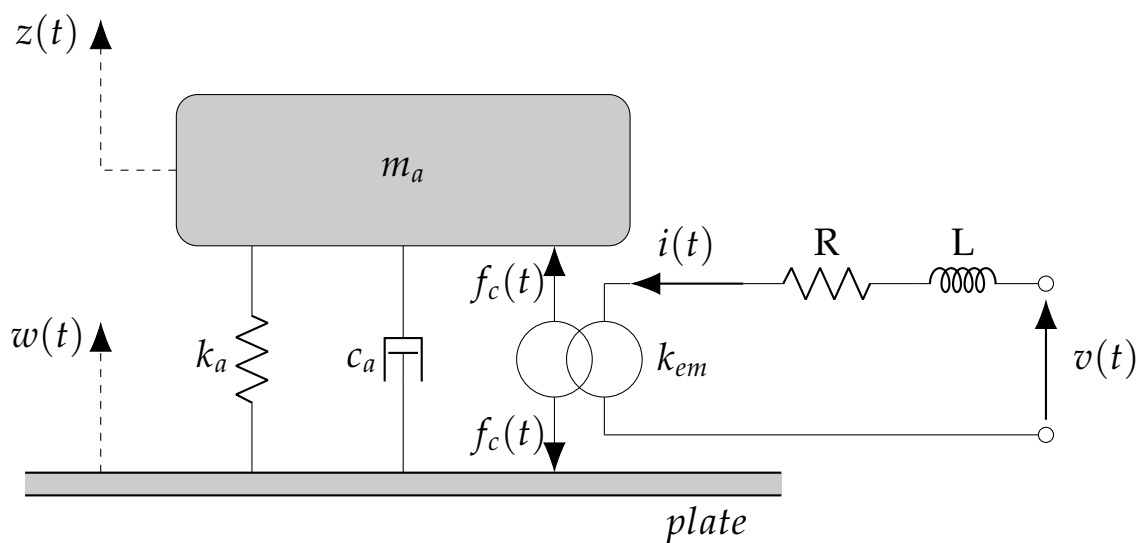


**Figure 2.1:** Schematic representation of the lumped-parameters model of the inertial actuator, when it is attached to a flexible surface.

The vibration speakers used in this work can be modeled as proof-mass electrodynamic actuators, also called inertial actuators in the following. A proof-mass actuator is a device able to provide a force on the supporting structure, by accelerating a suspended mass. Such a device can be schematized as a mass, elastically connected to the structure on which control has to be obtained, bound to move perpendicularly to the structure itself. If the movable mass - also called inertial mass in the following - is a permanent magnet, and if it is subjected to a variable magnetic field produced by a coil attached to the support structure, then the device is called an electrodynamic actuator. The magnetic field generated by the coil is proportional to the current flowing in it, such a current can be directly provided by a current source or can arise from a voltage applied by a voltage source. In the former case the actuator can be defined as *current driven*, in the latter as *voltage driven*.

A single degree of freedom lumped-parameters model is adopted to describe the electromechanical dynamics of the actuator as shown in Figure 2.1.

### 2.1.1 Dynamics equations

In this section the dynamics equations for the inertial actuator are derived in the context of the lumped-parameter approach depicted in Figure 2.1. As reported in Ref. [29], Lagrange's equations can be used for the task. The following relevant quantities are defined:

$$T^* = \frac{1}{2} m_a \dot{z}^2 \quad \text{Complementary kinetic energy} \quad (2.1)$$

$$V = \frac{1}{2} k_a (z - w)^2 \quad \text{Potential energy} \quad (2.2)$$

$$W_m^* = \frac{1}{2} L \dot{q}^2 + k_{em} (z - w) \dot{q} \quad \text{Complementary magnetic energy} \quad (2.3)$$

$$\mathcal{D} = \frac{1}{2} c_a (\dot{z} - \dot{w})^2 + \frac{1}{2} R \dot{q}^2 \quad \text{Dissipation function} \quad (2.4)$$

$$\delta W_{nc} = \delta q v \quad \text{Virtual work by non-conservative forces} \quad (2.5)$$

Where:

$m_a$	Proof mass of the actuator	[kg]
$c_a$	Damping of the actuator	[Ns m <sup>-1</sup> ]
$k_a$	Suspension stiffness of the actuator	[N m <sup>-1</sup> ]
$R$	Coil resistance	[Ω]
$L$	Coil inductance	[H]
$k_{em}$	Electromagnetic coupling factor	[NA <sup>-1</sup> ]

$q(t)$	Electric charge in the coil	[F]
$i(t)$	Electric current flowing in the coil	[A]
$v(t)$	Electric voltage source	[V]
$z(t)$	Absolute displacement of the proof mass	[m]
$w(t)$	Absolute displacement of the support structure	[m]

The Lagrangian of the system is defined as:

$$\mathcal{L} = T^* - V + W_m^* = \frac{1}{2}m_a\dot{z}^2 - \frac{1}{2}k_a(z - w)^2 + \frac{1}{2}L\dot{q}^2 + k_{em}(z - w)\dot{q} \quad (2.6)$$

The Lagrange's equations read:

$$\frac{d}{dt} \left( \frac{\partial \mathcal{L}}{\partial \dot{z}} \right) - \frac{\partial \mathcal{L}}{\partial z} + \frac{\partial \mathcal{D}}{\partial \dot{z}} = Q_z \quad (2.7)$$

$$\frac{d}{dt} \left( \frac{\partial \mathcal{L}}{\partial \dot{q}} \right) - \frac{\partial \mathcal{L}}{\partial q} + \frac{\partial \mathcal{D}}{\partial \dot{q}} = Q_q \quad (2.8)$$

Leading to the following dynamics equations:

$$\begin{cases} m_a\ddot{z}(t) + c_a[\dot{z}(t) - \dot{w}(t)] + k_a[z(t) - w(t)] - k_{em}\dot{q}(t) = 0 \\ L\ddot{q}(t) + R\dot{q}(t) + k_{em}[\dot{z}(t) - \dot{w}(t)] = v(t) \end{cases} \quad (2.9)$$

That can be rewritten considering  $\dot{q}(t) = i(t)$  as:

$$\begin{cases} m_a\ddot{z}(t) + c_a[\dot{z}(t) - \dot{w}(t)] + k_a[z(t) - w(t)] - k_{em}i(t) = 0 \\ L\frac{di(t)}{dt} + Ri(t) + k_{em}[\dot{z}(t) - \dot{w}(t)] = v(t) \end{cases} \quad (2.10)$$

The first equation describes the mechanical behavior, whereas the second is referred to the dynamics of the electrical part. The actuator is mechanically equivalent to a spring-mass-damper system subjected to a control force due to the electromechanic coupling  $f_c(t) = k_{em}i(t)$ . The current  $i(t)$  arises from the electrical equation if the actuator is voltage driven. If current driven, instead, it is directly provided by the current source and the electrical equation is discarded.

## 2.1.2 State space realization

The system in Eq. 2.10 can be conveniently rewritten in state space introducing the following substitutions:

$$\begin{cases} x_1 = z \\ x_2 = \dot{z} \\ x_3 = i \end{cases} \quad \begin{cases} u_1 = w \\ u_2 = \dot{w} \\ u_3 = v \end{cases} \quad (2.11)$$

Obtaining three first order differential equations, as follows.

$$\begin{cases} \dot{x}_1 = x_2 \\ \dot{x}_2 = -\frac{k_a}{m_a}x_1 - \frac{c_a}{m_a}x_2 + \frac{k_{em}}{m_a}x_3 + \frac{k_a}{m_a}u_1 + \frac{c_a}{m_a}u_2 \\ \dot{x}_3 = -\frac{k_{em}}{L}x_2 - \frac{R}{L}x_3 + \frac{k_{em}}{L}u_2 + \frac{1}{L}u_3 \end{cases} \quad (2.12)$$

$$\begin{bmatrix} \dot{x}_1 \\ \dot{x}_2 \\ \dot{x}_3 \end{bmatrix} = \begin{bmatrix} 0 & 1 & 0 \\ -\frac{k_a}{m_a} & -\frac{c_a}{m_a} & \frac{k_{em}}{m_a} \\ 0 & -\frac{k_{em}}{L} & -\frac{R}{L} \end{bmatrix} \begin{bmatrix} x_1 \\ x_2 \\ x_3 \end{bmatrix} + \begin{bmatrix} 0 & 0 & 0 \\ \frac{k_a}{m_a} & \frac{c_a}{m_a} & 0 \\ 0 & \frac{k_{em}}{L} & \frac{1}{L} \end{bmatrix} \begin{bmatrix} u_1 \\ u_2 \\ u_3 \end{bmatrix} \quad (2.13)$$

That can be written in the form

$$\dot{x} = Ax + Bu \quad (2.14)$$

Where

$$A = \begin{bmatrix} 0 & 1 & 0 \\ -\frac{k_a}{m_a} & -\frac{c_a}{m_a} & \frac{k_{em}}{m_a} \\ 0 & -\frac{k_{em}}{L} & -\frac{R}{L} \end{bmatrix} \quad \text{and} \quad B = \begin{bmatrix} 0 & 0 & 0 \\ \frac{k_a}{m_a} & \frac{c_a}{m_a} & 0 \\ 0 & \frac{k_{em}}{L} & \frac{1}{L} \end{bmatrix}$$

The state space realization has been used in MATLAB to couple the different dynamic system described in this chapter. Of course it is not the only way - for instance everything could be done through transfer functions obtaining exactly the same results. The process for obtaining the state space model of a system is straightforward and has been described above, therefore - for the sake of brevity - it will not be repeated for every system.

### 2.1.3 Static residualization of the electrical dynamics

If the electrical dynamics is faster enough than the mechanical dynamics, a static residualization of the former can be introduced. Starting from the dynamics system in Eq.

2.10 and introducing the approximation of  $\frac{di(t)}{dt} = 0$ , the electrical equation is simplified as follows.

$$\begin{cases} m_a \ddot{z}(t) + c_a [\dot{z}(t) - \dot{w}(t)] + k_a [z(t) - w(t)] - k_{em} i(t) = 0 \\ i(t) = -\frac{k_{em}}{R} [\dot{z}(t) - \dot{w}(t)] + \frac{1}{R} v_a(t) \end{cases} \quad (2.15)$$

Substituting the expression of  $i(t)$  from the electrical equation into the mechanical equation, it can be obtained the following differential expression for the actuator with residualized electric dynamics.

$$m_a \ddot{z}(t) + \left( c_a + \frac{k_{em}^2}{R} \right) [\dot{z}(t) - \dot{w}(t)] + k_a [z(t) - w(t)] = \frac{k_{em}}{R} v_a(t) \quad (2.16)$$

### 2.1.4 Rigid base

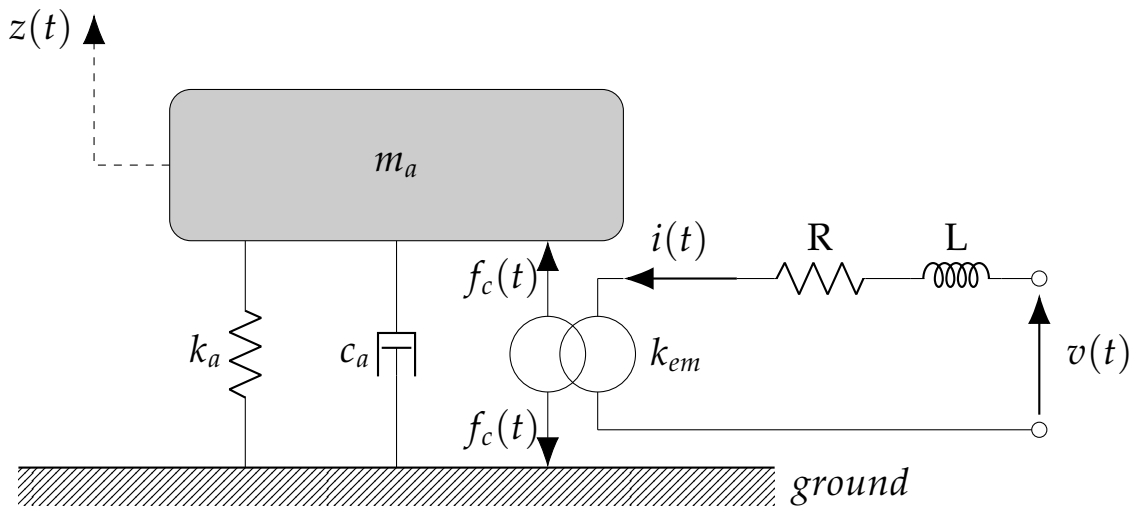


**Figure 2.2:** Schematic representation of the lumped-parameters model of the inertial actuator, when it is attached on a fixed, rigid surface.

So far it has been considered an actuator attached on a generic flexible surface. In Chapter 3 it will be described the experimental procedure adopted to compute the coefficients of the lumped-parameters model described previously. It will be seen later that the most practical solution is to attach the speaker on an infinitely rigid - therefore fixed - surface. Doing so allows to drop the dependency on the movement of the base and simplifies the mathematical description, thus the mathematical model of the actuator mounted on a rigid surface is required.

The derivation of the dynamics equations could be performed exactly as done for the flexible base case, computing the energies involved in the system and writing the Lagrange's equations. Alternatively it can be observed, comparing Figure 2.1 and Figure

2.2, that the only difference between the two systems is the dependency on the structural degree of freedom  $w(t)$ . Therefore it is enough to drop the terms in  $w(t)$  and  $\dot{w}(t)$  from Eq. 2.10, to obtain the dynamics equation for the actuator when mounted on a rigid base, Eq. 2.17.

$$\begin{cases} m_a \ddot{z}(t) + c_a \dot{z}(t) + k_a z(t) - k_{em} i(t) = 0 \\ L \frac{di(t)}{dt} + Ri(t) + k_{em} \dot{z}(t) = v(t) \end{cases} \quad (2.17)$$

### 2.1.5 Proof-mass acceleration response

In this section the actuator dynamics is described through the proof-mass acceleration response, defined as the transfer function between the electrical source and the acceleration of the moving mass. Dependently on how the electromagnetic inertial actuator is driven - in current or in voltage - different transfer functions are obtained.

In both cases the derivation starts from the dynamics equations in Eq. 2.17. In the voltage driven case both equations are used, whereas in the current driven case the second one can be dropped.

#### Voltage driven

Taking the Laplace transform of Eq. 2.17

$$\begin{cases} (m_a s^2 + c_a s + k_a) z(s) - k_{em} i(s) = 0 \\ (Ls + R)i(s) + k_{em} z(s) = v(s) \end{cases} \quad (2.18)$$

Computing  $i(s)$  from the second equation and substituting it in the first, the following expression is obtained:

$$\left( m_a s^2 + c_a s + k_a + \frac{k_{em}^2}{R + sL} \right) z(s) - \frac{k_{em}}{R + sL} v(s) = 0 \quad (2.19)$$

The dependency of the proof-mass acceleration on the driving voltage can now be readily obtained isolating  $z(s)$  and taking the second time derivative:

$$\ddot{z}(s) = \frac{s^2 k_{em}}{(R + sL)(m_a s^2 + c_a s + k_a) + s k_{em}^2} v(s) \quad (2.20)$$

The proof-mass acceleration response for the voltage driven actuator can now be made explicit, writing the following transfer function:

$$\tilde{H}_{aV}(s) = \frac{\ddot{z}(s)}{v(s)} = \frac{s^2 k_{em}}{(R + sL)(m_a s^2 + c_a s + k_a) + s k_{em}^2} \quad (2.21)$$

If the frequency separation between the mechanical and the electrical poles is high enough, it could be computationally useful to introduced the static residualization described before. Doing so the proof-mass acceleration response reads:

$$\tilde{H}_{aV res}(s) = \frac{\tilde{z}(s)}{v(s)} = \frac{s^2 k_e e m}{R(m_a s^2 + c_a s + k_a) + s k_{em}^2} \quad (2.22)$$

In Figure 2.3a both  $\tilde{H}_{aV}(s)$  and  $\tilde{H}_{aV res}(s)$  are depicted, using the parameters computed in Chapter 3 for a real actuator (Dayton A in Table 3.4). As predicted the two curves differs only at high frequencies, if this difference is acceptable is a matter that depends on the specific application and that will be analyzed later.

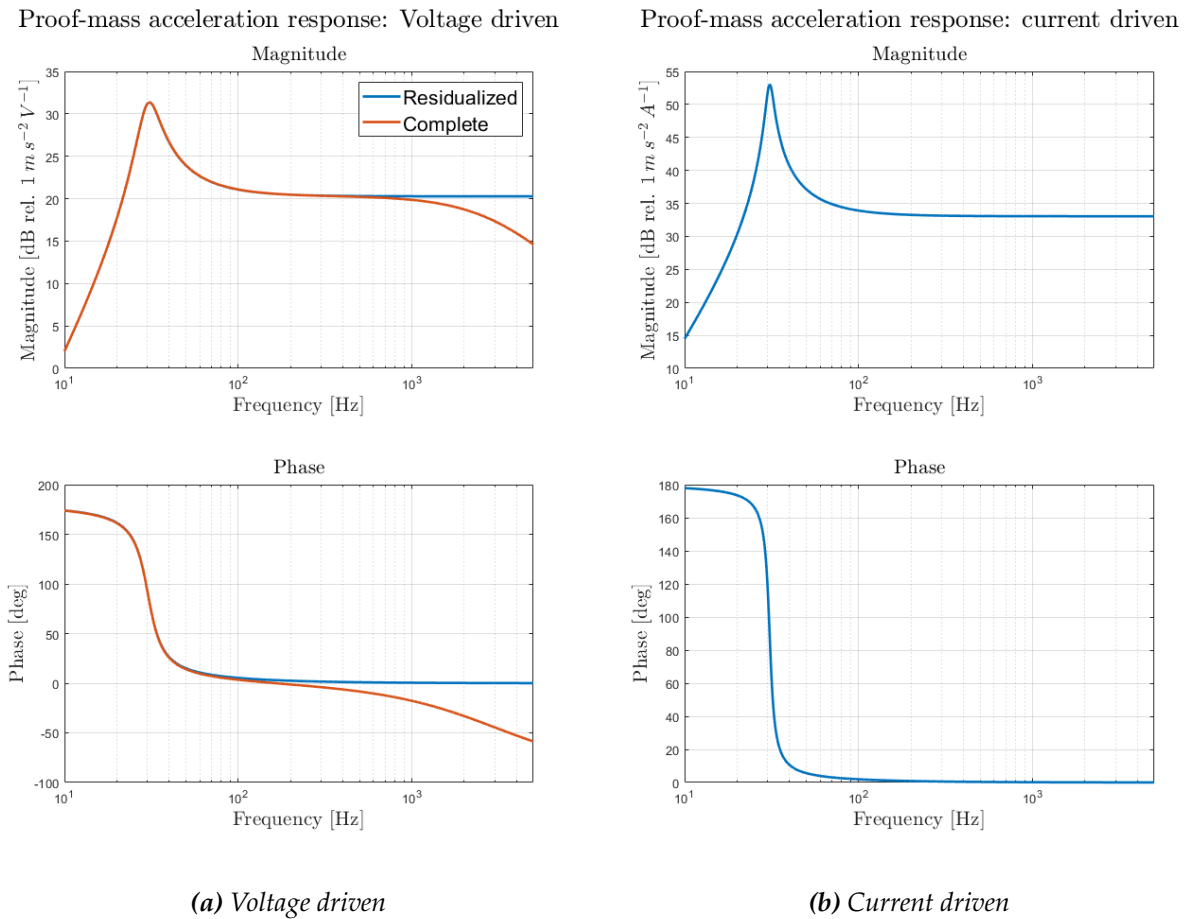


**Figure 2.3:** On the left: comparison of the proof-mass acceleration response for a voltage driven actuator with complete and residualized electrical dynamics. On the right: proof-mass acceleration response for a current driven actuator.

### Current driven

As anticipated, the derivation of the proof-mass acceleration response for a current driven actuator is a straightforward process. The system is described with only the

mechanical equation, therefore the dynamics of the actuator is reduced to the first equation of Eq. 2.18:

$$(m_a s^2 + c_a s + k_a)z(s) - k_{em}i(s) = 0 \quad (2.23)$$

It can be immediately computed  $z(s)$ , derived two times and rearranged to obtain the transfer function that describes the proof-mass acceleration response of a current driven actuator. Figure 2.3b shows its plot.

$$\tilde{H}_{ai}(s) = \frac{\ddot{z}(s)}{i(s)} = \frac{s^2 k_{em}}{m_a s^2 + c_a s + k_a} \quad (2.24)$$

The plots in Figure 2.3a and 2.3b anticipate the behaviour of one of the actuator that will be used in this work. Note that both voltage and current driven responses show a resonance peak at the same frequency, around 30Hz. This is the fundamental frequency of the single degree of freedom model used to describe the actuator.

### 2.1.6 Electrical input impedance

Another way of characterizing the electromechanic dynamics of a proof-mass actuator is to study its electrical input impedance. The electric circuit composing the driver of the vibration speaker is well described by a RL circuit. The electrical impedance of such a circuit is an extension of the concept of electric resistance in simple resistive circuit, therefore the ratio of the applied voltage over the flowing current. As done in the context of the proof-mass acceleration response, the derivation of the electrical input impedance transfer function starts from the dynamics equations of the actuator when it is attached on a fixed surface, Eq. 2.17. The Laplace transform of the system is the same as before and it's reported here for the sake of clarity:

$$\begin{cases} (m_a s^2 + c_a s + k_a)z(s) - k_{em}i(s) = 0 \\ (Ls + R)i(s) + k_{em}z(s) = v(s) \end{cases} \quad (2.25)$$

The aim is to obtain an expression depending only on  $i(s)$  and  $v(s)$ . It can be easily done isolating  $z(s)$  in the second equation.

$$\begin{cases} (m_a s^2 + c_a s + k_a)z(s) - k_{em}i(s) = 0 \\ z(s) = \frac{1}{k_{em}s}v(s) - \frac{R + sL}{k_{em}s}i(s) \end{cases} \quad (2.26)$$

Substituting  $z(s)$  back in the mechanical equation the following expression is obtained:

$$(m_a s^2 + c_a s + k_a)v(s) = \left[ (R + sL)(m_a s^2 + c_a s + k_a) - k_{em}^2 s \right] i(s) \quad (2.27)$$



It can be expressed in the form of a transfer function:

$$\tilde{H}_{Vi}(s) = \frac{v(s)}{i(s)} = \frac{(R + sL)(m_a s^2 + c_a s + k_a) - k_{em}^2 s}{m_a s^2 + c_a s + k_a} \quad (2.28)$$

As before, it could be interesting to consider the statically residualized electric case.

$$\tilde{H}_{Vi\,res}(s) = \frac{v(s)}{i(s)} = \frac{R(m_a s^2 + c_a s + k_a) - k_{em}^2 s}{m_a s^2 + c_a s + k_a} \quad (2.29)$$

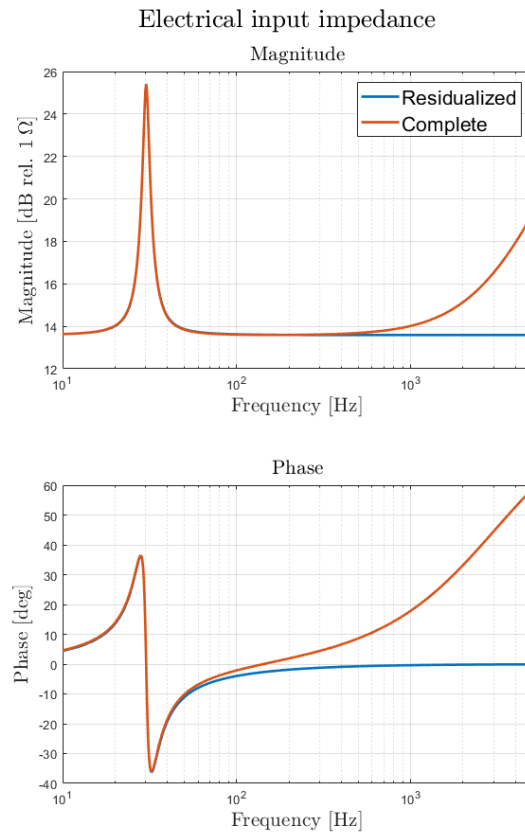


**Figure 2.4:** Comparison of the electrical input impedance of an actuator when complete and residualized electrical dynamics are considered.

Plots of both  $\tilde{H}_{Vi}(s)$  and  $\tilde{H}_{Vi\,res}(s)$  are displayed in Figure 2.4, having assumed the parameters of the actuator Dayton A in Table 3.4. If there were no mechanical dynamics and electrical inductance, the electrical impedance would have been an horizontal straight line equal to the electrical resistance  $R$ . The peak at low frequency is due to the mechanical poles, while the behaviour at high frequency is entirely determined by the inductance  $L$ . Indeed the effect of the inductance is to create an opposing induced current in the circuit, this is coherent with both the increase in impedance and with the lag of the current with respect to the tension displayed in the plot for high frequencies.

## 2.2 Reconstruction of the velocities

Aim of this section is to derive the mathematical formulation on which the sensor-actuator concept described in Chapter 1 is based. The objective is to obtain an expression that, by receiving as inputs only current and voltage, allows to reconstruct the transverse velocity of the plate to be used in the skyhook control strategy. The derivation follows what proposed in Ref. [9, 10], with the purpose to remove the need of accelerometers to obtain the transverse plate velocity. The same procedure will be also applied to reconstruct the velocity of the inertial mass of the actuator that could be needed in more advanced control logic to increase stability limits. Note that in the following, whenever a velocity is call *reconstructed*, reference is always made to the velocity obtained by current and voltage measurements.

### 2.2.1 Plate transverse velocity

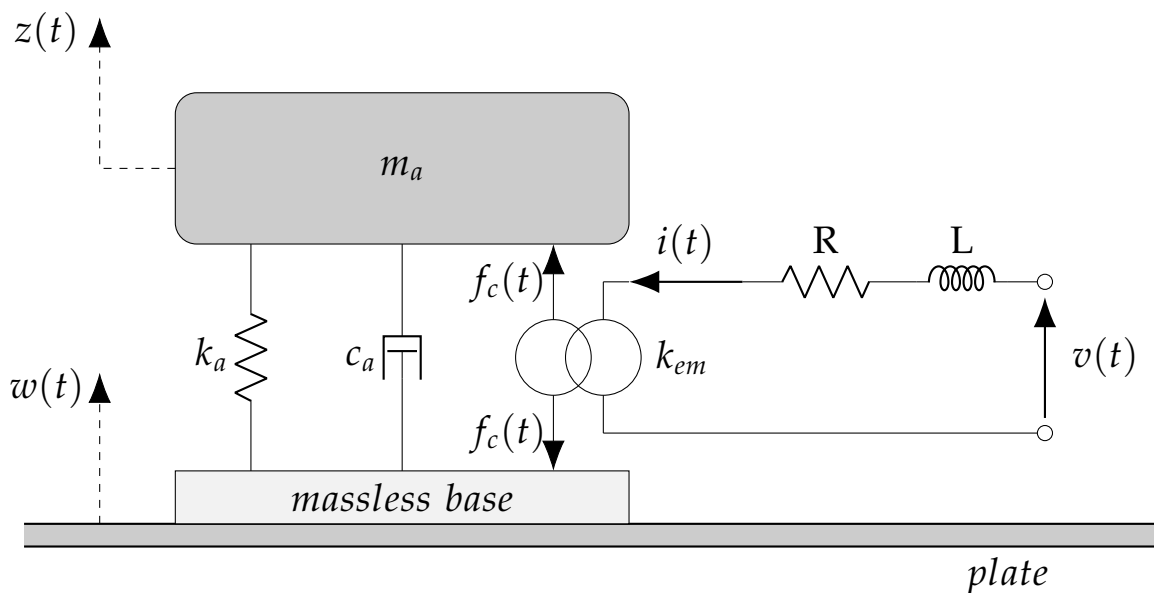


**Figure 2.5:** Schematic representation of the lumped-parameters model of the inertial actuator, when it is attached on a flexible surface.

The physical concept on which is based this work is the following: when a vibration speaker is mounted on a vibrating surface, the displacement of the base -  $w(t)$  in Figure 2.5 - causes a relative displacement of the inertial mass with respect to the base, causing - through the electromagnetic coupling - an induced current in the electrical circuit. The electrical quantities will thus contain "information" about the movement of the surface on which the actuator is attached. The derivation of a way to retrieve such an "information" moves from the dynamics equations of the actuator when attached on a flexible surface, reported in Eq. 2.30.

$$\begin{cases} m_a \ddot{z}(t) + c_a [\dot{z}(t) - \dot{w}(t)] + k_a [z(t) - w(t)] - k_{em} i(t) = 0 \\ L \frac{di(t)}{dt} + Ri(t) + k_{em} [\dot{z}(t) - \dot{w}(t)] = v(t) \end{cases} \quad (2.30)$$

Rewriting the same equations in the Laplace's domain:

$$\begin{cases} s^2 m_a z(s) + s c_a [z(s) - w(s)] + k_a [z(s) - w(s)] - k_{em} i(s) = 0 \\ sLi(s) + Ri(s) + s k_{em} [z(s) - w(s)] = v(s) \end{cases} \quad (2.31)$$

The aim is now to obtain an equation where the plate degree of freedom  $w(s)$ , depends only on the applied voltage  $v(s)$ , and on the flowing current  $i(s)$ . To do so it has to be eliminated the dependency on the inertial mass degree of freedom  $z(s)$ . Rearranging the electrical equation  $z(s)$  can be isolated:

$$z(s) = w(s) - \frac{R + sL}{s k_{em}} i(s) + \frac{1}{s k_{em}} v(s) \quad (2.32)$$

Substituting it into the mechanical equations it is obtained an expression in  $w(s)$ ,  $v(s)$  and  $i(s)$  alone.

$$s^2 m_a w(s) - \left( \frac{(R + sL) (s^2 m_a + s c_a + k_a)}{s k_{em}} + k_{em} \right) i(s) + \frac{s^2 m_a + s c_a + k_a}{s k_{em}} v(s) = 0 \quad (2.33)$$

It's now possible to isolate  $w(s)$ :

$$w(s) = \left[ \frac{(R + sL) (s^2 m_a + s c_a + k_a) + s k_{em}^2}{s^3 m_a k_{em}} \right] i(s) - \left[ \frac{s^2 m_a + s c_a + k_a}{s^3 m_a k_{em}} \right] v(s) \quad (2.34)$$

Taking the first time derivative, the desired transverse plate velocity is obtained:

$$\begin{aligned} \dot{w}(s) &= \left[ \frac{(R + sL) (s^2 m_a + s c_a + k_a) + s k_{em}^2}{s^2 m_a k_{em}} \right] i(s) - \left[ \frac{s^2 m_a + s c_a + k_a}{s^2 m_a k_{em}} \right] v(s) \\ &= H_i(s) i(s) - H_v(s) v(s) \end{aligned} \quad (2.35)$$

Eq. 2.35 allows to reconstruct the plate velocity - in the point where the actuator is placed - measuring only voltage and current.

It has to be pointed out that the current related transfer function -  $H_i(s)$  - is not proper, being the numerator of higher order than the denominator. This problem - among others - will be extensively addressed later. One possible way to overcome it, consists in the static residualization of the electric dynamic.

### Static residualization

The equation for the reconstruction of the plate transverse velocity in a statically residualized framework could be obtained intuitively just removing  $sL$  from Eq. 2.35, but for the sake of completeness it's hereby analytically derived. The derivation shall move from the dynamics equations for a statically residualized actuator attached on a flexible surface, Eq. 2.36.

$$\begin{cases} m_a \ddot{z}(t) + c_a [\dot{z}(t) - \dot{w}(t)] + k_a [z(t) - w(t)] - k_{em} i(t) = 0 \\ Ri(t) + k_{em} [\dot{z}(t) - \dot{w}(t)] = v_a(t) \end{cases} \quad (2.36)$$

Rewriting the same equations in the Laplace's domain:

$$\begin{cases} s^2 m_a z(s) + s c_a [z(s) - w(s)] + k_a [z(s) - w(s)] - k_{em} i(s) = 0 \\ Ri(s) + s k_{em} [z(s) - w(s)] = v_a(s) \end{cases} \quad (2.37)$$

From the electrical equation can be obtained  $z(s)$ :

$$z(s) = w(s) - \frac{R}{s k_{em}} i(s) + \frac{1}{s k_{em}} v(s) \quad (2.38)$$

Substituting it into the mechanical equations:

$$s^2 m_a w(s) - \left[ \frac{R (s^2 m_a + s c_a + k_a)}{s k_{em}} + k_{em} \right] i(s) + \left[ \frac{s^2 m_a + s c_a + k_a}{s k_{em}} \right] v(s) = 0 \quad (2.39)$$

Isolating  $w(s)$ :

$$w(s) = \left[ \frac{R (s^2 m_a + s c_a + k_a) + s k_{em}^2}{s^3 m_a k_{em}} \right] i(s) - \left[ \frac{s^2 m_a + s c_a + k_a}{s^3 m_a k_{em}} \right] v(s) \quad (2.40)$$

And deriving it:

$$\dot{w}(s) = \left[ \frac{R \left( s^2 m_a + s c_a + k_a \right) + s k_{em}^2}{s^2 m_a k_{em}} \right] i(s) - \left[ \frac{s^2 m_a + s c_a + k_a}{s^2 m_a k_{em}} \right] v(s) \quad (2.41)$$

As anticipated the only difference with the complete electrical dynamics case is the absence of the  $sL$  contribution.

### 2.2.2 Inertial mass velocity

As anticipated before it's possible to apply the same method and derive a formulation for the velocity of the inertial mass, depending only on the voltage applied to the inertial actuator and on the current flowing in it.

As before the derivation moves from the dynamics equations for the inertial actuator mounted on a flexible surface.

$$\begin{cases} m_a \ddot{z}(t) + c_a [\dot{z}(t) - \dot{w}(t)] + k_a [z(t) - w(t)] - k_{em} i(t) = 0 \\ L \frac{di(t)}{dt} + R i(t) + k_{em} [\dot{z}(t) - \dot{w}(t)] = v(t) \end{cases} \quad (2.42)$$

Rewriting the same equations in the Laplace's domain:

$$\begin{cases} s^2 m_a z(s) + s c_a [z(s) - w(s)] + k_a [z(s) - w(s)] - k_{em} i(s) = 0 \\ s L i(s) + R i(s) + s k_{em} [z(s) - w(s)] = v(s) \end{cases} \quad (2.43)$$

As above the electrical equation can be rearranged isolating, this time, the transverse plate velocity  $w(s)$ :

$$w(s) = z(s) + \frac{R + sL}{s k_{em}} i(s) - \frac{1}{s k_{em}} v(s) \quad (2.44)$$

Substituting it into the mechanical equation is obtained an expression in  $z(s)$ ,  $v(s)$  and  $i(s)$  alone:

$$s^2 m_a z(s) - \left( \frac{(R + sL)(s c_a + k_a)}{s k_{em}} + k_{em} \right) i(s) + \frac{s c_a + k_a}{s k_{em}} v(s) = 0 \quad (2.45)$$

Isolating  $z(s)$ :

$$z(s) = \left[ \frac{(R + sL)(sc_a + k_a) + sk_{em}^2}{s^3 m_a k_{em}} \right] i(s) - \left[ \frac{sc_a + k_a}{s^3 m_a k_{em}} \right] v(s) \quad (2.46)$$

Taking the first derivative the velocity of the inertial mass of the actuator is obtained:

$$\dot{z}(s) = \left[ \frac{(R + sL)(sc_a + k_a) + sk_{em}^2}{s^2 m_a k_{em}} \right] i(s) - \left[ \frac{sc_a + k_a}{s^2 m_a k_{em}} \right] v(s) \quad (2.47)$$

The statically residualized version of the previous equation can be easily obtained just dropping the inductance related term  $sL$ .

$$\dot{z}(s) = \left[ \frac{R(sc_a + k_a) + sk_{em}^2}{s^2 m_a k_{em}} \right] i(s) - \left[ \frac{sc_a + k_a}{s^2 m_a k_{em}} \right] v(s) \quad (2.48)$$

## 2.3 Pseudo-integrator

In a skyhook control strategy the transverse velocity of the plate is usually obtained by integration of the transverse acceleration. In later chapters, the performances of the reconstruction of the velocity obtained in the context of the self-sensing actuator, will be often compared to the classical approach. In this section is thus briefly described how to properly integrate the acceleration signal to obtain the velocity, as done in [11]. In the Laplace domain, the transfer function of a pure integrator would be:

$$\frac{y_{vel}(s)}{y_{acc}(s)} = \frac{1}{s}$$

If the acceleration signal presents a DC components - such the gravity - or even a small offset due to acquisition errors, a pure integral action is not recommended. Instead, the following pseudo-integration can be adopted.

$$\frac{y_{vel}(s)}{y_{acc}(s)} = \frac{s}{s^2 + 2\zeta_{pi}\omega_{pi}s + \omega_{pi}^2} \quad (2.49)$$

The parameters that will be used in the following - as selected in [11] - are reported in Table 2.2.

Parameter	Value	Units
Integrator Frequency	$2\pi$	$[rad\ s^{-1}]$
Damping Coefficient	0.707	$[-]$

*Table 2.2: Pseudo-integrator parameters.*

## 2.4 Power amplifiers

In the experimental setup object of this work, the vibrations speakers are driven by signals generated by a computer. Although the PC could provide a sufficiently large voltage output to drive directly the speakers -  $\pm 10V$  - it can not produce the required current due to its high output impedance - therefore neither the required power - that's why a power amplifier is required. A power amplifier is a common device that reproduces low power signals at levels that are strong enough for powering the most various items. Not only they provide enough current to drive low impedance devices, but they also give a mean to amplify the driving voltage. While the former aspect simply allows the speaker to work properly and does not require any mathematical modelling, the latter introduces a voltage gain that has to be quantified, if the behaviour of the amplifier has to be simulated numerically.

As will be discussed in Chapter 3, the speakers used in this work have an input impedance of  $4\Omega$ , allowing to drive them with common audio amplifiers.

Broadly speaking, an audio amplifier can be modeled as a band pass filter, whose behaviour is represented by the following transfer function:

$$H(s) = \tilde{g}_{amp} \frac{s}{(s+a)(s+b)}$$

Where  $\tilde{g}_{amp}$  is the voltage gain described above and  $a$  and  $b$  are respectively the low frequency and high frequency poles of the band pass filter. Taking into account that the range of human hearing spans from  $20Hz$  to  $20kHz$  [30], it's foreseeable that the high frequency pole of the amplifier would be around  $20kHz$ , far higher than the frequency range of interest of this work. Then, for the purpose of this thesis, the high frequency pole can be ignored and the audio amplifier transfer function can be reduced as follows:

$$H(s) = g_{amp} \frac{s}{s+a}$$

## 2.5 Plate Model

As outlined before, the plate has been modeled relying on the sublaminate generalized unified formulation (S-GUF) [31], developed through a collaboration between Politecnico di Milano and Université of Paris X. Although such a complex formulation would not be strictly required to model the thin homogeneous aluminum plate object of this work, it has been chosen because its versatility allows to promptly extend the results of the present work to more complex vibrating structures, in particular to multilayered composite and sandwich panels. In the following the key points of the S-GUF formulation are described, for the complete derivation make reference to [31].

### 2.5.1 The Sublaminar Generalized Unified Formulation

The majority of the nowadays available approaches to plate modeling are based on reducing the 3-D problem to a 2-D problem, introducing in advance some kinematic assumptions about the behaviour of the displacement field in the thickness direction of the plate. Such a modelling strategy is known as *axiomatic displacement-based approach* and the resulting 2-D models are called *displacement-based plate theories*.

The most used displacement-based plate theories are the Classical Plate Theory (CPT) and the First-order Shear Deformation Theory (FSDT). These theories originally addressed the need of working with computational economical models that could be handled by limited computational capabilities, however they could lead to inaccurate results when thick or multilayered structures are considered. These inaccuracies arise because a simple 2-D model can't properly catch some relevant 3-D effects such as transverse shear and normal deformations, cross-section warping, boundary layer stresses and through-the-thickness zig-zag behaviour of the displacement field. Indeed a formulation able to account in some way for these effects while keeping a relatively simple 2-D model of the plate - avoiding the need to resort to a cumbersome fully 3-D formulation - would be a powerful and interesting tool, that's in fact the case of the S-GUF approach.

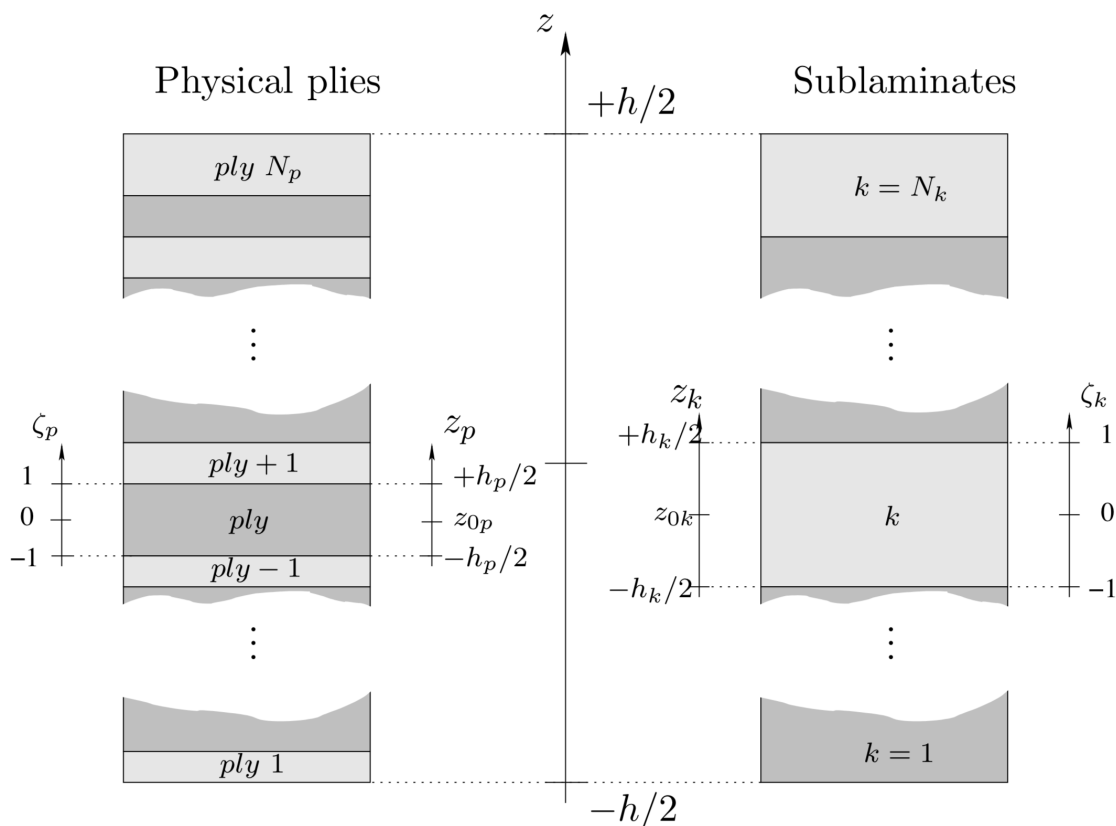


Figure 2.6: S-GUF geometric description



A peculiar characteristic of the S-GUF formulation is the fact that the kinematic description can be enriched when needed, introducing different 2-D kinematic theories of arbitrary order in different sub-regions of the plate thickness, so that a virtually infinite amount of plate models can be derived from a single general formulation. This approach shows its full potential with multilayered plates, when the concept of sublaminate - *a group of adjacent physical plies with a specific kinematic description* - can be introduced. The concept of sublaminates can be seen in Figure 2.6: a plate of thickness  $h$ , composed by  $N_p$  physical plies of homogeneous orthotropic material, is subdivided into  $k = 1, 2, \dots, N_k$  sublaminates of thickness  $h_k$ , numbered from bottom to top.

As previously said, in the S-GUF approach the user can introduce a different kinematic description in each sublaminate. Such an approach is called *layerwise* (LW) and it's formal expression is

$$\begin{cases} u_x^{p,k}(x, y, z_k, t) = F_{\alpha_{u_x}}(z_k) u_{x\alpha_{u_x}}^{p,k}(x, y, t) & (\alpha_{u_x} = 0, 1, \dots, N_x) \\ u_y^{p,k}(x, y, z_k, t) = F_{\alpha_{u_y}}(z_k) u_{y\alpha_{u_y}}^{p,k}(x, y, t) & (\alpha_{u_y} = 0, 1, \dots, N_y) \\ u_z^{p,k}(x, y, z_k, t) = F_{\alpha_{u_z}}(z_k) u_{z\alpha_{u_z}}^{p,k}(x, y, t) & (\alpha_{u_z} = 0, 1, \dots, N_z) \end{cases} \quad (2.50)$$

Where  $u_r^{p,k}(x, y, z_k, t)$  are the displacements components ( $r = x, y$ , or  $z$ ),  $F_{\alpha_{u_r}}(z_k)$  are thickness functions defined in terms of the sublaminate coordinate  $z_k$ , and  $u_{r\alpha_{u_r}}^{p,k}(x, y, t)$  are the kinematic variables for layerwise description in the ply  $p = 1, 2, \dots, N_p^k$  of the sublaminate  $k$ .  $N_r$  is the order of expansion of the  $u_r$  component. Eq. 2.50 represent the most general case. If the same kinematics is adopted for all the plies of one sublaminate than the approach is said *equivalent single-layer* (ESL) and can be expressed dropping the index  $p$ . It's worth to be noted that a specific local kinematics can be specified in each sublaminate, with the possibility to obtain a multiple-kinematics model of the plate in a straightforward way. For instance a sandwich panel can be divided in three sublaminates: two low-order sublaminates describing the stiff laminated skins and one higher-order sublaminate for the soft thick core. Of course also common single kinematic model can be obtained as special cases when a single sublaminate is used to describe the whole plate. In particular, the thin isotropic aluminum plate object of this work can be described by a full ESL model, whose S-GUF parameters are defined as follows

$$\begin{cases} p = 1 \\ k = 1 \\ N_x = 1 \\ N_y = 1 \\ N_z = 0 \\ F_0 = 0 \\ F_1 = z \end{cases} \quad (2.51)$$

Corresponding to the classical *first-order shear deformation theory* (FSDT) kinematics, with a displacement field described as:

$$\begin{cases} u_x = u_{x0} + z u_{x1} \\ u_y = u_{y0} + z u_{y1} \\ u_z = u_{z0} \end{cases} \quad (2.52)$$

## 2.5.2 Constitutive equations

If linearly elastic materials are considered, stress  $\sigma_{ij}$  and strain  $\varepsilon_{ij}$ , are represented by second order tensors and are related through the fourth order elasticity tensor  $\mathbf{C}_{ijkl}$  as in the following constitutive equation:

$$\sigma_{ij} = \mathbf{C}_{ijkl} \varepsilon_{kl} \quad (2.53)$$

Where  $i, j, k, l = 1, 2, 3$ . Thanks to the symmetry of both stress and strain - meaning  $\sigma_{ij} = \sigma_{ji}$  and  $\varepsilon_{kl} = \varepsilon_{lk}$  - a more convenient matrix notation can be introduced.

$$\sigma_m = \mathbf{C} \varepsilon_m \quad (2.54)$$

Making all terms explicit

$$\begin{pmatrix} \sigma_{11} \\ \sigma_{22} \\ \sigma_{33} \\ \sigma_{23} \\ \sigma_{31} \\ \sigma_{12} \end{pmatrix} = \begin{bmatrix} C_{11} & C_{12} & C_{13} & C_{14} & C_{15} & C_{16} \\ C_{21} & C_{22} & C_{23} & C_{24} & C_{25} & C_{26} \\ C_{31} & C_{32} & C_{33} & C_{34} & C_{35} & C_{36} \\ C_{41} & C_{42} & C_{43} & C_{44} & C_{45} & C_{46} \\ C_{51} & C_{52} & C_{53} & C_{54} & C_{55} & C_{56} \\ C_{61} & C_{62} & C_{63} & C_{64} & C_{65} & C_{66} \end{bmatrix} \begin{pmatrix} \varepsilon_{11} \\ \varepsilon_{22} \\ \varepsilon_{33} \\ \varepsilon_{23} \\ \varepsilon_{31} \\ \varepsilon_{12} \end{pmatrix} \quad (2.55)$$

The matrix  $C$  is a  $6 \times 6$  matrix, with 36 independent components but some simplifications can be introduced for the simple aluminum plate under analysis. If a strain energy function can be defined,  $C$  becomes symmetric and the free components are reduced to 21. If the material is also *isotropic* - having identical properties in any direction - the Hooke's law reduces as follows.

$$\begin{pmatrix} \sigma_{11} \\ \sigma_{22} \\ \sigma_{33} \\ \tau_{23} \\ \tau_{31} \\ \tau_{12} \end{pmatrix} = \begin{bmatrix} C_{11} & C_{12} & C_{12} & 0 & 0 & 0 \\ & C_{11} & C_{12} & 0 & 0 & 0 \\ & & C_{11} & 0 & 0 & 0 \\ & & & C_{44} & 0 & 0 \\ \text{sym} & & & & C_{44} & 0 \\ & & & & & C_{44} \end{bmatrix} \begin{pmatrix} \varepsilon_{11} \\ \varepsilon_{22} \\ \varepsilon_{33} \\ \gamma_{23} \\ \gamma_{31} \\ \gamma_{12} \end{pmatrix} \quad (2.56)$$

Where the engineering stress and strain vectors have also been introduced. Due to their symmetric properties, isotropic materials as the plate under analysis involve only 3 elastic constants:  $C_{11}$ ,  $C_{12}$  and  $C_{44}$ , related to physical and mechanical properties as:

$$C_{11} = \frac{E(1-\nu)}{(1+\nu)(1-2\nu)} \quad (2.57)$$

$$C_{12} = \frac{E\nu}{(1+\nu)(1-2\nu)}$$

$$C_{44} = \frac{E}{(1+\nu)}$$

Where  $E$  is the Young's modulus and  $\nu$  is the Poisson's ratio.

Going back to the more general *orthotropic* case, a mean to express strain and stress of all physical plies in the same reference frame is needed. It can be introduced a reference frame  $(x, y, z)$  for the whole laminate and transform the quantities of each ply into this new frame. Exploiting the matrix representation introduced above it can be easily done as follows.

$$\sigma = T\sigma_m \quad (2.58)$$

$$\varepsilon_m = T^T\varepsilon \quad (2.59)$$

Where the matrix  $T$  is defined as

$$T = \begin{bmatrix} \cos^2\theta & \sin^2\theta & 0 & 0 & 0 & -2\sin\theta\cos\theta \\ \sin^2\theta & \cos^2\theta & 0 & 0 & 0 & 2\sin\theta\cos\theta \\ 0 & 0 & 1 & 0 & 0 & 0 \\ 0 & 0 & 0 & \cos\theta & \sin\theta & 0 \\ 0 & 0 & 0 & -\sin\theta & \cos\theta & 0 \\ \sin\theta\cos\theta & -\sin\theta\cos\theta & 0 & 0 & 0 & \cos^2\theta - \sin^2\theta \end{bmatrix} \quad (2.60)$$

Where  $\theta$  is the angle between the two reference frames. Putting together Eq. (2.59), (2.54) and (2.58) the Hooke's law in the laminate coordinates can be rewritten as

$$\sigma = \tilde{C}\varepsilon \quad (2.61)$$

Where  $\tilde{C} = TCT^T$ .

If stress and strains are divided between in-plane and out-of plane components:

$$\boldsymbol{\sigma}_\Omega = \begin{bmatrix} \sigma_{xx} & \sigma_{yy} & \tau_{xy} \end{bmatrix}^T \quad \boldsymbol{\varepsilon}_\Omega = \begin{bmatrix} \varepsilon_{xx} & \varepsilon_{yy} & \gamma_{xy} \end{bmatrix}^T \quad (2.62)$$

$$\boldsymbol{\sigma}_n = \begin{bmatrix} \tau_{yz} & \tau_{xz} & \sigma_{zz} \end{bmatrix}^T \quad \boldsymbol{\varepsilon}_n = \begin{bmatrix} \gamma_{yz} & \gamma_{xz} & \varepsilon_{zz} \end{bmatrix}^T \quad (2.63)$$

the Hooke's law can be rewritten as follows:

$$\boldsymbol{\sigma}_\Omega = \tilde{\mathbf{C}}_{\Omega\Omega} \boldsymbol{\varepsilon}_\Omega + \tilde{\mathbf{C}}_{\Omega n} \boldsymbol{\varepsilon}_n \quad (2.64)$$

$$\boldsymbol{\sigma}_n = \tilde{\mathbf{C}}_{n\Omega} \boldsymbol{\varepsilon}_\Omega + \tilde{\mathbf{C}}_{nn} \boldsymbol{\varepsilon}_n \quad (2.65)$$

Since the material can be different for each physical ply, to the above equations can be added the superscripts  $p$  and  $k$ , in order to refer them to the  $p$ -th ply of the  $k$ -th sublaminates.

### 2.5.3 Gradient equations

If a linear framework is assumed, a matrix of differential operators can link strains and displacements as follows.

$$\boldsymbol{\varepsilon} = \mathbf{D}\mathbf{u} \quad (2.66)$$

With

$$\mathbf{D} = \begin{bmatrix} \frac{\partial}{\partial x} & 0 & 0 \\ 0 & \frac{\partial}{\partial y} & 0 \\ \frac{\partial}{\partial y} & \frac{\partial}{\partial x} & 0 \\ \frac{\partial}{\partial z} & 0 & \frac{\partial}{\partial x} \\ 0 & \frac{\partial}{\partial z} & \frac{\partial}{\partial y} \\ 0 & 0 & \frac{\partial}{\partial z} \end{bmatrix} \quad (2.67)$$

$$\mathbf{u} = \begin{bmatrix} u_x & u_y & u_z \end{bmatrix}^T \quad (2.68)$$

Recalling the distinction between in-plane and normal strain components introduced before, Eq. 2.66 can be rewritten as follows.

$$\boldsymbol{\varepsilon}_\Omega = \mathbf{D}_\Omega \mathbf{u} \quad (2.69)$$

$$\boldsymbol{\varepsilon}_n = (\mathbf{D}_n + \mathbf{D}_z) \mathbf{u} \quad (2.70)$$

Where

$$\mathbf{D}_\Omega = \begin{bmatrix} \frac{\partial}{\partial x} & 0 & 0 \\ 0 & \frac{\partial}{\partial y} & 0 \\ \frac{\partial}{\partial y} & \frac{\partial}{\partial x} & 0 \end{bmatrix} \quad \mathbf{D}_n = \begin{bmatrix} 0 & 0 & \frac{\partial}{\partial x} \\ 0 & 0 & \frac{\partial}{\partial y} \\ 0 & 0 & 0 \end{bmatrix} \quad \mathbf{D}_z = \begin{bmatrix} \frac{\partial}{\partial z} & 0 & 0 \\ 0 & \frac{\partial}{\partial z} & 0 \\ 0 & 0 & \frac{\partial}{\partial z} \end{bmatrix}$$

Such that, the strain components for the  $p$ -th ply of the  $k$ -th sublaminate can be expressed as:

$$\boldsymbol{\varepsilon}_\Omega^{p,k} = \mathbf{D}_\Omega \mathbf{u}^{p,k} \quad (2.71)$$

$$\boldsymbol{\varepsilon}_n^{p,k} = \mathbf{D}_n \mathbf{u}^{p,k} + \mathbf{D}_z \mathbf{u}^{p,k} \quad (2.72)$$

### 2.5.4 Ritz approximation

Let's assume the plate to have a density  $\rho = \rho(x, y, z)$ , to occupy a volume  $V = \Omega \times [h/2, h/2]$  - where  $\Omega$  is the reference surface - and to be subjected to a normal pressure  $f_{top} = f_z^{top}$  and  $f_{bot} = f_z^{bot}$  applied at its top and bottom surfaces, respectively  $z = h/2$  and  $z = -h/2$ . The equilibrium condition can be written resorting to the *Principle of Virtual Displacements* (PVD), as follows

$$\int_\Omega \int_{-h/2}^{h/2} \delta \boldsymbol{\varepsilon}^T \boldsymbol{\sigma} \, dz \, d\Omega = - \int_\Omega \int_{-h/2}^{h/2} \delta \mathbf{u}^T \rho \ddot{\mathbf{u}} \, dz \, d\Omega + \int_\Omega \delta u_{top} f_{top} \, d\Omega + \int_\Omega \delta u_{bot} f_{bot} \, d\Omega \quad (2.73)$$

That can be rewritten in the context of the S-GUF formulation taking into account each ply  $p$  of each sublaminate  $k$ .

$$\begin{aligned} & \sum_{k=1}^{N_k} \sum_{p=1}^{N_p^k} \int_\Omega \int_{z_p^{bot}}^{z_p^{top}} \left( \delta \boldsymbol{\varepsilon}_\Omega^{p,kT} \boldsymbol{\sigma}_\Omega^{p,k} + \delta \boldsymbol{\varepsilon}_n^{p,kT} \boldsymbol{\sigma}_n^{p,k} \right) \, dz \, d\Omega = \\ & - \sum_{k=1}^{N_k} \sum_{p=1}^{N_p^k} \int_\Omega \int_{z_p^{bot}}^{z_p^{top}} \delta \mathbf{u}^{p,kT} \rho^{p,k} \ddot{\mathbf{u}}^{p,k} \, dz \, d\Omega + \delta u_{z_0}^{N_p^k, N_k} f_z^{top} + \delta u_{z_1}^{1,1} f_z^{bot} \end{aligned} \quad (2.74)$$

Where  $\mathbf{u}^{p,k}$  is the displacement vector at ply  $p$  of sublaminate  $k$ .

The weak form of the equilibrium condition expressed so far by the principle of virtual displacement in Eq. 2.74 - integrated with the constitutive and gradient equations derived before - can be used as the starting point for deriving a suitable model in the  $(x, y)$  plane of the multilayered structure. Indeed, once a specific plate theory is postulated through the thickness, different methods can be used to compute a solution

for the reduced 2-D problem in the  $(x, y)$  plane. In the S-GUF formulation this task is performed through the discretization using the Ritz approach. The Ritz approximation of the 2-D kinematic variables can be written as follows

$$\begin{cases} u_{x\alpha_{u_x}}^{p,k}(x, y, t) = N_{u_x j}(x, y) u_{x\alpha_{u_x} j}^{p,k}(t) \\ u_{y\alpha_{u_y}}^{p,k}(x, y, t) = N_{u_y j}(x, y) u_{y\alpha_{u_y} j}^{p,k}(t) \\ u_{z\alpha_{u_z}}^{p,k}(x, y, t) = N_{u_z j}(x, y) u_{z\alpha_{u_z} j}^{p,k}(t) \end{cases} \quad j = 1, 2, \dots, M \quad (2.75)$$

Where  $N_{u_r i}$  is the  $i$ -th admissible function related to  $u_r$  ( $r = x, y, z$ ). Note that in Eq. 2.75 the summation over the repeated index  $i$  is implied.

Eq. 2.75 shows that the assumed solutions are in the form of a linear combination of undetermined parameters with appropriate chosen functions. The number of terms of the combination is given by  $M$ , which is called the Ritz order. The generic admissible function can be expressed - mapping the physical  $(x, y)$  domain into the computational  $(\xi, \eta)$  domain defined in the interval  $[-1, 1] \times [-1, 1]$  - as follows

$$N_{u_r i}(\xi, \eta) = \phi_{u_r m}(\xi) \psi_{u_r n}(\eta) \quad (m = 1, \dots, R; n = 1, \dots, S)$$

Where  $R \cdot S = M$ ,  $i = S(m - 1) + n$  and

$$\begin{aligned} \phi_{u_r m}(\xi) &= f_{u_r}(\xi) p_m(\xi) \\ \psi_{u_r n}(\eta) &= g_{u_r}(\eta) p_n(\eta) \end{aligned} \quad (2.76)$$

The completeness of the Ritz functions is guaranteed by  $p_m$  and  $p_n$ , taken as Legendre orthogonal polynomials. The compliance with the geometric boundary conditions is achieved thanks to the boundary functions  $f_{u-r}$  and  $g_{u-r}$ , expressed in the following form.

$$\begin{aligned} f_{u_r}(\xi) &= (1 + \xi)^{e_{1r}} (1 - \xi)^{e_{2r}} \\ g_{u_r}(\eta) &= (1 + \eta)^{e_{1r}} (1 - \eta)^{e_{2r}} \end{aligned}$$

Where the value of the exponents  $e_{1r}$  and  $e_{2r}$  are selected according to the boundary conditions.

The following compact notation for the integrals of the Ritz functions can be introduced.

$$\mathcal{I}_{u_r u_s ij}^{defg} = \int_{\Omega} \frac{\partial^{d+e} N_{u_r i}}{\partial x^d \partial y^e} \frac{\partial^{f+g} N_{u_s j}}{\partial x^f \partial y^g} d\Omega \quad (d, e, f, g = 0, 1) \quad (2.77)$$

The Ritz approximate form of the PVD derived before can now be expressed as in Eq. 2.78, where many elastic terms are omitted for the sake of brevity.

$$\begin{aligned}
& \sum_{k=1}^{N_k} \sum_{p=1}^{N_p^k} \left[ \delta u_{x\alpha_{ux}i}^{p,k} \rho^{p,k} Z_{u_x u_x}^{p\alpha_{ux}\beta_{ux}} \mathcal{I}_{u_x u_x ij}^{0000} \dot{u}_{x\beta_{ux}j}^{p,k} + \delta u_{y\alpha_{uy}i}^{p,k} \rho^{p,k} Z_{u_y u_y}^{p\alpha_{uy}\beta_{uy}} \mathcal{I}_{u_y u_y ij}^{0000} \dot{u}_{y\beta_{uy}j}^{p,k} \right. \\
& \quad \left. + \delta u_{z\alpha_{uz}i}^{p,k} \rho^{p,k} Z_{u_z u_z}^{p\alpha_{uz}\beta_{uz}} \mathcal{I}_{u_z u_z ij}^{0000} \dot{u}_{z\beta_{uz}j}^{p,k} \right] + \\
& \sum_{k=1}^{N_k} \sum_{p=1}^{N_p^k} \left[ \delta u_{x\alpha_{ux}i}^{p,k} \tilde{C}_{11}^{p,k} Z_{u_x u_x}^{p\alpha_{ux}\beta_{ux}} \mathcal{I}_{u_x u_x ij}^{1010} u_{x\beta_{ux}j}^{p,k} + \delta u_{x\alpha_{ux}i}^{p,k} \tilde{C}_{12}^{p,k} Z_{u_x u_y}^{p\alpha_{ux}\beta_{uy}} \mathcal{I}_{u_x u_y ij}^{1001} u_{y\beta_{uy}j}^{p,k} \right. \\
& \quad + \delta u_{x\alpha_{ux}i}^{p,k} \tilde{C}_{16}^{p,k} Z_{u_x u_x}^{p\alpha_{ux}\beta_{ux}} \mathcal{I}_{u_x u_x ij}^{1001} u_{x\beta_{ux}j}^{p,k} + \delta u_{x\alpha_{ux}i}^{p,k} \tilde{C}_{16}^{p,k} Z_{u_x u_y}^{p\alpha_{ux}\beta_{uy}} \mathcal{I}_{u_x u_y ij}^{1010} u_{y\beta_{uy}j}^{p,k} + \dots \\
& \quad \left. + \dots + \delta u_{z\alpha_{uz}i}^{p,k} \tilde{C}_{33}^{p,k} Z_{\partial u_z \partial u_z}^{p\alpha_{uz}\beta_{uz}} \mathcal{I}_{u_z u_z ij}^{0000} u_{z\beta_{uz}j}^{p,k} \right] = \\
& \delta u_{z0i}^{N_p^k, N_k} \int_{\Omega} N_{u_z i} f_z^{\text{top}} d\Omega + \delta u_{z1i}^{1,1} \int_{\Omega} N_{u_z i} f_z^{\text{bot}} d\Omega
\end{aligned} \tag{2.78}$$

### 2.5.5 Expansion and assembly

From the indicial form shown in Eq. 2.78, can be constructed the matrices and the load vectors o a virtually infinite number of plate models, trough a procedure consisting in successive expansion and assembly steps of elementary blocks of the formulation called *kernels* end defined as follows.

$$\tilde{C}_{RS}^{p,k} Z_{(\partial)u_r(\partial)u_s}^{p\alpha_{ur}\beta_{us}} \mathcal{I}_{u_r u_s ij}^{defg} \quad (\text{elastic terms}) \tag{2.79}$$

$$\rho^{p,k} Z_{u_r u_s}^{p\alpha_{ur}\beta_{us}} \mathcal{I}_{u_r u_s ij}^{defg} \quad (\text{inertial terms}) \tag{2.80}$$

In the following are schematized the four cycles from the fundamental kernels to the mass and stiffness matrices of the plate model.

1. Summation over the repeated indexes  $\alpha_{ur}$  and  $\beta_{us}$ , arising from the order of the kinematic description assumed in each sublaminare. Symbolically it can be expressed as

$$Z_{(\partial)u_r(\partial)u_s}^{p\alpha_{ur}\beta_{us}} \xrightarrow[\text{(\alpha_{ur}, \beta_{us}) cycling}]{\text{theory expansion}} Z_{(\partial)u_r(\partial)u_s}^{p,k} \quad (r, s = x, y, z)$$

2. Summation of the contribution of each ply inside a specified sublaminare, cycling over  $p$ . Symbolically it can be expressed as

$$\tilde{C}_{RS}^{p,k} Z_{(\partial)u_r(\partial)u_s}^{p,k} \xrightarrow[p \text{ cycling}]{\text{ply assembly}} Z_{(\partial)u_r(\partial)u_s}^k$$

$$\rho^{p,k} \mathbf{Z}_{u_r u_s}^{p,k} \xrightarrow[p \text{ cycling}]{\text{ply assembly}} \mathbf{Z}_{u_r u_s \rho}^k$$

3. Summation over all the sublaminates - index  $k$  - imposing the continuity of the displacements at the interfaces of adjacent sublaminates. Symbolically it can be expressed as

$$\mathbf{Z}_{(\partial)u_r(\partial)u_sRS}^k \xrightarrow[k \text{ cycling}]{\text{sublaminates assembly}} \mathbf{Z}_{(\partial)u_r(\partial)u_sRS}$$

$$\mathbf{Z}_{u_r u_s \rho}^k \xrightarrow[k \text{ cycling}]{\text{sublaminates assembly}} \mathbf{Z}_{u_r u_s \rho}$$

Finally the following matrices for each  $i$  and  $j$  are obtained.

$$\mathbf{M}_{ij} = \begin{bmatrix} \mathbf{M}_{u_x u_x ij} & \mathbf{0} & \mathbf{0} \\ \mathbf{0} & \mathbf{M}_{u_y u_y ij} & \mathbf{0} \\ \mathbf{0} & \mathbf{0} & \mathbf{M}_{u_z u_z ij} \end{bmatrix} \quad (2.81)$$

$$\mathbf{K}_{ij} = \begin{bmatrix} \mathbf{K}_{u_x u_x ij} & \mathbf{K}_{u_x u_y ij} & \mathbf{K}_{u_x u_z ij} \\ \mathbf{K}_{u_y u_x ij} & \mathbf{K}_{u_y u_y ij} & \mathbf{K}_{u_y u_z ij} \\ \mathbf{K}_{u_z u_x ij} & \mathbf{K}_{u_z u_y ij} & \mathbf{K}_{u_z u_z ij} \end{bmatrix} \quad (2.82)$$

Where

$$\mathbf{M}_{u_x u_x ij} = \mathbf{Z}_{u_x u_x \rho} \mathcal{I}_{u_x u_x ij}^{0000}$$

$$\mathbf{M}_{u_y u_y ij} = \mathbf{Z}_{u_y u_y \rho} \mathcal{I}_{u_y u_y ij}^{0000}$$

$$\mathbf{M}_{u_z u_z ij} = \mathbf{Z}_{u_z u_z \rho} \mathcal{I}_{u_z u_z ij}^{0000}$$

$$\begin{aligned} \mathbf{K}_{u_x u_x ij} &= \mathbf{Z}_{u_x u_x 11} \mathcal{I}_{u_x u_x ij}^{1010} + \mathbf{Z}_{u_x u_x 16} (\mathcal{I}_{u_x u_x ij}^{1001} + \mathcal{I}_{u_x u_x ij}^{0110}) + \mathbf{Z}_{u_x u_x 66} \mathcal{I}_{u_x u_x ij}^{0101} \\ &\quad + \mathbf{Z}_{\partial u_x \partial u_x 55} \mathcal{I}_{u_x u_x ij}^{0000} \end{aligned}$$

$$\begin{aligned} \mathbf{K}_{u_x u_y ij} &= \mathbf{Z}_{u_x u_y 12} \mathcal{I}_{u_x u_y ij}^{1001} + \mathbf{Z}_{u_x u_y 16} \mathcal{I}_{u_x u_y ij}^{1010} + \mathbf{Z}_{u_x u_y 26} \mathcal{I}_{u_x u_y ij}^{0101} + \mathbf{Z}_{u_x u_y 66} \mathcal{I}_{u_x u_y ij}^{0110} \\ &\quad + \mathbf{Z}_{\partial u_x \partial u_y 45} \mathcal{I}_{u_x u_y ij}^{0000} \end{aligned}$$

$$\mathbf{K}_{u_x u_z ij} = \mathbf{Z}_{\partial u_x \partial u_z 55} \mathcal{I}_{u_x u_z ij}^{0010} + \mathbf{Z}_{\partial u_x \partial u_z 45} \mathcal{I}_{u_x u_z ij}^{0001} + \mathbf{Z}_{u_x \partial u_z 13} \mathcal{I}_{u_x u_z ij}^{1000} + \mathbf{Z}_{u_x \partial u_z 36} \mathcal{I}_{u_x u_z ij}^{0100}$$

$$\begin{aligned} \mathbf{K}_{u_y u_x ij} &= \mathbf{Z}_{u_y u_x 12} \mathcal{I}_{u_y u_x ij}^{0110} + \mathbf{Z}_{u_y u_x 26} \mathcal{I}_{u_y u_x ij}^{0101} + \mathbf{Z}_{u_y u_x 16} \mathcal{I}_{u_y u_x ij}^{1010} + \mathbf{Z}_{u_y u_x 66} \mathcal{I}_{u_y u_x ij}^{1001} \\ &\quad + \mathbf{Z}_{\partial u_y \partial u_x 45} \mathcal{I}_{u_y u_x ij}^{0000} \end{aligned}$$

$$\mathbf{K}_{u_y u_y ij} = \mathbf{Z}_{u_y u_y 22} \mathcal{I}_{u_y u_y ij}^{0101} + \mathbf{Z}_{u_y u_y 26} (\mathcal{I}_{u_y u_y ij}^{0110} + \mathcal{I}_{u_y u_y ij}^{1001}) + \mathbf{Z}_{u_y u_y 66} \mathcal{I}_{u_y u_y ij}^{1010}$$



$$\begin{aligned}
& + \mathbf{Z}_{\partial u_y \partial u_y 44} \mathcal{I}_{u_y u_y ij}^{0000} \\
\mathbf{K}_{u_y u_z ij} &= \mathbf{Z}_{\partial u_y u_z 45} \mathcal{I}_{u_y u_z ij}^{0010} + \mathbf{Z}_{\partial u_y u_z 44} \mathcal{I}_{u_y u_z ij}^{0001} + \mathbf{Z}_{u_y \partial u_z 23} \mathcal{I}_{u_y u_z ij}^{0100} + \mathbf{Z}_{u_y \partial u_z 36} \mathcal{I}_{u_y u_z ij}^{1000} \\
\mathbf{K}_{u_z u_x ij} &= \mathbf{Z}_{u_z \partial u_x 55} \mathcal{I}_{u_z u_x ij}^{1000} + \mathbf{Z}_{u_z \partial u_x 45} \mathcal{I}_{u_z u_x ij}^{0100} + \mathbf{Z}_{\partial u_z u_x 13} \mathcal{I}_{u_z u_x ij}^{0010} + \mathbf{Z}_{\partial u_z u_x 36} \mathcal{I}_{u_z u_x ij}^{0001} \\
\mathbf{K}_{u_z u_y ij} &= \mathbf{Z}_{u_z \partial u_y 45} \mathcal{I}_{u_z u_y ij}^{1000} + \mathbf{Z}_{u_z \partial u_y 44} \mathcal{I}_{u_z u_y ij}^{0100} + \mathbf{Z}_{\partial u_z u_y 23} \mathcal{I}_{u_z u_y ij}^{0001} + \mathbf{Z}_{\partial u_z u_y 36} \mathcal{I}_{u_z u_y ij}^{0010} \\
\mathbf{K}_{u_z u_z ij} &= \mathbf{Z}_{u_z u_z 55} \mathcal{I}_{u_z u_z ij}^{1010} + \mathbf{Z}_{u_z u_z 45} (\mathcal{I}_{u_z u_z ij}^{1001} + \mathcal{I}_{u_z u_z ij}^{0110}) + \mathbf{Z}_{u_z u_z 44} \mathcal{I}_{u_z u_z ij}^{0101} \\
& + \mathbf{Z}_{\partial u_z \partial u_z 33} \mathcal{I}_{u_z u_z ij}^{0000}
\end{aligned}$$

4. Summation over the  $i$  and  $j$  indices related to the Ritz series approximation of the kinematic quantities, obtaining the final mass and stiffness matrices of the plate. Symbolically it can be expressed as

$$\begin{aligned}
\mathbf{M}_{ij} & \xrightarrow[\text{(i,j) cycling}]{\text{Ritz expansion}} \mathbf{M} \\
\mathbf{K}_{ij} & \xrightarrow[\text{(i,j) cycling}]{\text{Ritz expansion}} \mathbf{K}
\end{aligned}$$

Finally - after applying a similar procedure to compute the load vector - the governing equations in the classical form are obtained.

$$\mathbf{M}\ddot{\mathbf{u}} + \mathbf{K}\mathbf{u} = \mathbf{L}^{\text{top}} f_0^{\text{top}} + \mathbf{L}^{\text{bot}} f_0^{\text{bot}} \quad (2.83)$$

### 2.5.6 Equivalent single degree of freedom model

The S-GUF model described above can be used to simulate the dynamic response of a wide class of plates with different boundary conditions. However, for some specific purposes, it could be enough to use a much simpler model, in order to gain insight on the problem without being confused by the complete complex dynamics well described by the S-GUF model.

As a matter of fact, in Chapter 4 some considerations will be drawn looking firstly at a simple equivalent *single degree of freedom* (SDOF) plate model.

The adopted mathematical description is the same derived by Di Girolamo in [11], where only the first natural mode of the plate is described with a simple mass-spring-dashpot model.

## 2.6 SDOF plate model with one inertial actuator

The SDOF model of the plate consist in a simple mass  $m_s$ , connected to the ground by mean of a spring of elastic constant  $k_s$  and a dashpot of damping coefficient  $c_s$ . It's immediate to notice the similarity with the mechanical part of the lumped parameter

model of the actuator described at the beginning of this chapter. Thanks to this similarity the dynamics equations governing the coupled system can be derived in the same way described before, just modifying the system as show in Figure 2.7.

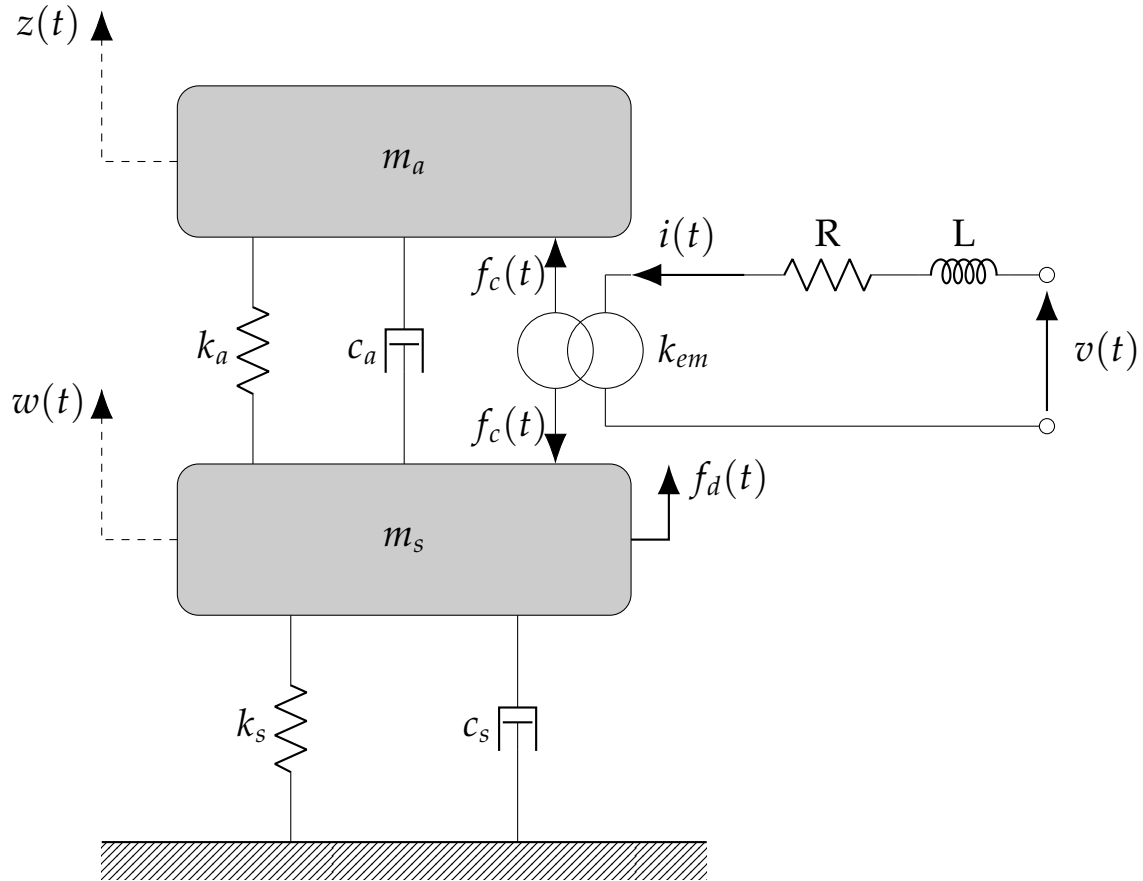


Figure 2.7: Schematic of the SDOF plate model with an installed inertial actuator.

### 2.6.1 Dynamics equations

The coupled model is composed by a single degree of freedom mass-spring-dashpot system representing the plate, on top of which is mounted the inertial actuator, modeled as described before.

The dynamics equations can be derived again through the Lagrange formalism, taking care to add the terms due to the new plate degree of freedom. The energetic quantities are modified as follows.

$$T^* = \frac{1}{2}m_a\dot{z}^2 + \frac{1}{2}m_s\dot{w}^2 \quad \text{Complementary kinetic energy} \quad (2.84)$$

$$V = \frac{1}{2}k_a(z - w)^2 + \frac{1}{2}k_s w^2 \quad \text{Potential energy} \quad (2.85)$$

$$W_m^* = \frac{1}{2}L\dot{q}^2 + k_{em}(z - w)\dot{q} \quad \text{Complementary magnetic energy} \quad (2.86)$$

$$\mathcal{D} = \frac{1}{2}c_a(\dot{z} - \dot{w})^2 + \frac{1}{2}c_s\dot{w}^2 + \frac{1}{2}R\dot{q}^2 \quad \text{Dissipation function} \quad (2.87)$$

$$\delta W_{nc} = \delta w f_d + \delta q v \quad \text{Virtual work by non-conservative forces} \quad (2.88)$$

Where

$m_s$	Equivalent mass of the plate	[kg]
$c_s$	Equivalent damping of the plate	[Ns m <sup>-1</sup> ]
$k_s$	Equivalent suspension stiffness of the plate	[N m <sup>-1</sup> ]
$m_a$	Proof mass of the actuator	[kg]
$c_a$	Damping of the actuator	[Ns m <sup>-1</sup> ]
$k_a$	Suspension stiffness of the actuator	[N m <sup>-1</sup> ]
$R$	Coil resistance	[Ω]
$L$	Coil inductance	[H]
$k_{em}$	Electromagnetic coupling factor	[NA <sup>-1</sup> ]
$q(t)$	Electric charge in the coil	[F]
$i(t)$	Electric current flowing in the coil	[A]
$v(t)$	Electric voltage source	[V]
$f_d(t)$	Disturbance acting on the plate	[N]
$z(t)$	Absolute displacement of the proof mass	[m]
$w(t)$	Absolute displacement of plate degree of freedom	[m]

The Lagrangian of the system is defined as:

$$\mathcal{L} = T^* - V + W_m^* = \frac{1}{2}m_a\dot{z}^2 + \frac{1}{2}m_s\dot{w}^2 - \frac{1}{2}k_a(z - w)^2 - \frac{1}{2}k_s(w)^2 + \frac{1}{2}L\dot{q}^2 + k_{em}(z - w)\dot{q} \quad (2.89)$$

The Lagrange's equations read:

$$\begin{cases} \frac{d}{dt} \left( \frac{\partial \mathcal{L}}{\partial \dot{w}} \right) - \frac{\partial \mathcal{L}}{\partial w} + \frac{\partial \mathcal{D}}{\partial \dot{w}} = Q_w \\ \frac{d}{dt} \left( \frac{\partial \mathcal{L}}{\partial \dot{z}} \right) - \frac{\partial \mathcal{L}}{\partial z} + \frac{\partial \mathcal{D}}{\partial \dot{z}} = Q_z \\ \frac{d}{dt} \left( \frac{\partial \mathcal{L}}{\partial \dot{q}} \right) - \frac{\partial \mathcal{L}}{\partial q} + \frac{\partial \mathcal{D}}{\partial \dot{q}} = Q_q \end{cases} \quad (2.90)$$

Leading to the following dynamics equations.

$$\begin{cases} m_s \ddot{w}(t) + (c_s + c_a) \dot{w}(t) + (k_s + k_a) w(t) - c_a \dot{z}(t) - k_a z(t) + k_{em} \dot{q}(t) = f_d \\ m_a \ddot{z}(t) + c_a [\dot{z}(t) - \dot{w}(t)] + k_a [z(t) - w(t)] - k_{em} \dot{q}(t) = 0 \\ L \dot{q}(t) + R \dot{q}(t) + k_{em} [z(t) - w(t)] = v(t) \end{cases} \quad (2.91)$$

That can be rewritten considering  $\dot{q}(t) = i(t)$  as:

$$\begin{cases} m_s \ddot{w}(t) + (c_s + c_a) \dot{w}(t) + (k_s + k_a) w(t) - c_a \dot{z}(t) - k_a z(t) + k_{em} i(t) = f_d \\ m_a \ddot{z}(t) + c_a [\dot{z}(t) - \dot{w}(t)] + k_a [z(t) - w(t)] - k_{em} i(t) = 0 \\ L \dot{i}(t) + R i(t) + k_{em} [z(t) - w(t)] = v(t) \end{cases} \quad (2.92)$$

The first equation describes the mechanical behavior of the SDOF plate, the second describes the dynamic of the actuator and the third is referred to the dynamics of the electrical part.

## 2.6.2 State space realization

$$\text{Defining:} \quad \begin{cases} x_1 = w \\ x_2 = z \\ x_3 = \dot{w} \\ x_4 = \dot{z} \\ x_5 = i \end{cases} \quad \begin{cases} u = v_a \\ u_d = f_d \end{cases} \quad (2.93)$$

The previous set of equation (Eq. 2.92) can be written in state space, obtaining five first order differential equations, as follows:

$$\begin{cases} \dot{x}_1 = x_3 \\ \dot{x}_2 = x_4 \\ \dot{x}_3 = -\frac{k_s + k_a}{m_s}x_1 + \frac{k_a}{m_s}x_2 - \frac{c_s + c_a}{m_s}x_3 + \frac{c_a}{m_s}x_4 - \frac{k_{em}}{m_s}x_5 + \frac{1}{m_s}u_d \\ \dot{x}_4 = \frac{k_a}{m_a}x_1 - \frac{k_a}{m_a}x_2 + \frac{c_a}{m_a}x_3 - \frac{c_a}{m_a}x_4 + \frac{k_{em}}{m_a}x_5 \\ \dot{x}_5 = \frac{k_{em}}{L}x_3 - \frac{k_{em}}{L}x_4 - \frac{R}{L}x_5 + \frac{1}{L}u \end{cases} \quad (2.94)$$

$$\begin{bmatrix} \dot{x}_1 \\ \dot{x}_2 \\ \dot{x}_3 \\ \dot{x}_4 \\ \dot{x}_5 \end{bmatrix} = \begin{bmatrix} 0 & 0 & 1 & 0 & 0 \\ 0 & 0 & 0 & 1 & 0 \\ -\frac{k_s + k_a}{m_s} & \frac{k_a}{m_s} & -\frac{c_s + c_a}{m_s} & \frac{c_a}{m_s} & -\frac{k_{em}}{m_s} \\ \frac{k_a}{m_a} & -\frac{k_a}{m_a} & \frac{c_a}{m_a} & -\frac{c_a}{m_a} & \frac{k_{em}}{m_a} \\ 0 & 0 & \frac{k_{em}}{L} & -\frac{k_{em}}{L} & -\frac{1}{L} \end{bmatrix} \begin{bmatrix} x_1 \\ x_2 \\ x_3 \\ x_4 \\ x_5 \end{bmatrix} + \begin{bmatrix} 0 \\ 0 \\ 0 \\ 0 \\ \frac{1}{L} \end{bmatrix} u + \begin{bmatrix} 0 \\ 0 \\ \frac{1}{m_s} \\ 0 \\ 0 \end{bmatrix} u_d \quad (2.95)$$

That can be written in the form:

$$\dot{x} = Ax + B_u u + B_d u_d \quad (2.96)$$

Where

$$A = \begin{bmatrix} 0 & 0 & 1 & 0 & 0 \\ 0 & 0 & 0 & 1 & 0 \\ -\frac{k_s + k_a}{m_s} & \frac{k_a}{m_s} & -\frac{c_s + c_a}{m_s} & \frac{c_a}{m_s} & -\frac{k_{em}}{m_s} \\ \frac{k_a}{m_a} & -\frac{k_a}{m_a} & \frac{c_a}{m_a} & -\frac{c_a}{m_a} & \frac{k_{em}}{m_a} \\ 0 & 0 & \frac{k_{em}}{L} & -\frac{k_{em}}{L} & -\frac{1}{L} \end{bmatrix} \quad B_u = \begin{bmatrix} 0 \\ 0 \\ 0 \\ 0 \\ \frac{1}{L} \end{bmatrix} \quad B_d = \begin{bmatrix} 0 \\ 0 \\ \frac{1}{m_s} \\ 0 \\ 0 \end{bmatrix} \quad (2.97)$$



# Chapter 3

## Experimental Characterization

In this chapter the generic mathematical models derived previously, are completed with the computation of all the involved parameters and validated comparing experimental and numerical results. Some experiments are therefore carried out on each single component, firstly with the aim of computing the characteristic parameters, secondly to assess the validity of the mathematical models.

### 3.1 Inertial actuators: Dayton DAEX25VT-4 exciters



*Figure 3.1: Dayton DAEX25VT-4.*

In this work the Dayton DAEX25VT-4 electrodynamic exciters (Figure 3.1) are employed as low cost proof-mass actuators. They are small vibration speakers, with high

sensibility and low power requirements if compared to similar size exciters. Their efficiency is due to the neodymium magnets used to create maximum magnetic flux around the voice coil, allowing the speakers to be driven also by small and cheap audio amplifiers, as done in this thesis. The transducer are provided with pre-applied 3M VHB (Very High Bond), but here some Loctite SuperAttak has been added to ensure maximum energy transfer between the speaker and the plate surface.

The characterization of the inertial actuators consists in the estimation of the free parameters described in Chapter 2, reported here for the sake of clarity:

- $m_a$ : proof mass of the actuator
- $c_a$ : damping coefficient of the suspension of the proof-mass
- $k_a$ : suspension stiffness of the proof-mass
- $R$ : total equivalent internal resistance of the electrical system of the actuator
- $L$ : total equivalent internal inductance of the electrical system of the actuator
- $k_{em}$ : electromagnetic coupling factor

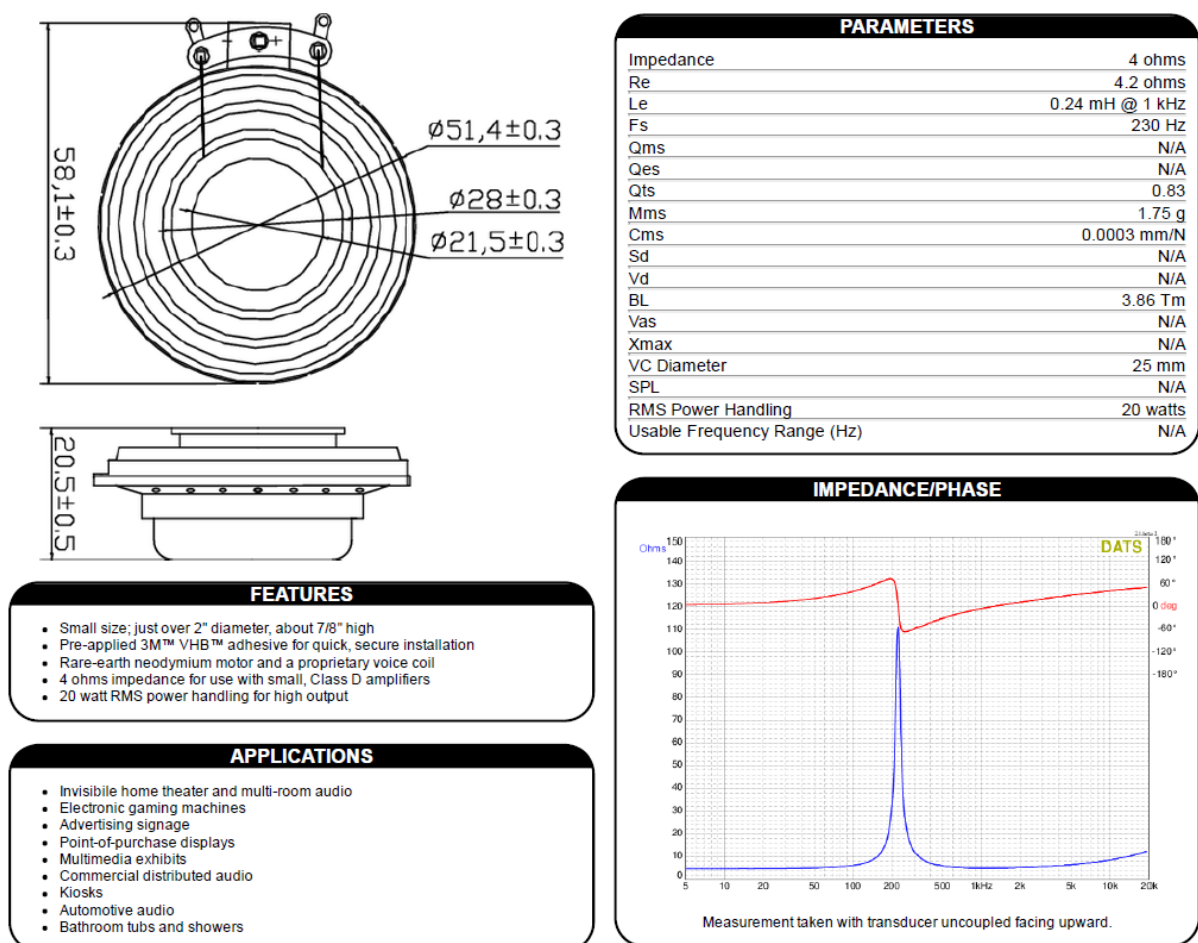


Figure 3.2: Dayton DAEX25VT-4 electrodynamic exciters: manufacturer specifications.



The characterization is carried out following the same procedure as in [11], measuring some physical quantities strictly dependent on the above parameters. The main difference here is that instead of considering only the proof mass acceleration response in the voltage driven case, also the acceleration response in the current driven case and the electrical input impedance will be computed. The aim of such a redundant approach is firstly to assess how much the values obtained are dependent on the method used to compute them, secondly - in the case slightly different results are obtained - to average the values.

The three approaches are similar in the procedure, but due to the different transfer function by which they are described, they allow to estimate a different number of parameters. In particular, the proof-mass acceleration response in the current driven case allows to retrieve the three mechanical parameters:  $m_a$ ,  $c_a$  and  $k_a$ , while in the voltage driven case also the inductance  $L$  is computable. The electrical impedance gives the resistance  $R$  in addition to all the previous, but in any case the electromagnetic coupling factor  $k_{em}$  has to be obtained from the datasheet in Figure 3.2. How the parameters are computed and why their number change will be cleared in the following.

The experimental setup is kept the same for any of the three analysis performed. It is composed as in Figure 3.3: a desktop PC generates a digital signal and converts it to analog through the PCI-6213 digital-to-analog converter. The PCI-MIO-16E-1 board, instead, is responsible for the analog-to-digital conversion of all the quantities that the PC shall acquire. All PC performed operations are done with a 20kHz sampling frequency. BNC-2110 and BNC-2090 are adapters that allow to connect BNC cables to the PC boards and do not modify in any way the signal coming across them. The analog signal produced by the PC is first filtered with the KEMO BENCH-MASTER 21M filter to limit its bandwidth to 10kHz, and then fed to the audio amplifier (LEPAI LP-2020A+) that, dependently on the setting of the volume knob, amplifies its input voltage.

The output tension of the audio amplifier is directly applied to the terminals of the inertial actuators, this voltage is also measured and sent to the acquisition board by the PICO TA043 differential probe. In this chapter, whenever input voltage is named without other clarifications, reference is always made to the tension provided as input to the speaker by the audio amplifier. In theory the direct measure of such a tension would not be required in this phase, because it could have been reconstructed knowing the output from the PC board and the transfer function that describes the amplifier behaviour; in practice it has been chosen to acquire it, in order to eliminate as much as possible any source of errors.

One of the cables that connect the amplifier to the speaker is severed by the LPRS 6-NP current transducer; it maps the current to be measured in a tension at its exit pins, proportional to the current as  $V_{out}(t) = 2.5 + 0.417 i(t)$ . Such tension is acquired by the data acquisition system.

The acceleration of the proof-mass is measured by means of a small PCB 333B32 accelerometer of mass 4g, glued on top of the actuator.

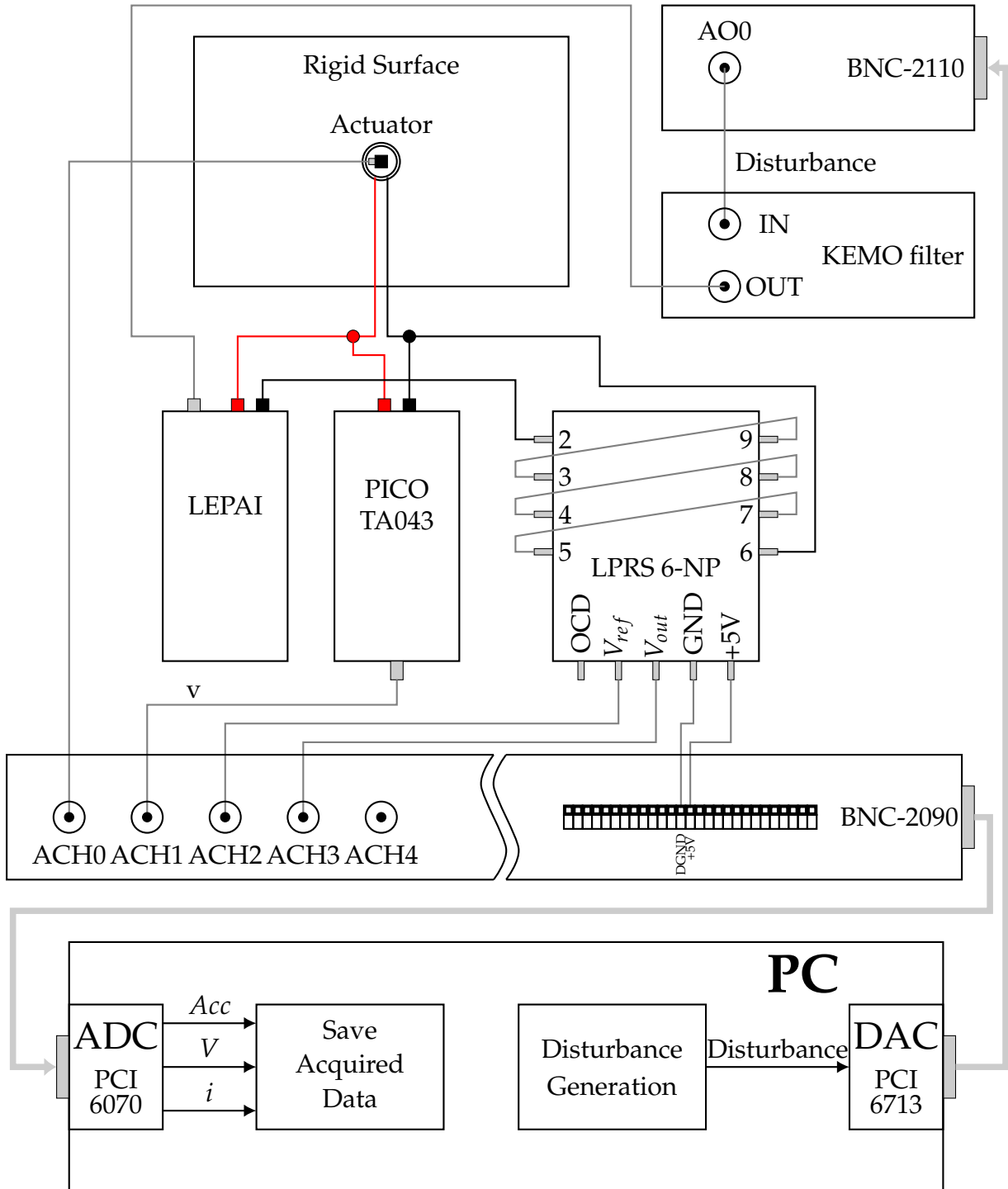


Figure 3.3: Scheme of the experimental setup adopted for the actuators characterization.

### 3.1.1 Proof-mass acceleration response

The proof-mass acceleration response describes the relationship between the acceleration of the suspended mass of the inertial actuator and the electrical input, that can be both current or tension. For the sake of clarity it must be pointed out that the system under analysis can be strictly considered as voltage driven, since the controllable

quantity is the voltage and no method to achieve direct control of the current has been applied. However, since both voltage and current are measured, it's possible to seek the relationship between current and acceleration of the proof-mass, as it would have been done if the actuator was current driven.

### Voltage driven

In this section the voltage driven case is presented while the current driven will be briefly discussed later, mainly for comparative purposes. Note that the procedure outlined in the following is rather general: it has been applied also to the current driven acceleration response and to the electrical impedance, with only minor modifications.

The frequency response function is computed using as input a random white noise, filtered by the KEMO BENCH-MASTER to limit it's bandwidth to 0 – 10kHz. It can be computed as:

$$H_{aV}(j\omega) = \frac{S_{aV}(\omega)}{S_{VV}(\omega)}$$

where  $S_{aV}(\omega)$  is the cross spectral density of the voltage  $V$  and acceleration of the proof mass  $a$ , and  $S_{VV}(\omega)$  is the power spectral density of  $V$ .

Such elaboration of the acquired data has been performed using the MATLAB function `tfestimate`. It takes as inputs the time series of two quantities and reconstruct the input-output relation in the frequency domain. The results for the two Dayton devices used in this work are reported in Figure 3.4.

The acceleration response obtained above still lacks a clear link with the parameters needed for the complete characterization of the inertial actuator. What has to be done is to find the coefficients of a transfer function that gives a frequency response such as the one obtained with `tfestimate`. Once it is done, the transfer function can be compared with the analytical acceleration response  $\tilde{H}_{aV}$  - derived in Chapter 2 and reported in Eq. 3.1 with the addition of the accelerometer mass  $m_s$  - and the speakers' lumped model's parameters can be computed.

$$\tilde{H}_{aV}(s) = \frac{s^2 k_{em}}{(R + sL)(s^2(m_a + m_s) + sc_a + k_a) + sk_{em}} \quad (3.1)$$

Eq. 3.1 can be rewritten highlighting the coefficients of the complex variable, keeping in mind that for the next passages is needed to have the highest order coefficient of the denominator equal to one.

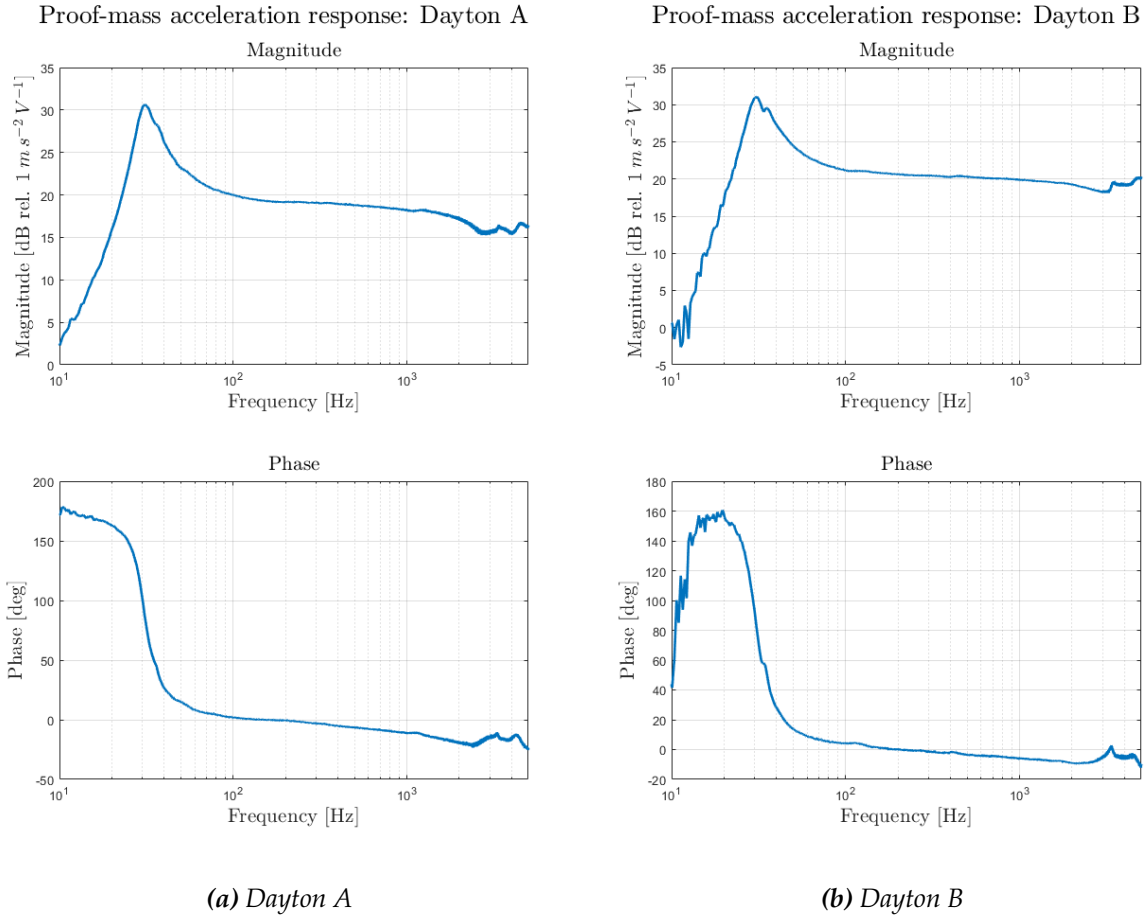


**Figure 3.4:** Proof-mass acceleration response computed from experimental data for Dayton A and B.

$$\tilde{H}_{aV}(s) = \frac{\left(\frac{k_{em}}{L(m_a + m_s)}\right) s^2}{s^3 + \left(\frac{R(m_a + m_s) + Lc_a}{L(m_a + m_s)}\right) s^2 + \left(\frac{Lk_a + Rc_a + k_{em}^2}{L(m_a + m_s)}\right) s + \left(\frac{Rk_a}{L(m_a + m_s)}\right)} \quad (3.2)$$

If  $H_{aV}(j\omega)$  is truly represented by the lumped parameter model  $\tilde{H}_{aV}(s)$ , it should be possible to find  $\hat{H}_{aV}(s)$  in Eq. 3.3, such that the coefficients  $b_i$  and  $a_i$  can be determined minimizing a suitable measure of the difference between  $H_{aV}(j\omega)$  and  $\hat{H}_{aV}(s)$ .

$$\hat{H}_{aV}(s) = \frac{b_2 s^2}{a_3 s^3 + a_2 s^2 + a_1 s + a_0} \quad (3.3)$$

This can be done, for example, with a least-square fitting algorithm, that tries to determine the coefficients  $a_i$  and  $b_i$  of a generic transfer function  $\hat{H}(s)$  with  $m$  zeros and  $n$

poles.

$$\hat{H}(s) = \frac{b_m s^m + b_{m-1} s^{m-1} + \dots + b_1 s + b_0}{a_n s^n + a_{n-1} s^{n-1} + \dots + a_1 s + a_0} \quad (3.4)$$

A possible scheme for such an algorithm is reported in Eq. 3.5:

$$\min_{b,a} \sum_{k=1}^n \omega_k \left| H_{aV}(j\omega_k) - \frac{B(j\omega_k)}{A(j\omega_k)} \right| \quad (3.5)$$

This task has been performed with the MATLAB `invfreqs` function, specifying the as desired order of the numerator and denominator respectively  $m = 2$  and  $n = 3$ . Eq. 3.6 reports the results for the two actuators employed:

$$\hat{H}_{aV}(s) = \begin{cases} \frac{1.9579e5s^2}{s^3 + 2.1191e4s^2 + 1.0892e6s + 7.9675e8} & (\text{DaytonA}) \\ \frac{2.5573e5s^2}{s^3 + 2.4291e4s^2 + 1.2993e6s + 8.1890e8} & (\text{DaytonB}) \end{cases} \quad (3.6)$$

Comparing Eq. 3.2 and Eq. 3.6 it's evident that four coefficients allow to compute only four parameters, while total number is six. This means that two of them shall be obtained in another way. The easiest choice is to take  $k_{em}$  and  $R$  from the actuator datasheet while computing the other four. Results are reported in Table 3.1 and in Figure 3.5  $H_{aV}(j\omega)$  and  $\hat{H}_{aV}(s)$  are superimposed.

Device	$m_a$ [g]	$c_a$ [Ns/m]	$k_a$ [N/m]	$L$ [H]	$R$ [ $\Omega$ ]	$k_{em}$ [N/A]
Dayton A	0.0830	1.2152	3272.6	0.000192	4.2000	3.8600
Dayton B	0.0723	0.8758	2575.1	0.000218	4.2000	3.8600

**Table 3.1:** Parameters computed through the voltage driven proof-mass acceleration response approach, for both the Dayton exciters. Those on the right end of the table are assumed from the datasheet.

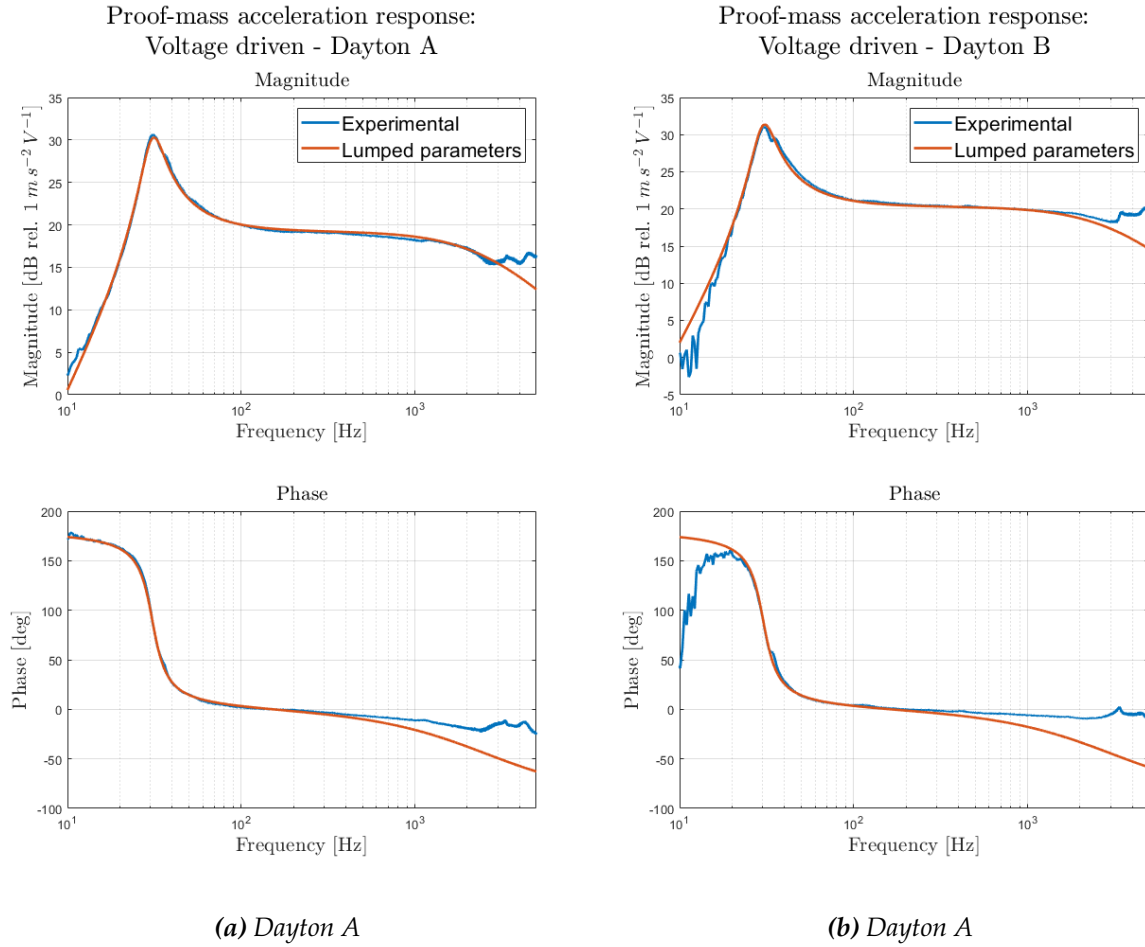


**Figure 3.5:** Comparison of the proof-mass acceleration response computed from experimental data ( $H_{aV}(j\omega)$ ) and the lumped parameters model ( $\hat{H}_{aV}(s)$ ), for Dayton A and B.

### Current driven

The current driven proof-mass acceleration response is defined as:

$$H_{ai}(j\omega) = \frac{S_{ai}(\omega)}{S_{ii}(\omega)}$$

It allows to compute only three of the six parameters of the actuator's model. This can be understood looking at its expression derived in Chapter 2 and reported for the sake of clarity in Eq. 3.7.

$$\tilde{H}_{ai}(s) = \frac{s^2 k_{em}}{(m_a + m_s)s^2 + c_a s + k_a} \quad (3.7)$$

Eq. 3.7 can be rewritten highlighting the coefficients of the frequency variable, keeping in mind that `invfreqs` gives back a transfer function with the highest order coefficient of the denominator equal to one.

$$\tilde{H}_{ai}(s) = \frac{\left(\frac{k_{em}}{m_a + m_s}\right) s^2}{s^2 + \left(\frac{c_a}{m_a + m_s}\right) s + \left(\frac{k_a}{m_a + m_s}\right)} \quad (3.8)$$

If  $H_{ai}(j\omega)$  is truly represented by the lumped parameter model  $\tilde{H}_{ai}(s)$ , it should be possible to find  $\hat{H}_{ai}(s)$  in Eq. 3.9, such that the coefficients  $b_i$  and  $a_i$  can be determined minimizing a suitable measure of the difference between  $H_{ai}(j\omega)$  and  $\hat{H}_{ai}(s)$ .

$$\hat{H}_{ai}(s) = \frac{b_2 s^2}{a_2 s^2 + a_1 s + a_0} \quad (3.9)$$

The computation of  $a_i$  and  $b_i$  and the derivation of the model parameters is straightforward and leads to the result reported in Table 3.2.

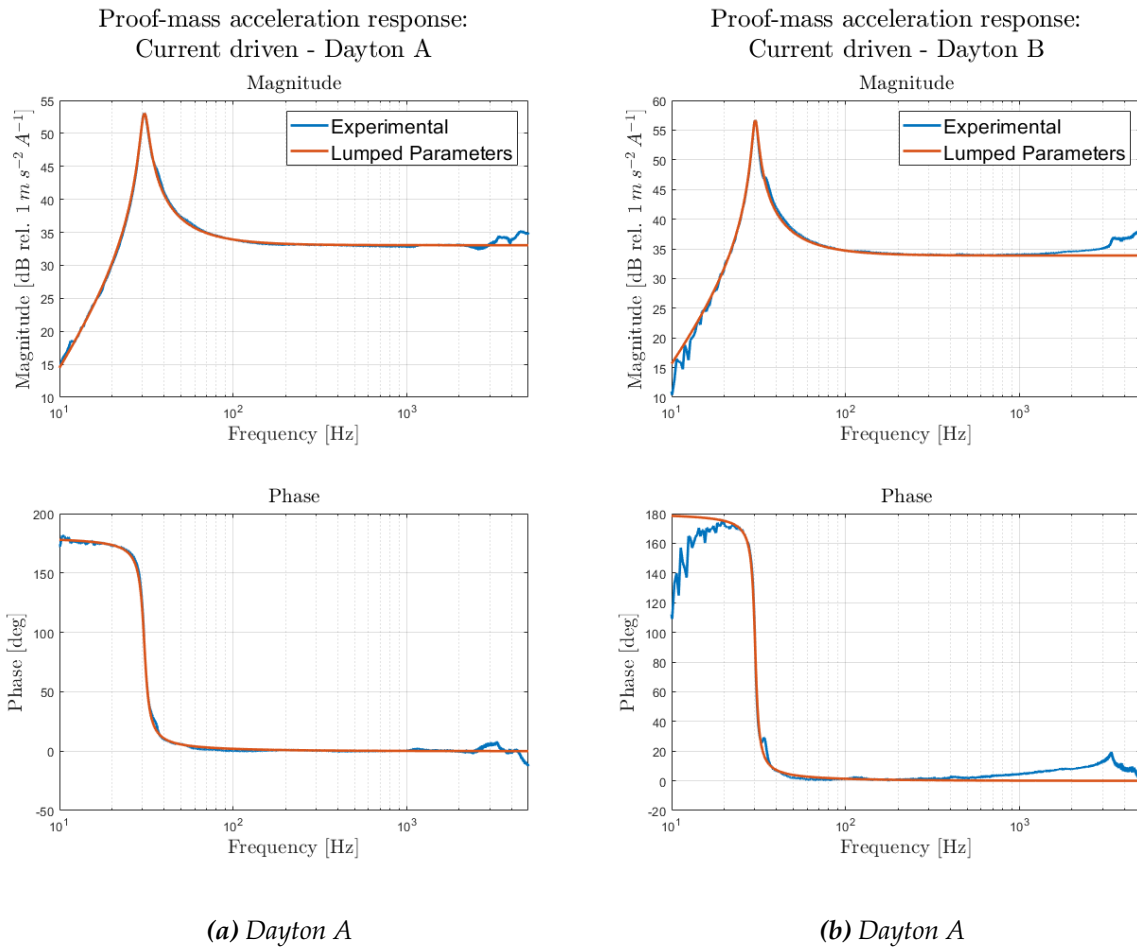


**Figure 3.6:** Comparison of the proof-mass acceleration response computed from experimental data ( $H_{ai}(j\omega)$ ) and the lumped parameters model ( $\hat{H}_{ai}(s)$ ), for Dayton A and B.

Device	$m_a$ [g]	$c_a$ [Ns/m]	$k_a$ [N/m]	$R$ [ $\Omega$ ]	$L$ [H]	$k_{em}$ [N/A]
Dayton A	0.0816	1.3417	3195.3	4.2000	0.00024	3.8600
Dayton B	0.0725	0.8085	2581.4	4.2000	0.00024	3.8600

**Table 3.2:** Parameters computed through the current driven proof-mass acceleration response approach, for both the Dayton exciters. Those on the right end of the table are assumed from the datasheet.

### 3.1.2 Electrical input impedance

The electrical input impedance is defined as:

$$H_{Vi}(j\omega) = \frac{S_{Vi}(\omega)}{S_{ii}(\omega)}$$

Its expression has been derived in Chapter 2 and is reported for the sake of clarity in Eq. 3.10.

$$\tilde{H}_{Vi}(s) = \frac{(R + sL)((m_a + m_s)s^2 + c_a s + k_a) - k_{em}^2 s}{(m_a + m_s)s^2 + c_a s + k_a} \quad (3.10)$$

Eq. 3.10 can be rewritten highlighting the coefficients of the frequency variable, keeping in mind that `invfreqs` gives back a transfer function with the highest order coefficient of the denominator equal to one.

$$\tilde{H}_{Vi}(s) = \frac{(L)s^3 + \left(\frac{R(m_a + m_s) + Lc_a}{m_a + m_s}\right)s^2 + \left(\frac{Rc_a + Lk_a - k_{em}^2}{m_a + m_s}\right)s + \left(\frac{Rk_a}{m_a + m_s}\right)}{s^2 + \left(\frac{c_a}{m_a + m_s}\right)s + \left(\frac{k_a}{m_a + m_s}\right)} \quad (3.11)$$

If  $H_{Vi}(j\omega)$  is truly represented by the lumped parameter model  $\tilde{H}_{Vi}(s)$ , it should be possible to find  $\hat{H}_{Vi}(s)$  in Eq. 3.12, such that the coefficients  $b_i$  and  $a_i$  can be determined minimizing a suitable measure of the difference between  $H_{Vi}(j\omega)$  and  $\hat{H}_{Vi}(s)$ .

$$\hat{H}_{Vi}(s) = \frac{b_3 s^3 + b_2 s^2 + b_1 s + b_0}{a_2 s^2 + a_1 s + a_0} \quad (3.12)$$

Proceeding in the same way as done for the voltage driven proof-mass acceleration response the values reported in Table 3.3 are obtained.



Device	$m_a$ [g]	$c_a$ [Ns/m]	$k_a$ [N/m]	$R$ [ $\Omega$ ]	$L$ [H]	$k_{em}$ [N/A]
Dayton A	0.0859	1.4040	3353.7	4.8206	0.00026	3.8600
Dayton B	0.0745	0.8262	2645.9	4.8094	0.00023	3.8600

**Table 3.3:** Parameters computed through the electrical input impedance approach, for both the Dayton exciters. Those on the right end of the table are assumed from the datasheet.

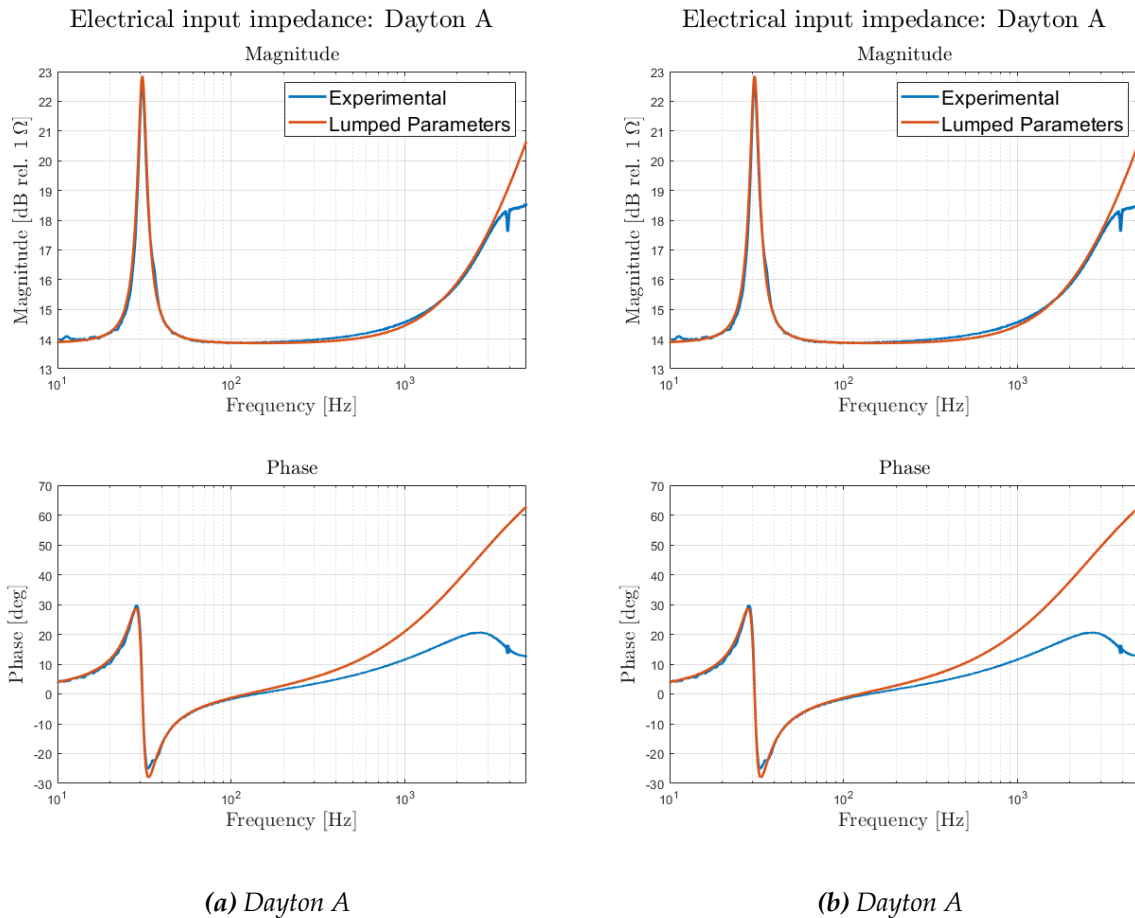


**Figure 3.7:** Comparison of the electrical input impedance computed from experimental data ( $H_{Vi}(j\omega)$ ) and the lumped parameters model ( $\hat{H}_{Vi}(s)$ ), for Dayton A and B.

The superposition of each experimental frequency responses to the related analytical lumped parameters model, shows that the model gives a good description of the underlying physics. The magnitude approximation is very good in a wide range spanning at least from 20 to 2000Hz. The frequency description is a little less satisfactory at higher frequencies.

Looking at the parameters obtained with the three methods and reported in Tables 3.1, 3.2 and 3.3, it can be noticed that the results slightly differ from one method to another. If the purpose was only to build a numerical model to simulate the dynamics of the ex-

perimental prototype, such a small uncertainty on the parameters would not be a big concern. This could be verified computing each of the three transfer functions using all the three sets of parameters and checking that - indeed - only minor differences are obtained. This is not the only purpose though, as shown in Chapter 4 these six parameters are used to reconstruct the plate velocity through a transfer function that is highly prone to errors, if the parameters are even only a bit wrong. Thus has been necessary to average them - and also to tune them through trial and error - to achieve the best possible performances. The final values used in the real-time laboratory simulation are reported in Table 3.4.

Device	$m_a$ [g]	$c_a$ [Ns/m]	$k_a$ [N/m]	$R$ [ $\Omega$ ]	$L$ [H]	$k_{em}$ [N/A]
Dayton A	0.0819	1.6620	3218.0	4.7000	0.00022	3.8600
Dayton B	0.0745	0.8262	2645.9	4.8094	0.00023	3.8600

*Table 3.4: Parameters used for the real-time simulation.*

## 3.2 Current sensor

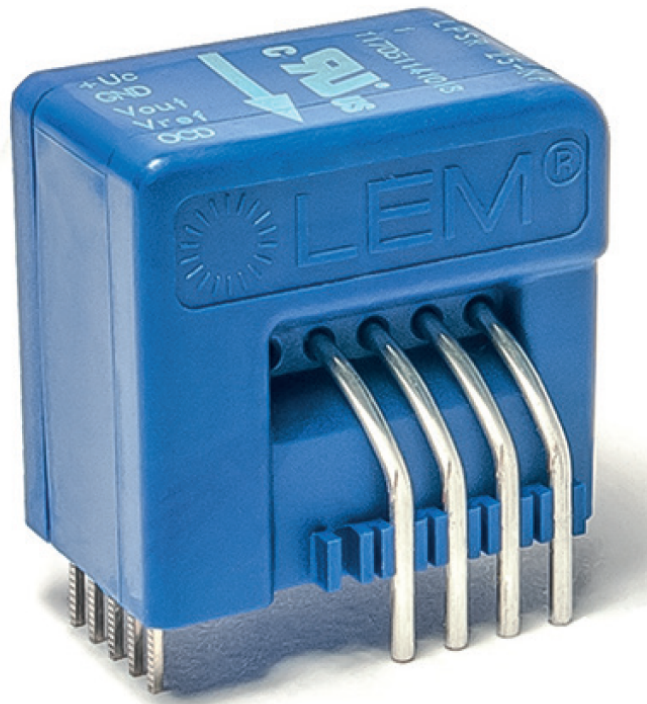


*Figure 3.8: Current sensor.*

While the voltage acquisition has been done thanks to the differential probe PICO TA043, already present in laboratory and used in [11, 32], for the current acquisition no probes were available. Since active current probes, such the PICO TA189, have prices

of hundreds of euros, it has been chosen to buy a simple and cheap electronic current transducer to be soldered on a breadboard (Figure 3.9).

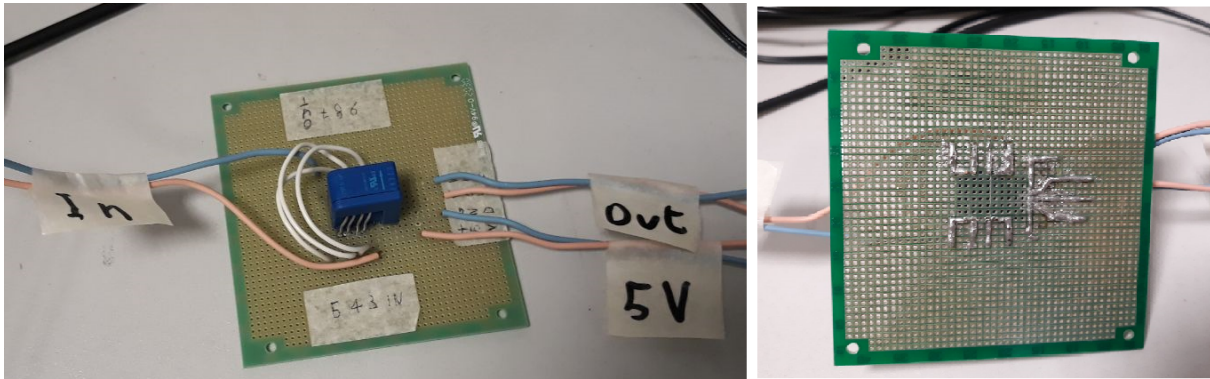


Figure 3.9: Current transducer installed on the breadboard, front and rear.

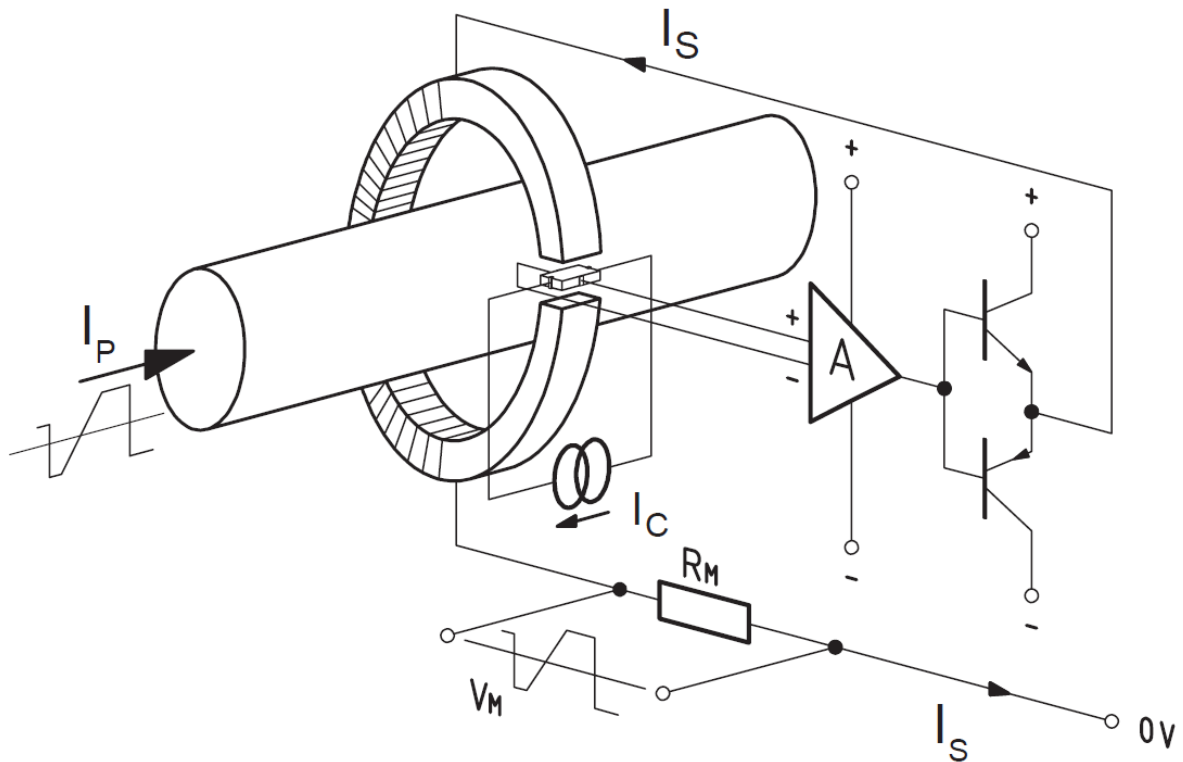


Figure 3.10: Hall effect current sensor generic scheme.

The chosen current transducer is the LEM LPSR 6-NP, (Figure 3.8) a closed loop Hall effect current transducer. Hall effect is created by Lorentz force,  $F_L = q \cdot (V \times B)$ , which acts on charges moving through a magnetic field. The current to be measured -  $I_P$  in Figure 3.10 - passes inside the transducer and generates a magnetic field that is amplified by the annular magnetic core. Such core has a small gap, inside which is placed a Hall generator: a small sheet of conducting material traversed by a control current -  $I_C$  in Figure 3.10, parallel to  $I_P$  - provided by the power supply of the sensor. When

the charge carriers of a such a constant current cross the gap in the magnetic core, they interact with the magnetic field being deviated by the Lorentz force and generating a voltage difference proportional to the magnetic field in the core. Within the linear region of the hysteresis loop (Figure 3.11) of the material used for the magnetic circuit, the magnetic flux density,  $B$ , is proportional to the primary current,  $I_p$ . Therefore the output of the Hall generator is proportional to the primary current.

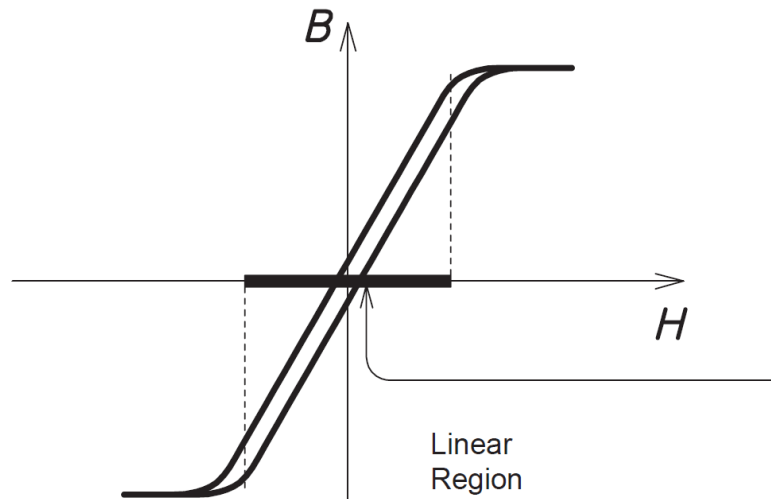


Figure 3.11: Hysteresis curve.

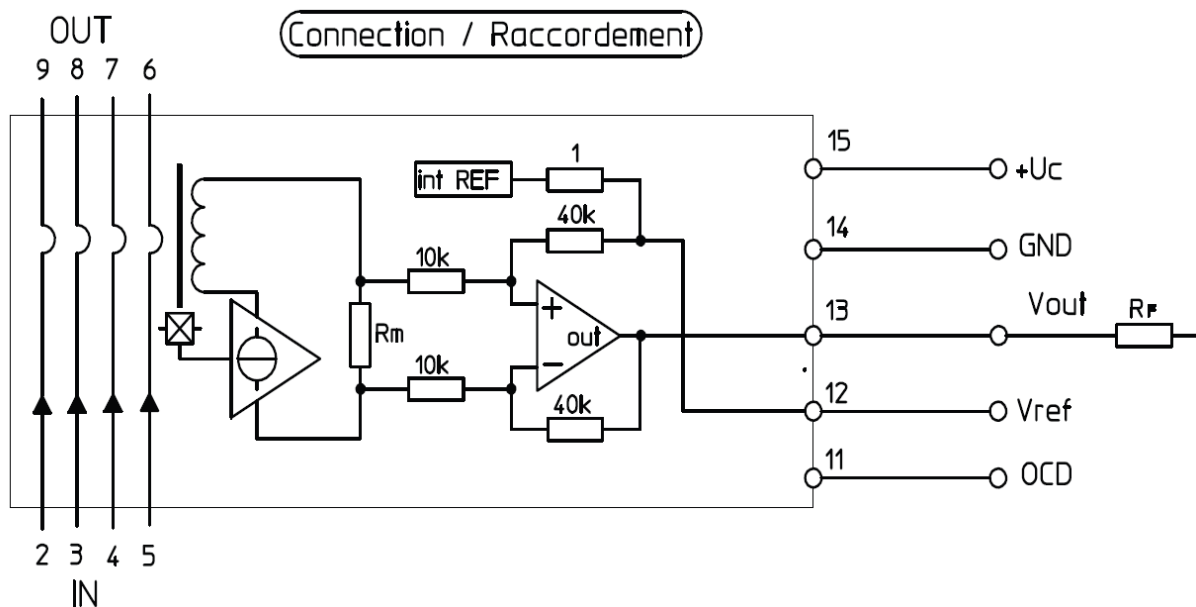


Figure 3.12: Current sensor connection scheme.

The transducer works with a DC power supply of 5V and the output voltage is offset by 2.5V in order to have a symmetric AC field of measure with a simple DC power supply. An electrical scheme of the transducer is reported in Figure 3.12.

Pins 2 and 6 are respectively input and output of the primary circuit in which the current to be measured shall flow. Pins from 2 to 9 can be connected among them in four different ways in order to change the transducer sensitivity, as summarized in Figure 3.13.

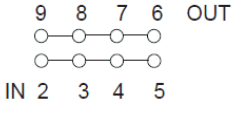
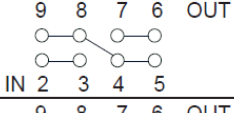
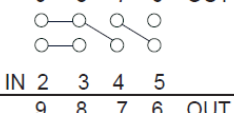
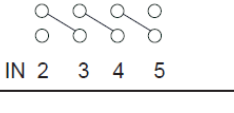
Number of primary turns	Primary Nominal RMS current	Output voltage $V_{out}$	Primary resistance $R_p$ [m $\Omega$ ]	Recommended connections
1	$\pm I_{PN}$	$V_{ref} \pm 0.625$	0.18	
2	$\pm I_{PN}/2$	$V_{ref} \pm 0.625$	0.72	
3	$\pm I_{PN}/3$	$V_{ref} \pm 0.625$	1.8	
4	$\pm I_{PN}/4$	$V_{ref} \pm 0.625$	2.88	

Figure 3.13: Current sensor sensitivity connection scheme.

The remaining pins, from 15 to 11, are respectively:

- +5V - Power input.
- GND - Reference voltage for all other pins.
- $V_{out}$  - Output voltage, proportional to the current to be measured through the following formula

$$V_{out} = V_{ref} + 0.625 \frac{N_p \cdot I}{I_{PN}}$$

Where  $I_{PN} = 6A$  and  $N_p$  can take values from 1 to 4 depending on the connection scheme of pins from 2 to 9. The configuration that will be used is the one for the maximum sensitivity with  $N_p = 4$ .

- $V_{ref}$  - Measure offset, equal to 2.5V.
- OCD - OverCurrent Detection, normally placed to 0V, apart from when the flowing current in the primary is greater than  $4.1 \cdot I_{PN}$ . The aim is to signal that the sensor is in saturation and therefore the measure is no more reliable. Considering that the limit current is 24A there will be no need for this pin.

The reading of the sensor could be made acquiring only  $V_{out}$  and subtracting 2.5V. However, as recommended by the manufacture and confirmed experimentally, by acquiring also  $V_{ref}$  the accuracy is increased.

### 3.3 Power amplifiers

The amplifiers used in this thesis to drive the Dayton speakers are the Lepai LP-2020A+, Figure 3.14. They are ultracheap mini amplifiers that can provide up to 20W per channel. They have one 3.5mm minijack input and a volume control knob.



Figure 3.14: Lepai LP-2020A+.

The amplifiers used in this work are the same of Ref. [11], namely number 1 and 2. Although the parameters of the amplifiers were available in the reference, the characterization has been performed again, since the required experimental setup (Figure 3.15) is much similar to that used to characterize the actuators. The only significant difference is that also the disturbance has to be acquired in order to compute, with  $t_{festimate}$ , the amplifier's transfer function.

$$H_{amp}(j\omega) = \frac{S_{Vd}(\omega)}{S_{dd}(\omega)}$$

$S_{Vd}(\omega)$  is the cross spectral density of the output voltage  $V$  and the input voltage - the disturbance -  $d$ , whereas  $S_{dd}(\omega)$  is the power spectral density of the disturbance. The parameter of the amplifier can now be obtained exactly as before, comparing the experimental transfer function with the assumed model derived in Chapter 2 and reported in Eq. 3.13 for the sake of clarity:

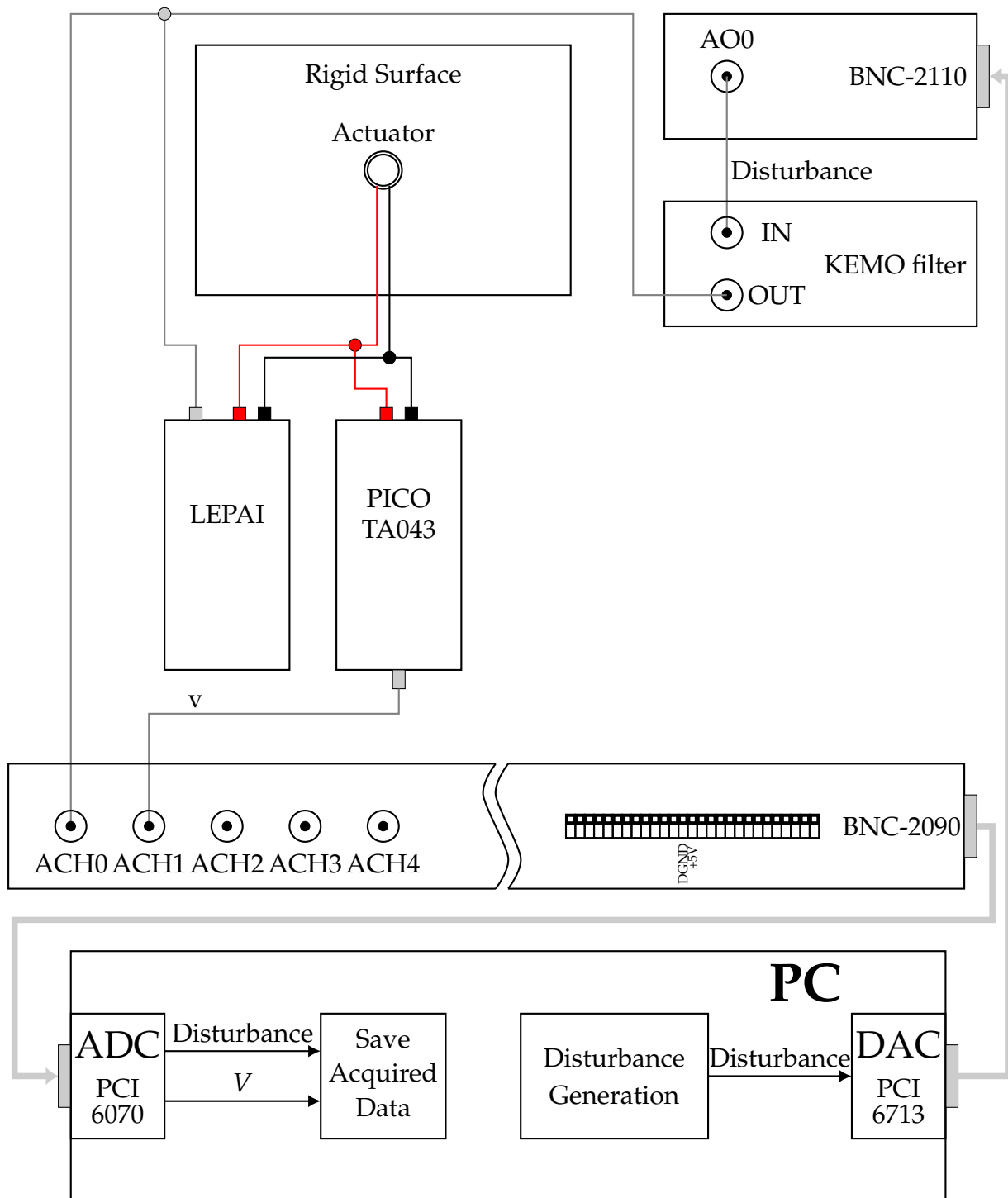


Figure 3.15: Scheme of the experimental setup adopted for the amplifiers characterization.

$$\tilde{H}(s) = g_{amp} \frac{s}{s + a} \quad (3.13)$$

It must be pointed out that while the low frequency pole of the amplifier is fixed, the gain depends on the setting of the volume knob. During the experimental characterization, the volume has been set approximately to 3/4 of the maximum, to avoid saturation. The results are reported in Table 3.5 and are in good agreement with those of Ref. [11]. The fact that the numerical model of the amplifier must be changed whenever the volume knob is moved is the main reason for which it has been chosen to actively measure the voltage. Indeed it could have been possible, knowing the disturbance that is generated by the PC, to compute the voltage after the amplifier, but for doing so, one should have been absolutely sure to do not move the volume knob.

Device	$g_{amp}[-]$	$a[\text{Hz}]$
Lepai 1	-4.5	45
Lepai 2	-4.42	45

Table 3.5: Parameters computed for the two power amplifiers.

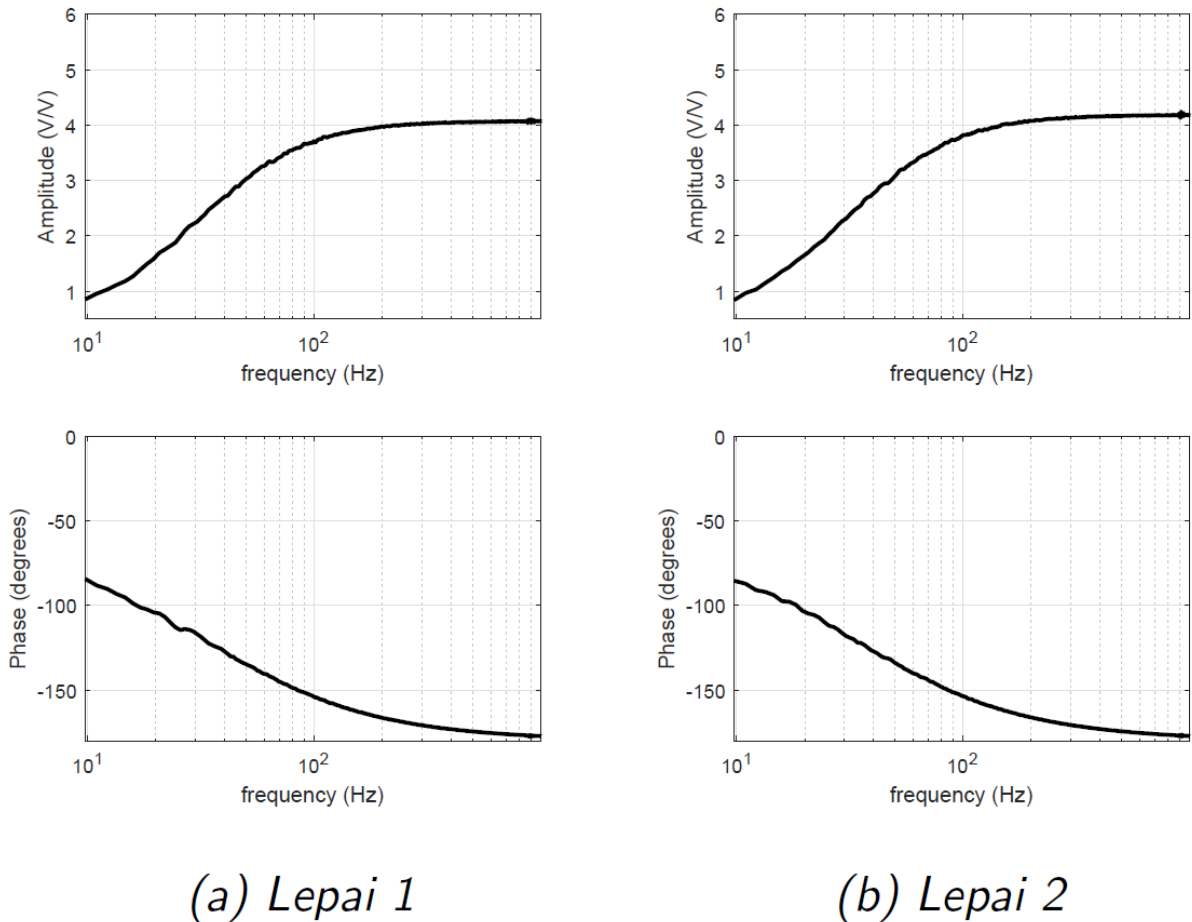


Figure 3.16: Lepai LP-2020A+.



It has to be noticed that the voltage gain is negative, meaning that the Lepai is an inverting amplifier. It can be seen also in Figure 3.16, where the phase tends to  $-180^\circ$  at high frequencies. It has to be kept in mind when using it in a control logic. Another interesting fact is that the low frequency pole is placed around  $45\text{Hz}$ , a little bit higher than the lower threshold of the human hearing.

### 3.4 Plate

The vibrating surface used in this thesis is the thin aluminum plate in [11, 32], depicted in Figure 3.17. It has thickness of  $2\text{mm}$  and a size of  $700$  by  $500\text{mm}$ . However, the presence of a steel rigid frame reduces the vibrating area to approximately  $600$  by  $400\text{mm}$ . Although the plate will be considered as clamped to the frame, it must be pointed out that this could be a rough approximation of the real bolted connection. The complete physical properties are reported in Table 3.6.

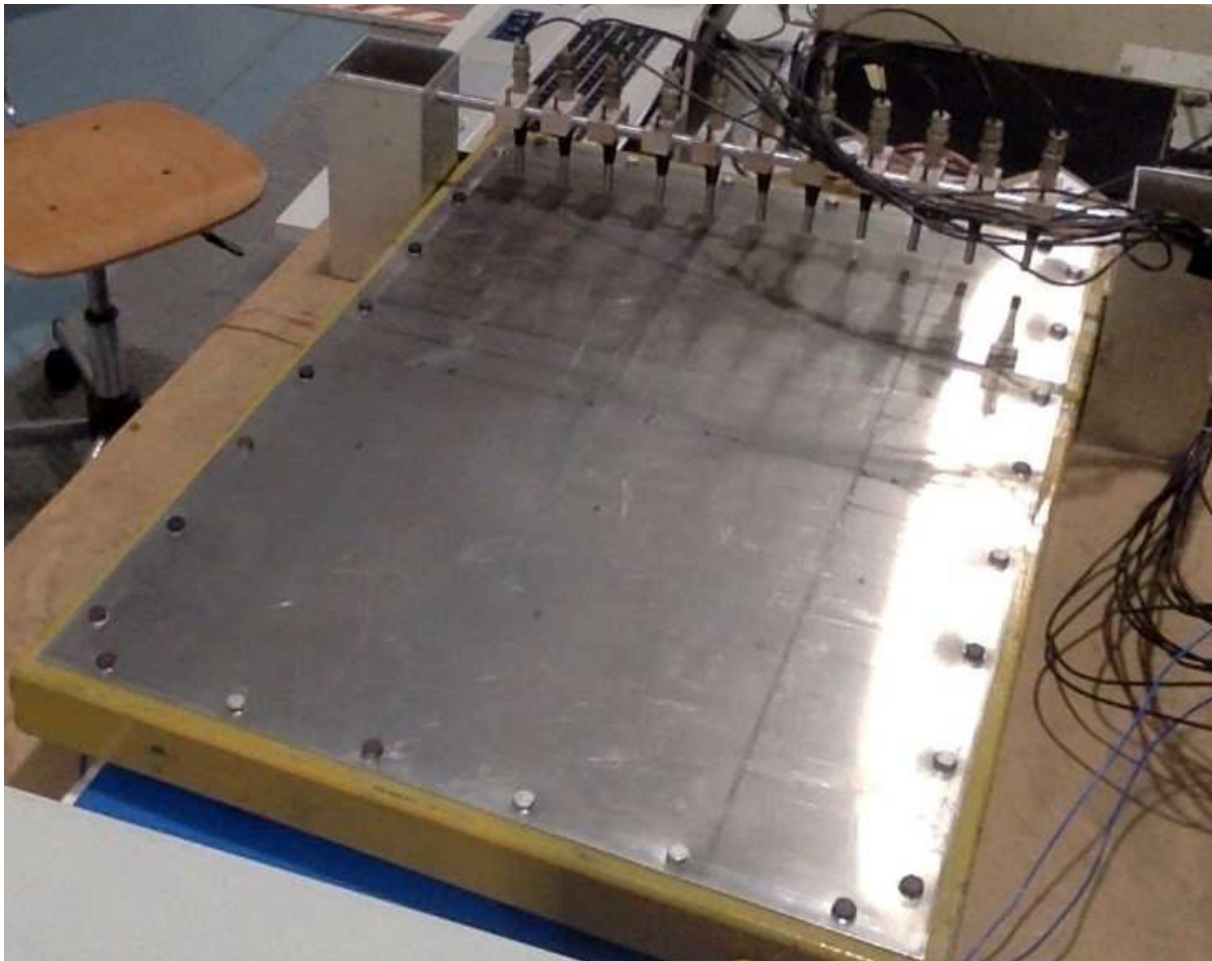


*Figure 3.17: Reference plate.*

The validation of the model has been performed in Ref. [11] comparing the results of an experimental modal analysis with the first eight modes predicted by the numerical model. The results are here reported for clarity in Figures 3.18 and 3.19.

Parameter	Value	Units
Length	600	[ <i>mm</i> ]
Width	400	[ <i>mm</i> ]
Thickness	2	[ <i>mm</i> ]
Density	2700	[ <i>kg m</i> <sup>-3</sup> ]
Young's Modulus	70	[ <i>GPa</i> ]
Poisson's Ratio	0.33	[ <i>-</i> ]

*Table 3.6: Test plate properties.*

The identification of the modes has been carried out impacting the panel with an instrumented hammer, carrying a load cell to measure the input force. The measure of the structural response has been done using an array of microphones, positioned normally to the panel, very close to the surface, such that the near-field sound pressure can be considered as an equivalent map of the transverse vibration of the plate.

The agreement of the numerical model is quite good. The shapes of the modes present some distortion, probably due to non uniform shape and boundary conditions of the plate, but still will allow to make considerations on the position of nodal lines and on the controllability of modes from a specific position. The accuracy in the estimation of the natural frequency is less satisfactory.

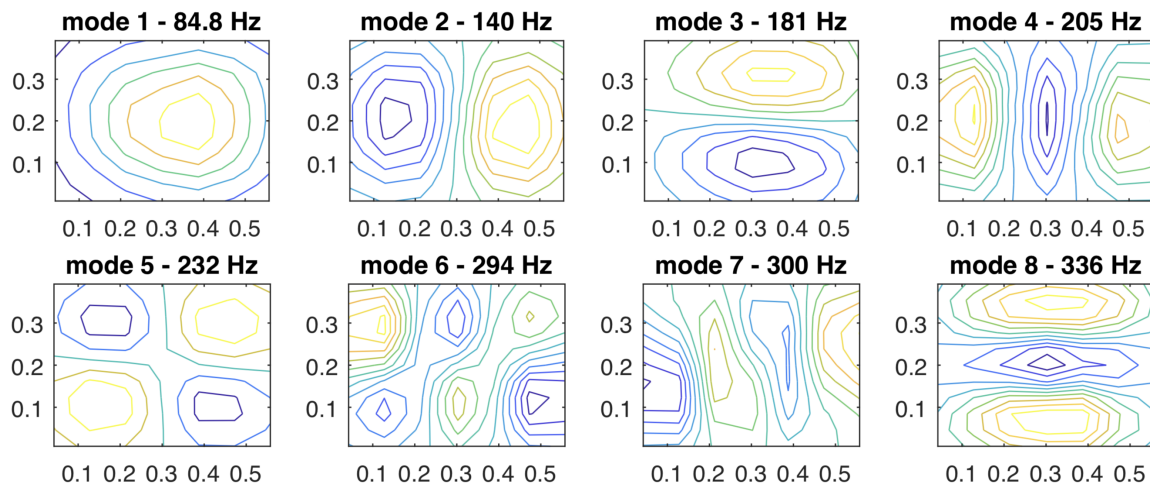


*Figure 3.18: Experimental plate mode shapes.*

As said in Chapter 2, a large use of a single degree of freedom model of the plate will be made. The parameters of the model, as obtained by Di Girolamo in Ref. [11], are reported in Table 3.7. It will be seen in the next chapters, despite the extreme simplicity of this model, that it could be useful to easily evaluate the effects of some design choices.

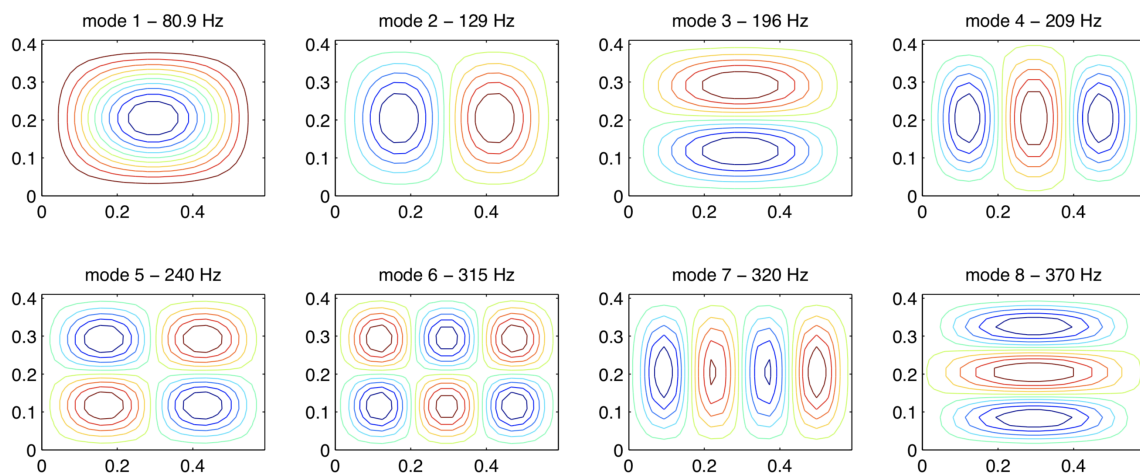


*Figure 3.19: Numerical plate mode shapes.*

$m_s$ [kg]	$c_s$ [Ns m <sup>-1</sup> ]	$k_s$ [N m <sup>-1</sup> ]
0.2171	4.4158	$5.6125 \times 10^4$

*Table 3.7: 1-DOF parameters.*



# Chapter 4

## Sensor-actuator model: Numerical Testing

In this chapter the sensor-actuator formulation derived in Chapter 2 is tested numerically. Firstly over the simple SDOF plate model, then on the complete flexible model of the structure, both in frequency and time domain. Some modification to the self-sensing actuator equation will be needed in order to achieve stability in real operating conditions.

### 4.1 Transverse plate velocity

The sensor-actuator equation for the reconstruction of the plate transverse velocity discussed in the previous chapters is reported in Eq. 4.1.

$$\dot{w}(s) = \left[ \frac{(R + sL) (s^2 m_a + s c_a + k_a) + s k_{em}^2}{s^2 m_a k_{em}} \right] i(s) - \left[ \frac{s^2 m_a + s c_a + k_a}{s^2 m_a k_{em}} \right] v(s) \quad (4.1)$$

$$= H_i(s) i(s) - H_v(s) v(s) = \dot{w}_i(s) - \dot{w}_v(s) \quad (4.2)$$

Two terms can be recognised: the first - current related -  $H_i(s)$ , and the second - voltage related -  $H_v(s)$ . It has to be noticed that after each term is multiplied by it's related electrical variable, the two resulting quantities -  $\dot{w}_i(s)$  and  $\dot{w}_v(s)$  - are subtracted. Highlighting this will prove to be of the utmost importance later. As a matter of fact the velocity reconstruction equation cannot be used as is, for reasons that will be explained later. It has to be modified, but due to the subtraction operation, the reconstruction becomes very sensitive to changes affecting only one of the two terms.

A qualitative understanding of this behaviour can be achieved by looking at Figure 4.1, where  $\dot{w}_i(s)$  and  $\dot{w}_v(s)$  are depicted, as obtained in laboratory (Chapter 5). It can be noticed that the two terms -  $\dot{w}_i(s)$  and  $\dot{w}_v(s)$  - differs only by a small fraction of their value. Since the plate velocity  $\dot{w}$  is in fact the difference between such two terms, it's

easy to understand that if one, for any reason, is modified, the reconstructed velocity would be heavily affected.

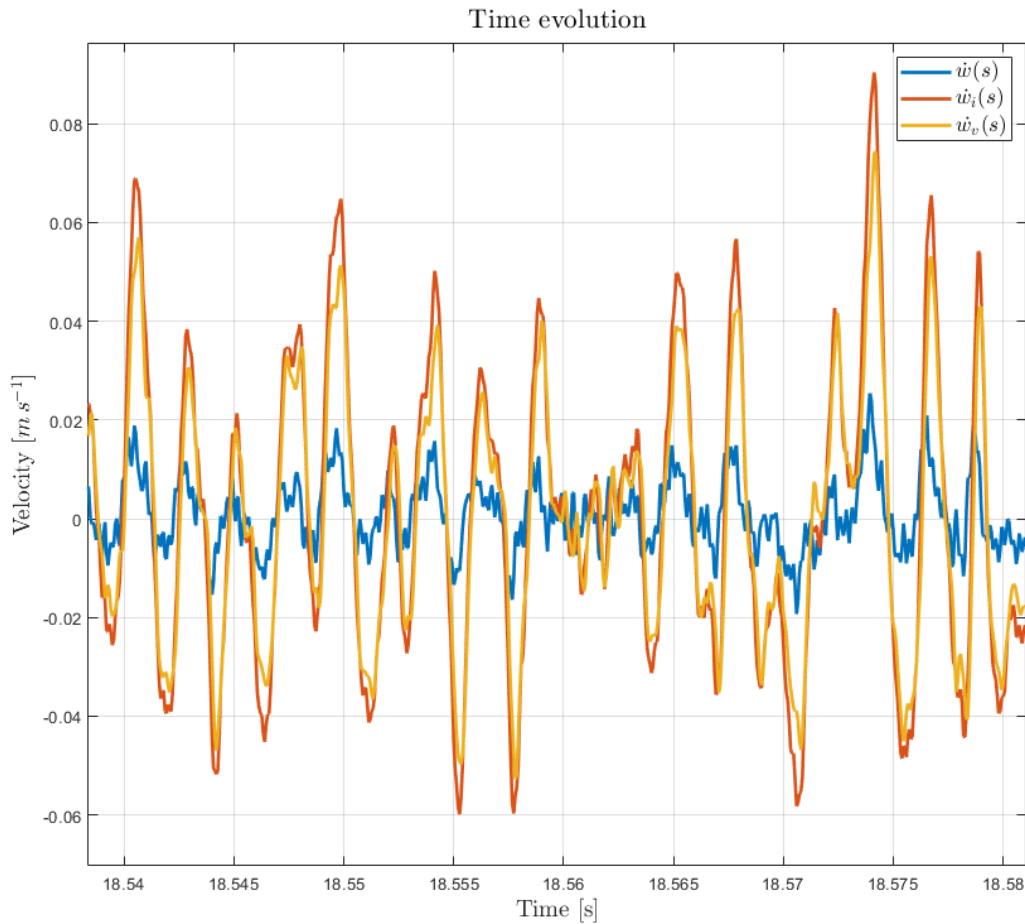


*Figure 4.1: Comparison of the  $\dot{w}_i(s)$  and  $\dot{w}_v(s)$  terms.*

As anticipated the aim of this chapter is to modify Eq. 4.1 in order to obtain a formulation that can be implemented in real-time laboratory testing. In fact, implementing Eq. 4.1 would give good results only in numerical simulations, while the performances in laboratory would be completely unsatisfying. This asymmetry between numerical and experimental analysis is due to different phenomena that affect only the experimental setup, that have to be included in the numerical simulation if significant results are to be drawn. The main problems and uncertainties taken into account in the following are:

- Offset in the current and voltage measures.
- High frequency noise in the measurements.
- Low frequency components due to unmodelled dynamics.
- Uncertainties on the actuator parameters computed in Chapter 3.

As a first step, the velocity reconstruction equation, so as derived from the dynamics system, is analyzed and the response to the uncertainties is explored.

### 4.1.1 High frequency behaviour

The first issue arises from the  $H_i(s)$  term. The transfer function has a numerator of order 3, while the denominator is of order 2, therefore is improper. This means that the amplification introduced by the transfer function goes to infinite as the frequency goes to infinite, causing an unbounded and detrimental amplification of the high frequency noise. Performing only a numerical simulation this phenomenon may go unnoticed at first, because in the ideal case it is exactly compensated by the actuator dynamics present in the current signal by which  $H_i(s)$  has to be multiplied. This is true only in ideal conditions though: if, for example, an uncertainty is introduced in the actuator parameters, it translates in an incorrect compensation that leads to huge errors in the reconstruction of the velocity.

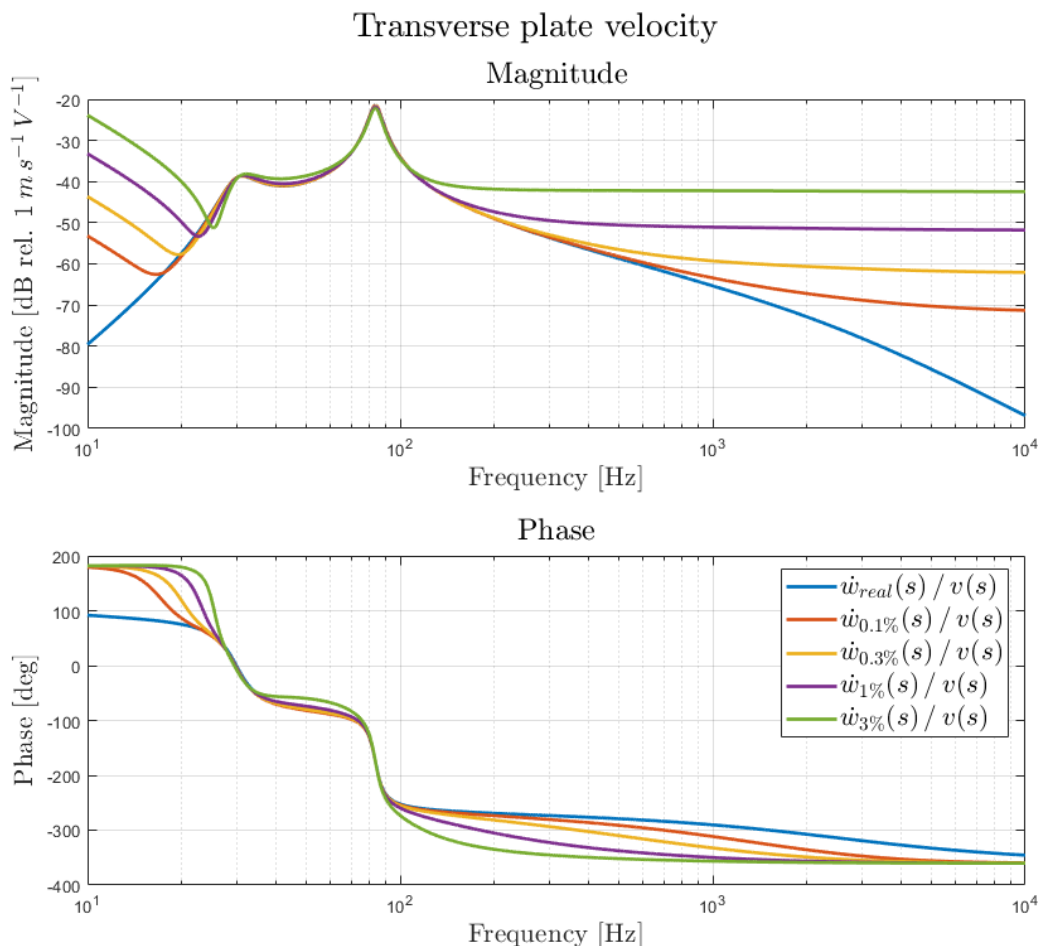


**Figure 4.2:** Plate velocity reconstruction with different errors in the actuator parameters.

Figure 4.2 shows that when small errors in the determination of the actuator's param-

eters performed in Chapter 3 are made, any high frequency component is amplified in the same way, while instead a decreasing magnitude is required. Possible solutions are to add a pole to the denominator or to drop a zero from the numerator.

### Static residualization of the electrical dynamics

Since a way to reduce the order of the numerator is sought, the static residualization of the electrical dynamics could appear to be a good solution. Indeed - as shown in Chapter 2 and reported in Eq. 4.3 for the sake of clarity - the term  $H_i(s)$  becomes strictly proper if the statically residualized case is considered, while  $H_v(s)$  is not affected.

$$\dot{w}(s) = \left[ \frac{R \left( s^2 m_a + s c_a + k_a \right) + s k_{em}^2}{s^2 m_a k_{em}} \right] i(s) - \left[ \frac{s^2 m_a + s c_a + k_a}{s^2 m_a k_{em}} \right] v(s) \quad (4.3)$$

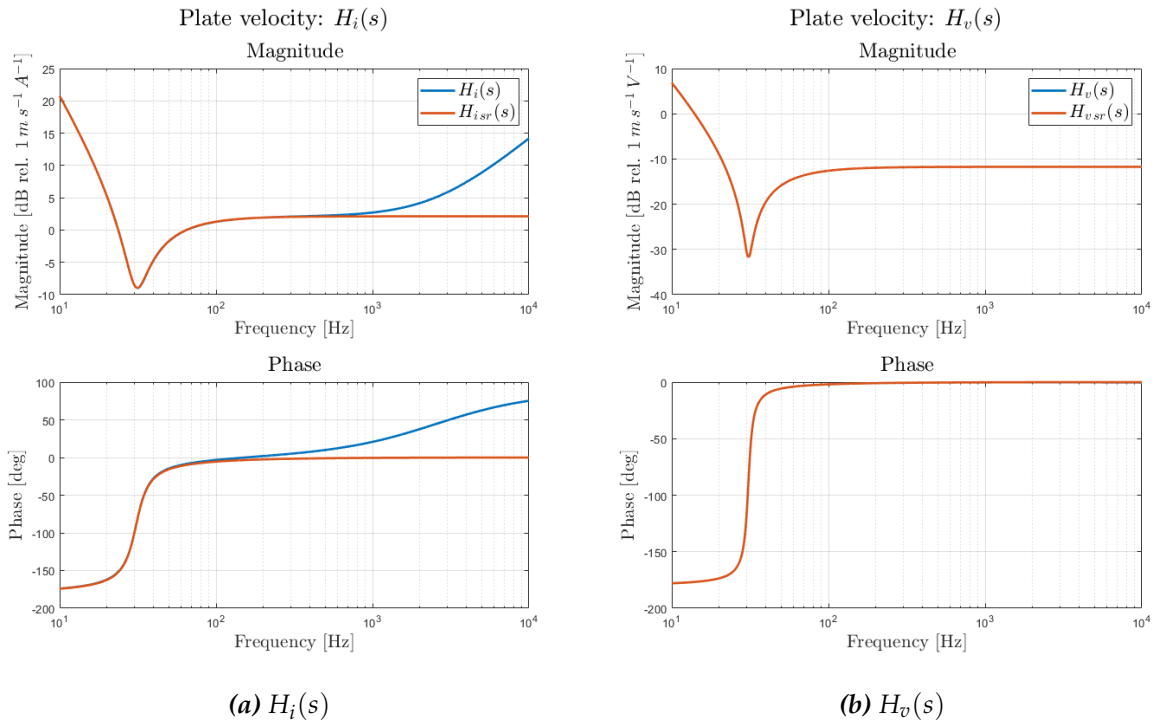


**Figure 4.3:** Bode plot of the two transfer functions for the transverse plate velocity reconstruction, both in the complete and statically residualized formulation.

In Figure 4.3 are depicted both the complete and the statically residualized electrical case for both the transfer functions  $H_i(s)$  and  $H_v(s)$ . It can be noticed that removing the electrical zero, the current related term approaches an horizontal asymptote for high frequencies, while the voltage related term is not modified. As has been said in



the previous chapters, the goodness of the statically residualized model has to be assessed for the specific application under analysis. Assuming that the frequency range of interest of this work is upper bounded at about  $1\text{kHz}$ , it could seem that the static residualization should not alter significantly the performances in the range of interest, being  $H_i(s) \approx H_{i\text{res}}(s)$  below  $1\text{kHz}$ . Unfortunately this is not the case, and what before has been only anticipated qualitatively - that any modification introduced on only one of  $H_i(s)$  or  $H_v(s)$  could heavily compromise the velocity reconstruction - it's demonstrated in the following.

Eq. 4.2 can be rewritten as:

$$\begin{aligned}\dot{w}(s) &= H_i(s)i(s) - H_v(s)v(s) \\ &= \left( H_i(s) \frac{i(s)}{v(s)} - H_v(s) \right) v(s) \\ &= (H_i(s)Y(s) - H_v(s)) v(s)\end{aligned}$$

Where has been introduced the electrical admittance  $Y(s)$ , defined as the inverse of the electrical impedance and depicted in Figure 4.4.

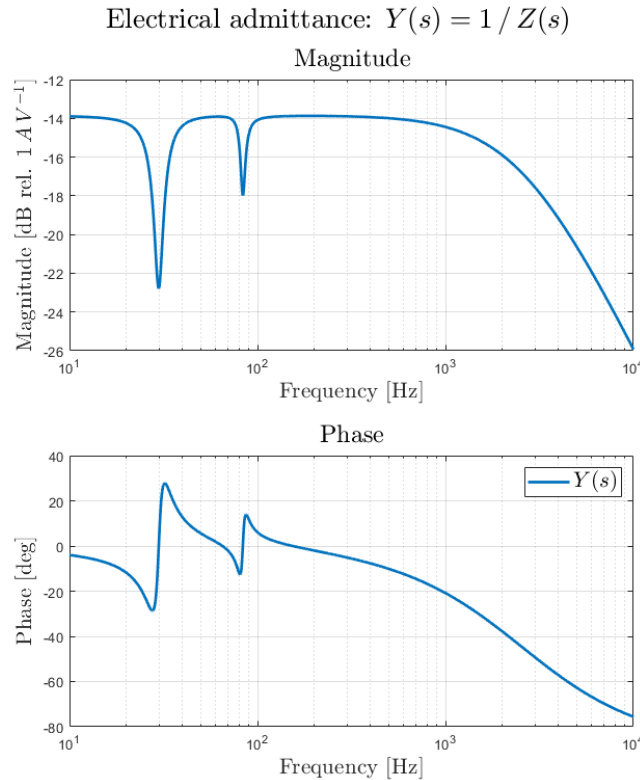


**Figure 4.4:** Electrical admittance simulated for the simple SDOF plate coupled with the lumped parameters model of the inertial actuator.

The plate model employed in these simulations is the simple single-degree-of-freedom,

it can be noted from the presence of only two resonance frequencies: the first around 30Hz due to the actuator, and the second slightly above 80Hz representing the first mode of the plate. The reduction in the magnitude at high frequency, instead, is due to the electrical dynamics of the actuator, *i.e.* to the action of the inductance. Keep also in mind that - although the velocity reconstruction equation can be statically residualized - the inductance contribute will always be present in the real dynamics of the actuator, therefore the electrical admittance shall remains the one depicted in Figure 4.4, no matter the approximation adopted in the reconstruction of the velocity. Even if the last clarification could seems obvious, it becomes of the utmost importance in Figure 4.5, where the two transfer functions  $H_i(s)Y(s)$  and  $H_v(s)$  are plotted for the complete and residualized case.

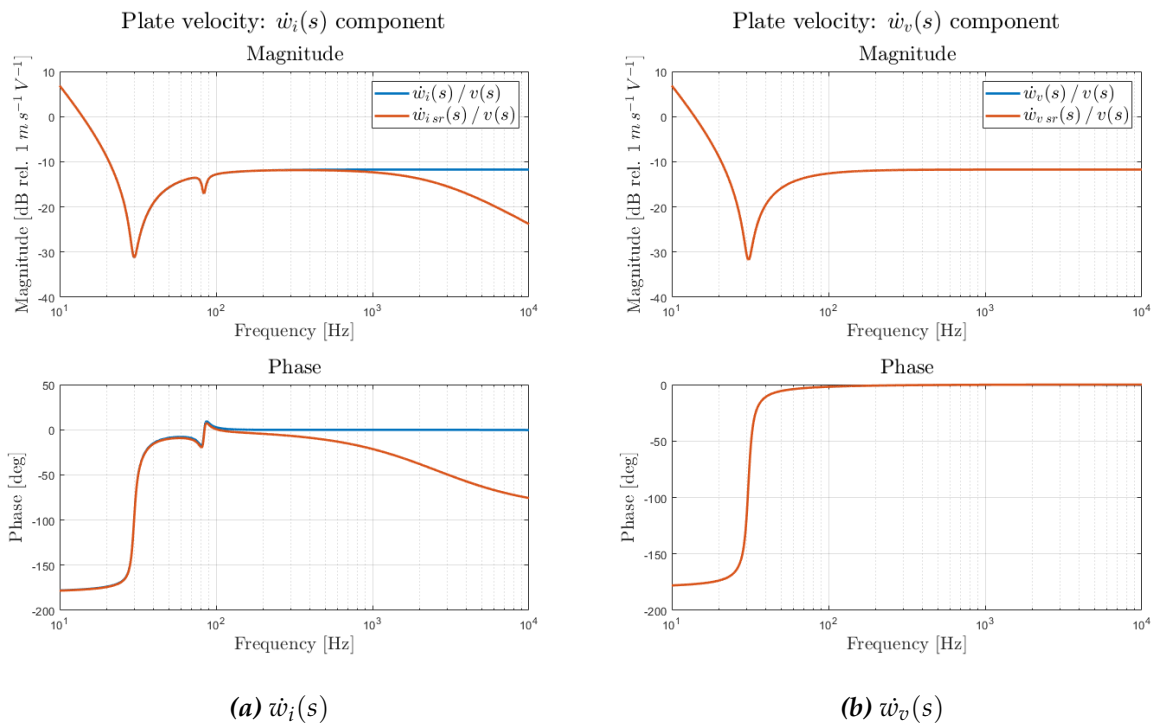


**Figure 4.5:** Frequency response to the input voltage of the two terms for the transverse plate velocity reconstruction, both in the complete and statically residualized formulation.

As expected, the difference at the high frequencies between  $H_i(s)$  and  $H_{i\text{res}}(s)$  is still present also after the multiplication by the electrical admittance. Note that in the complete - not residualized - case,  $H_i(s)Y(s)$  has an horizontal asymptote at high frequency, meaning that the electrical zero of  $H_i(s)$  is exactly compensated by a pole in the admittance - reason for which, despite  $H_i(s)$  not being proper, the velocity reconstruction formula appears to be stable, at least in numerical ideal conditions - while in the statically residualized case the electrical zero is dropped, therefore it can't compensate the pole in the admittance, resulting in a pole in the  $H_{i\text{res}}(s)Y(s)$  term. If, by a careless design, the static residualization of the electrical dynamics were implemented not only in the velocity reconstruction formula, but also in the dynamic model of the actuator, the electrical admittance would loose it's high frequency pole too, causing the term

$H_{i\text{res}}(s)Y_{\text{res}}(s)$  to be equal to the unresidualized one ( $H_i(s)Y(s)$ ). This could seem a great result, while instead is just a poor representation of the reality, because the behaviour of the real prototype actuator always shows the inductance contribute. Indeed this error would lead to believe that the residualized model could be a valid solution, while in practice it gives wrong result.

In Figure 4.6 the reconstructed velocity is compared with the real velocity of the plate. When the complete formulation of Eq. 4.1 is used, the results are perfectly superimposed to the real velocity, while if the residualized equation is used, the reconstruction completely fails to catch the real behaviour far from the two resonance peaks. The reason for that can be found by looking at Figure 4.5. The velocity is obtained subtracting 4.5b from 4.5a. When the complete case is considered, both figures have a flat high frequency behaviour, while in the residualized case the current term has a decreasing magnitude, that translates in an increasing difference between the two terms, as can be seen in Figure 4.6.

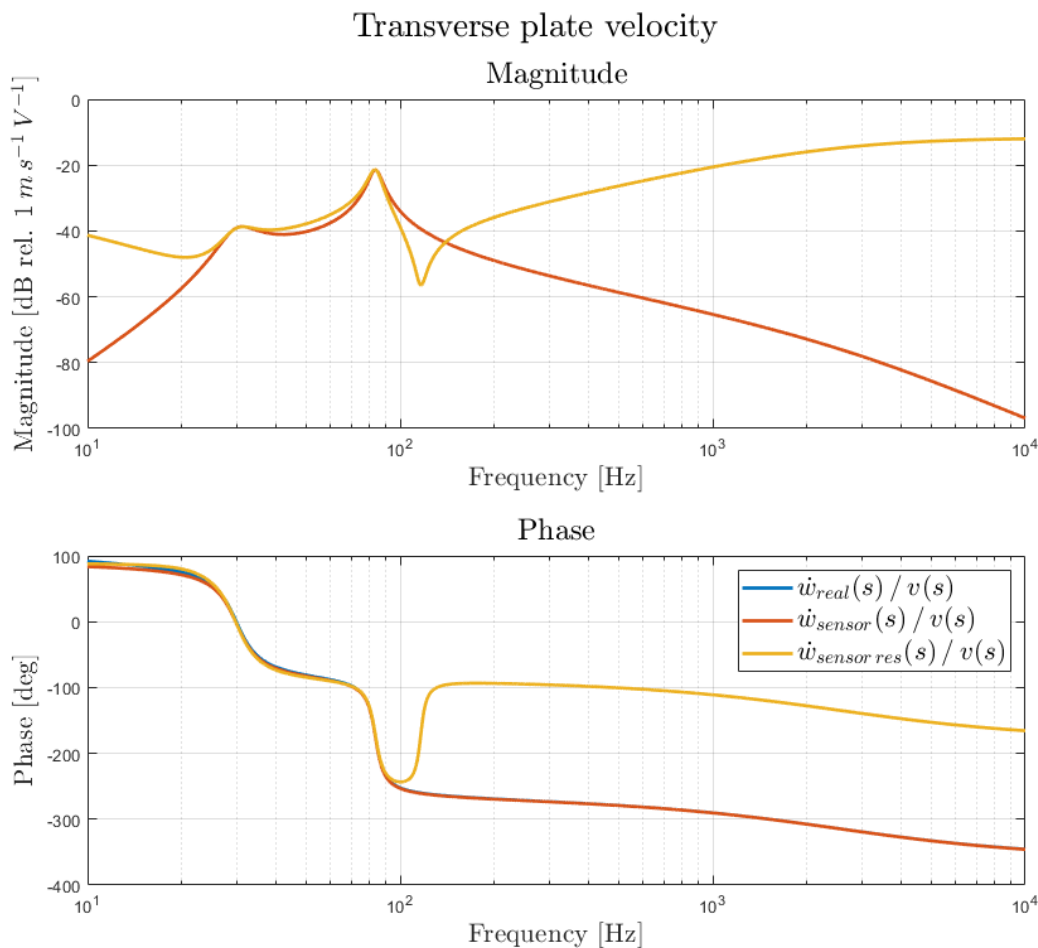


**Figure 4.6:** Reconstructed velocity frequency response, obtained both with the complete and statically residualized formulation, compared with the real velocity of the plate.

The result just obtained could seem counterintuitive: it was sought a way to solve the

problem of  $H_i(s)$  being improper, but it results that the velocity is better reconstructed using the improper  $H_i(s)$  than using the proper but statically residualized  $H_{i\text{res}}(s)$ . Indeed  $H_{i\text{res}}(s)$  seemed nearly superimposed to  $H_i(s)$  at frequencies below  $1\text{kHz}$ , but that is only thanks to implicit logarithmic scale of decibels in Figure 4.3. If the error is evaluated as the ratio of  $H_i(s)$  to  $H_{i\text{res}}(s)$  in a linear scale, more significant results are obtained, as reported in Table 4.1. Having assumed the frequency range of interest of this thesis to reach  $1\text{kHz}$ , and remembering that the transverse velocity of the plate is obtained subtracting two terms that only slightly differ from each other (Figure 4.1), it's evident that a 40% error is too much. Therefore another mean to obtain a proper transfer function has to be sought, with a particular attention to modifying in the same way both  $H_i(s)$  and  $H_v(s)$ .

Frequency [Hz]	Error [%]	Error [dB]
10	0.4	0.03
30	1.2	0.10
60	2.4	0.21
100	4.0	0.34
300	12.0	0.98
600	24.0	1.86
1000	40.0	2.92
3000	119.8	6.84

**Table 4.1:** Approximation error of  $H_{i\text{res}}(s)$  with respect to  $H_i(s)$ .

### High frequency pole

Another way to make  $H_i(s)$  proper is to add a pole. In principle there's no much difference between adding a pole and removing a zero, as done in the statically residualized case just presented. The difference lays in the fact that the zero to be removed is at a fixed frequency, while the pole to be added can be put at any arbitrarily high frequency  $\omega_h$  in order to keep the required distance from the frequency range of interest. Moreover a pole can be added to both  $H_i(s)$  and  $H_v(s)$  mitigating the effect described above. A possible representation of the new expression for the reconstruction of the transverse plate velocity, with the addition of an high frequency pole is reported in Eq. 4.4.

$$\dot{w}(s) = \left[ \frac{(R + sL) (s^2 m_a + s c_a + k_a) + s k_{em}^2}{s^2 m_a k_{em} \left(1 + \frac{s}{\omega_h}\right)} \right] i(s) - \left[ \frac{s^2 m_a + s c_a + k_a}{s^2 m_a k_{em} \left(1 + \frac{s}{\omega_h}\right)} \right] v(s) \quad (4.4)$$

Where to place the new pole is not trivial. Of course it should be placed at a frequency high enough to not have influence in the frequency range of interest, but at the same

time it is reasonable to keep it as low as possible in order to better reject high frequency noise. The latter requirement is not easily analysable in the frequency domain, and will be shortly addressed later in a time simulation. However, it can be anticipated that it will not be found to be much constraining.

Note that if it is imposed

$$\omega_h = \frac{R \left( s^2 m_a + s c_a + k_a \right) + s k_{em}^2}{L \left( s^2 m_a + s c_a + k_a \right)}$$

it can be obtained again the static residualization of the  $H_i(s)$  term

$$\begin{aligned} H_i(s) &= \frac{(R + sL) \left( s^2 m_a + s c_a + k_a \right) + s k_{em}^2}{s^2 m_a k_{em} \left( 1 + \frac{s}{\omega_h} \right)} \\ &= \frac{(R + sL) \left( s^2 m_a + s c_a + k_a \right) + s k_{em}^2}{s^2 m_a k_{em} \left( 1 + \frac{s}{\frac{R \left( s^2 m_a + s c_a + k_a \right) + s k_{em}^2}{L \left( s^2 m_a + s c_a + k_a \right)}} \right)} \\ &= \frac{(R + sL) \left( s^2 m_a + s c_a + k_a \right) + s k_{em}^2}{s^2 m_a k_{em} \left( 1 + \frac{Ls \left( s^2 m_a + s c_a + k_a \right)}{R \left( s^2 m_a + s c_a + k_a \right) + s k_{em}^2} \right)} \frac{R \left( s^2 m_a + s c_a + k_a \right) + s k_{em}^2}{R \left( s^2 m_a + s c_a + k_a \right) + s k_{em}^2} \\ &= \frac{\left[ (R + sL) \left( s^2 m_a + s c_a + k_a \right) + s k_{em}^2 \right] \left[ R \left( s^2 m_a + s c_a + k_a \right) + s k_{em}^2 \right]}{s^2 m_a k_{em} \left[ R \left( s^2 m_a + s c_a + k_a \right) + s k_{em}^2 + Ls \left( s^2 m_a + s c_a + k_a \right) \right]} \\ &= \frac{\left[ (R + sL) \left( s^2 m_a + s c_a + k_a \right) + s k_{em}^2 \right] \left[ R \left( s^2 m_a + s c_a + k_a \right) + s k_{em}^2 \right]}{s^2 m_a k_{em} \left[ (R + sL) \left( s^2 m_a + s c_a + k_a \right) + s k_{em}^2 \right]} \\ &= \frac{R \left( s^2 m_a + s c_a + k_a \right) + s k_{em}^2}{s^2 m_a k_{em}} = H_{i \text{ res}}(s) \end{aligned}$$

with an additional compensation of  $H_v(s)$  so as not to run into the problem described above.

Note, in Figure 4.7, that this peculiar case does not offer better performances than the others, therefore there's no reason to implement it.

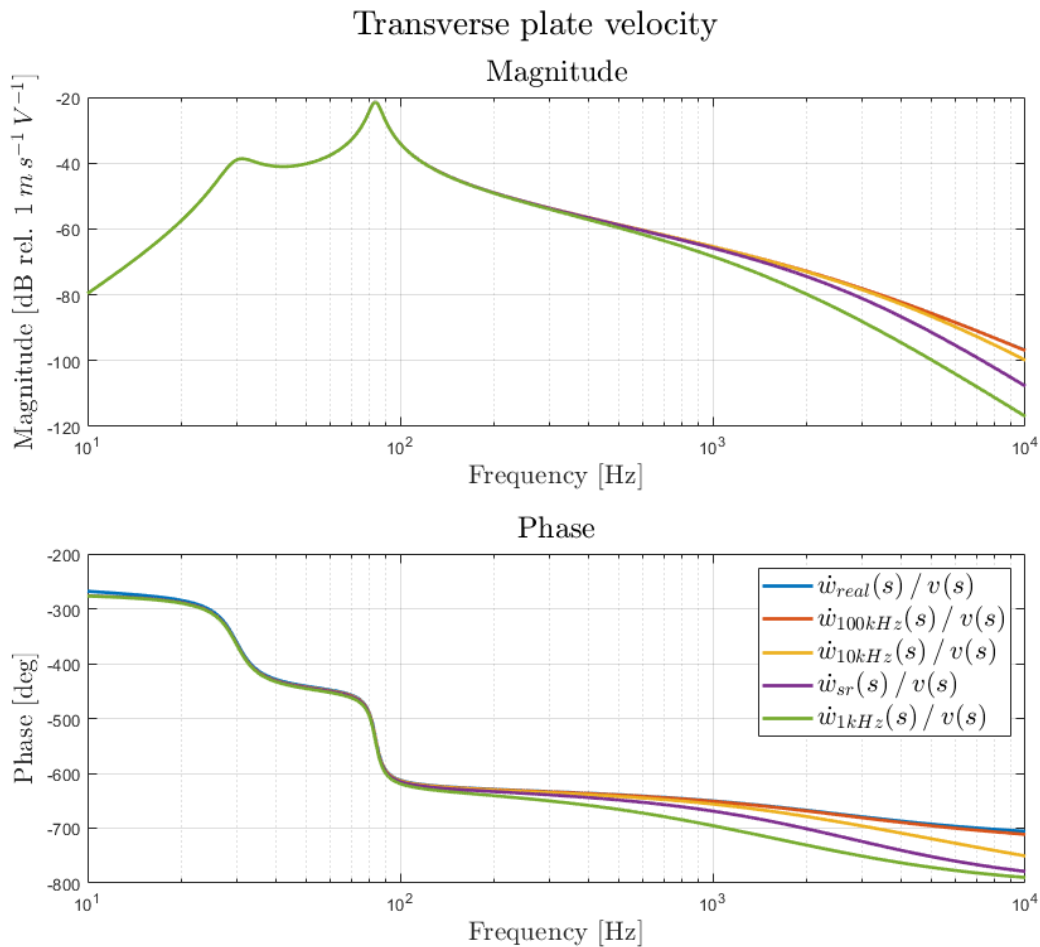


**Figure 4.7:** Reconstructed velocity frequency response, obtained with different high frequency poles, compared with the real velocity of the plate.

Comparing Figure 4.7 with Figure 4.6 it is evident that modifying both  $H_i(s)$  and  $H_v(s)$  dramatically improves the performance of the reconstruction of the velocity. With any  $\omega_h$  higher than about  $2\text{kHz}$  a proper transfer function is obtained with no detrimental effects in the frequency range of interest.

It has been demonstrated so far that the pole addition does not have detrimental effects on the reconstruction of the transverse plate velocity in ideal numerical conditions. However, it should be checked if its behaviour remains satisfactory even when an error in the actuator's parameters is introduced. Figure 4.8 depicts a comparison when the error is fixed at 1%. As anticipated, the lower the value of  $\omega_h$ , the better the reconstruction of the velocity in case of error in the parameters. As said before, the frequency analysis is not the best tool to understand how low the new pole has to be placed to reject the high frequency noise. Indeed it could appear from Figure 4.8 that also  $1\text{kHz}$  is too high to obtain a perfect reconstruction of the velocity. Although

the reason is not much straightforward, this is not true. The desired effect introducing the high frequency pole is not to achieve a perfect superposition with the true velocity - superposition that would be in any case impossible to achieve in laboratory due to noise and resolution problems - but to reproduce the decaying in the magnitude at high frequency of the real velocity plot, mainly for noise rejection purposes. As proof of this, it will be seen later that  $\omega_h = 2kHz$  is enough to achieve a good reconstruction of the velocity in time domain. Before showing this, the response at low frequency has to be analyzed.

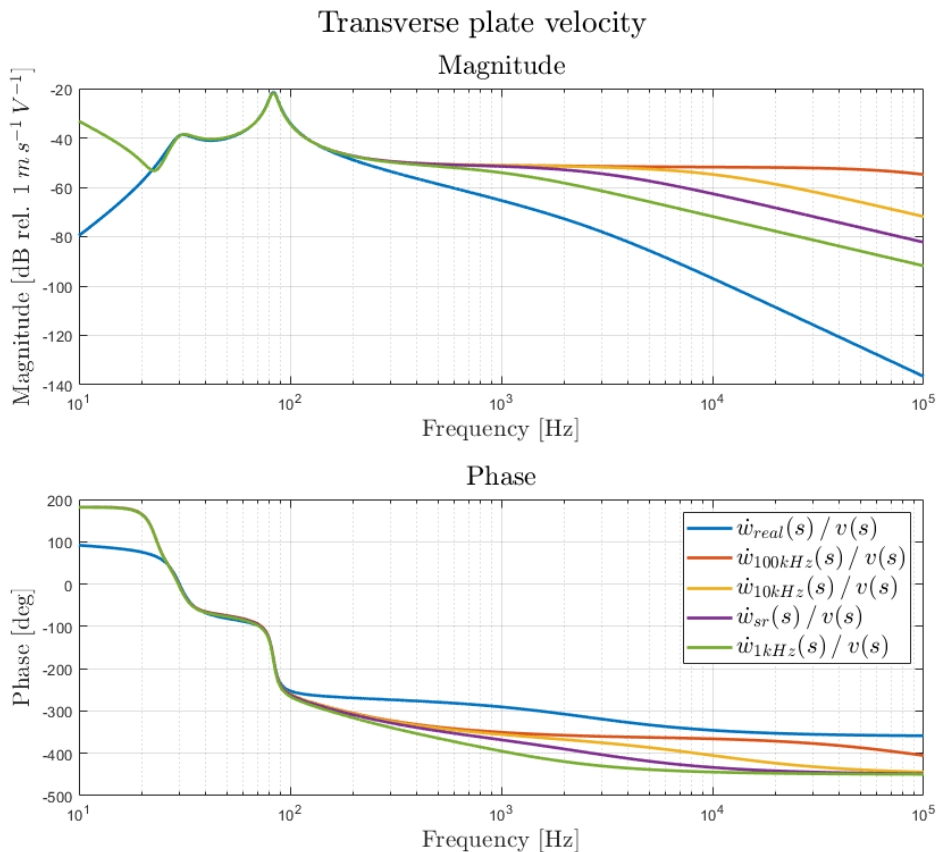


**Figure 4.8:** Reconstructed velocity frequency response, obtained with different high frequency poles, compared with the real velocity of the plate, when a 1% error in the actuator's parameters is introduced.

#### 4.1.2 Low frequency behaviour

Up to now the focus has been on the high frequency behaviour. It has to be noticed though that, when the uncertainty about the actuator's parameters is introduced, also frequencies below 20Hz are affected. It is visible both in Figure 4.6 and 4.8.

The reason lies in the expression for the reconstruction of the plate velocity, Eq. 4.1. Both terms have two poles in the origin, making the two transfer functions unstable. As before, if the ideal case is analyzed, the pure integration action at low frequency is exactly cancelled subtracting the two terms in Figure 4.5. This is no longer true in a real

application, due to the inaccuracy of the model. Moreover, as shown in Chapter 5, the experimental setup is affected by some offset in the acquisition of current and voltage, thus introducing low frequency components that requires the electrical quantities to be filtered before being used for the reconstruction of the velocity. To avoid any problem, the two poles in the origin can be substituted with two generic complex conjugate poles with negative real part, as in Eq. 4.5.

$$\dot{w}(s) = \begin{bmatrix} \frac{(R + sL) (s^2 m_a + s c_a + k_a) + s k_{em}^2}{m_a k_{em} (s^2 + 2\xi_l \omega_l s + \omega_l^2) \left(1 + \frac{s}{\omega_h}\right)} i(s) \\ - \frac{s^2 m_a + s c_a + k_a}{m_a k_{em} (s^2 + 2\xi_l \omega_l s + \omega_l^2) \left(1 + \frac{s}{\omega_h}\right)} v(s) \end{bmatrix} \quad (4.5)$$

There are two parameters to be selected: the damping coefficient and the cutting frequency. Figure 4.9 shows a comparison of  $H_i(s)$  and  $H_v(s)$  with different cutting frequencies and a damping coefficient  $\xi_l = 1$ .

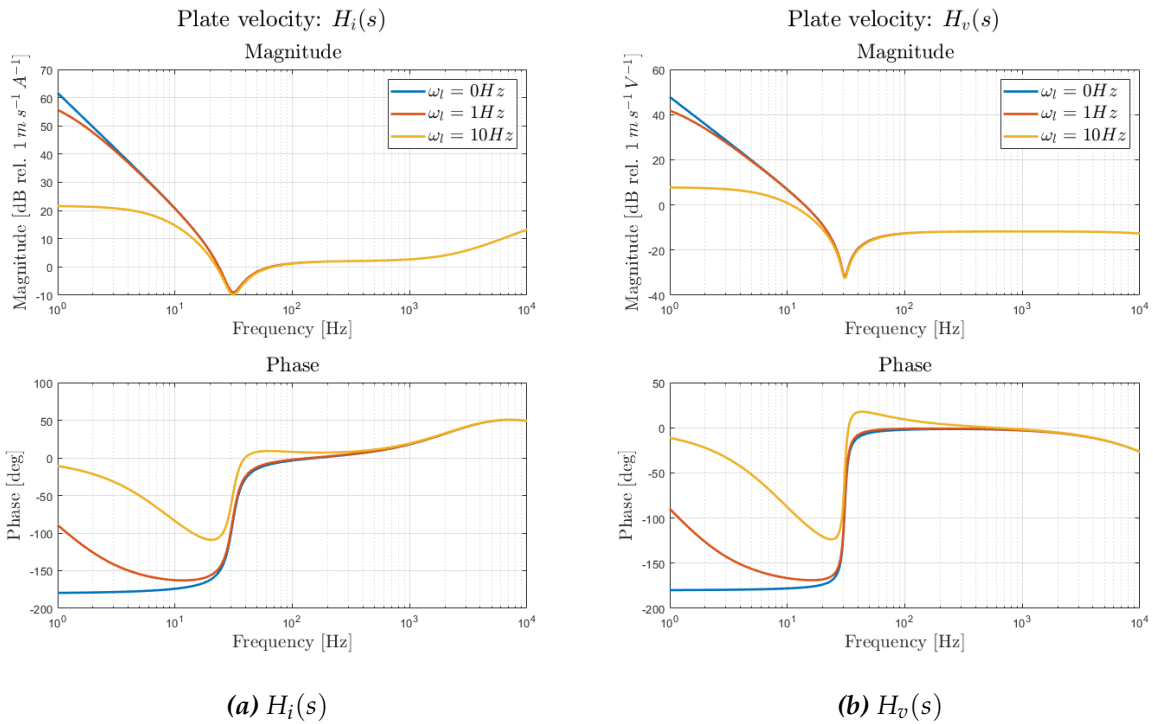


**Figure 4.9:** Bode plot of the two transfer functions for the transverse plate velocity reconstruction, for different frequencies of the low frequency poles.



Since the aim is to obtain stable transfer functions, the cutting frequency could be taken arbitrarily low. However, as explained in the next chapter, it could be useful to set the poles to the highest possible frequency in order to reduce the amplification of some undesired low frequency dynamics, that can arise filtering the electrical signals. Having in mind that the the aim of this thesis is to suppress acoustic vibrations, the frequency range of interest is limited at 20Hz, therefore placing the low frequency poles at 10Hz can be considered an acceptable compromise. In Figure 4.10 it can be seen that this only induces minor modification of the reconstructed velocity in the frequency range of interest, when the simulation is performed in ideal conditions.

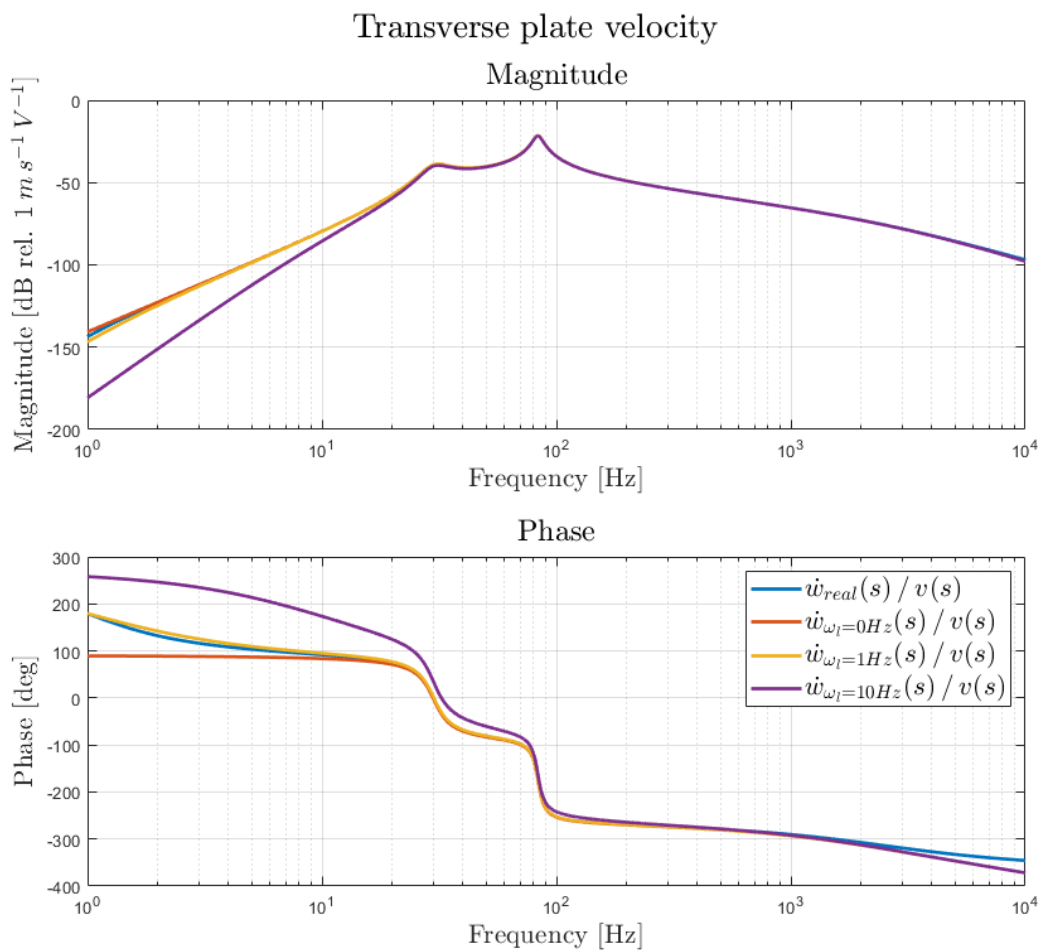


**Figure 4.10:** Reconstructed velocity frequency response, obtained with different low frequency poles, compared with the real velocity of the plate.

If 1% uncertainty is introduced on the actuator's parameters the results in Figure 4.11 are obtained. As for the high frequency behaviour is not sought a perfect superposition with the real velocity outside the range of interest, it is enough to obtain an horizontal asymptote for low frequencies. The higher the frequency at which the two poles are placed, the lower the magnitude of the asymptote, the lower the amplification of an undesired low frequency noise.

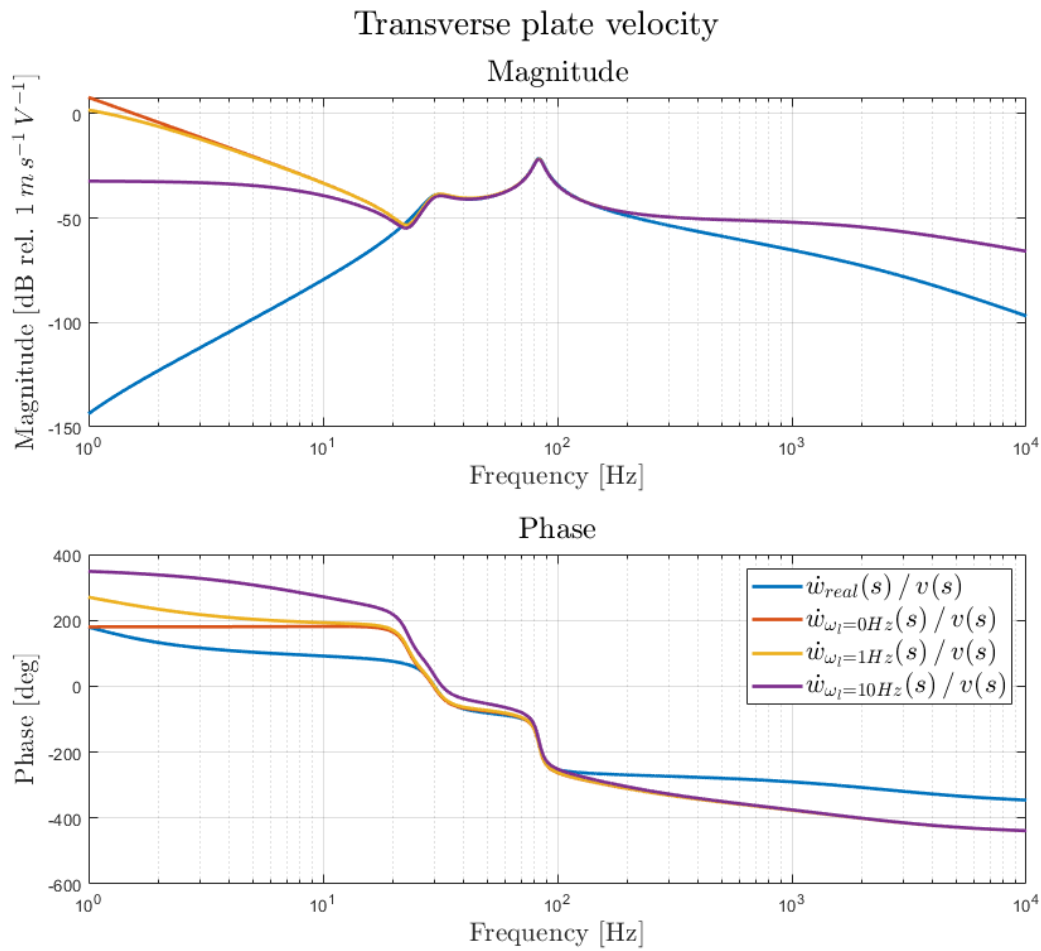


**Figure 4.11:** Reconstructed velocity frequency response, obtained with different low frequency poles, compared with the real velocity of the plate, when a 1% error in the actuator's parameters is introduced.

### 4.1.3 Discrete realization

The last numerical simulations presented in this chapter want to reproduce the testing conditions of the prototype plate. Up to now all simulations has been performed in continuous time, but since the real-time control shall be realized in discrete time, a discrete realization of the transverse plate velocity expression has to be derived. To bring the continuous Eq. 4.6 in a discrete time formulation, the Tustin's method can be applied, firstly on the current related transfer function  $H_i(s)$ , then on the voltage related  $H_v(s)$ .

$$\begin{aligned}
\dot{w}(s) &= \left[ \frac{(R + sL) (s^2 m_a + s c_a + k_a) + s k_{em}^2}{m_a k_{em} (s^2 + 2\zeta_l \omega_l s + \omega_l^2) \left(1 + \frac{s}{\omega_h}\right)} \right] i(s) \\
&\quad - \left[ \frac{s^2 m_a + s c_a + k_a}{m_a k_{em} (s^2 + 2\zeta_l \omega_l s + \omega_l^2) \left(1 + \frac{s}{\omega_h}\right)} \right] v(s) \\
&= H_i(s) i(s) - H_v(s) v(s) \\
&= \dot{w}_s(s) - \dot{w}_v(s)
\end{aligned} \tag{4.6}$$

### Current term

Substituting  $s = \frac{2}{Dt} \frac{z-1}{z+1}$

$$\begin{aligned}
H_i(s) &= \frac{\dot{w}_i(s)}{i(s)} = \frac{(R + sL) (s^2 m_a + s c_a + k_a) + s k_{em}^2}{m_a k_{em} (s^2 + 2\zeta_l \omega_l s + \omega_l^2) \left(1 + \frac{s}{\omega_h}\right)} \\
&= \frac{1}{m_a k_{em}} \frac{Rk_a + \frac{2Rc_a}{Dt} \frac{z-1}{z+1} + \frac{4Rm_a}{Dt^2} \frac{(z-1)^2}{(z+1)^2} + \frac{2Lk_a}{Dt} \frac{z-1}{z+1} + \frac{4Lc_a}{Dt^2} \frac{(z-1)^2}{(z+1)^2} + \frac{8Lm_a}{Dt^3} \frac{(z-1)^3}{(z+1)^3} + \frac{2k_{em}^2}{Dt} \frac{z-1}{z+1}}{\frac{8}{\omega_h Dt^3} \frac{(z-1)^3}{(z+1)^3} + \frac{4}{Dt^2} \frac{(z-1)^2}{(z+1)^2} + \frac{8\zeta_l \omega_l}{\omega_h Dt^2} \frac{(z-1)^2}{(z+1)^2} + \frac{4\zeta_l \omega_l}{\omega_h Dt} \frac{z-1}{z+1} + \frac{2\omega_l^2}{\omega_h Dt} \frac{z-1}{z+1} + \omega_l^2} \\
&= \frac{1}{m_a k_{em}} \frac{Lm_a(z-1)^3 + 4(Rm_a + Lc_a)Dt(z-1)^2(z+1) + 2(Rc_a + Lk_a + k_{em}^2)Dt^2(z-1)(z+1)^2 + Rk_a Dt^3(z+1)^3}{\frac{8}{\omega_h} (z-1)^3 + 4Dt \left(1 + \frac{2\zeta_l \omega_l}{\omega_h}\right) (z-1)^2(z+1) + 2Dt^2 \left(2\zeta_l \omega_l + \frac{\omega_l^2}{\omega_h}\right) (z-1)(z+1)^2 + \omega_l^2 Dt^3 (z+1)^3}
\end{aligned}$$

$$\begin{aligned}
& \frac{8Lm_a(z^3 - 3z^2 + 3z - 1) + 4(Rm_a + Lc_a)Dt(z^3 - z^2 - z + 1)}{1 + 2(Rc_a + Lk_a + k_{em}^2)Dt^2(z^3 + z^2 - z - 1) + Rk_aDt^3(z^3 + 3z^2 + 3z + 1)} \\
= & \frac{1}{m_ak_{em}} \frac{8}{\omega_h} (z^3 - 3z^2 + 3z - 1) + 4Dt \left( 1 + \frac{2\xi_l\omega_l}{\omega_h} \right) (z^3 - z^2 - z + 1) \\
& + 2Dt^2 \left( 2\xi_l\omega_l + \frac{\omega_l^2}{\omega_h} \right) (z^3 + z^2 - z - 1) + \omega_l^2Dt^3(z^3 + 3z^2 + 3z + 1)
\end{aligned} \tag{4.7}$$

$$= \frac{b_3z^3 + b_2z^2 + b_1z + b_0}{a_3z^3 + a_2z^2 + a_1z + a_0} = \frac{\dot{w}_i(z)}{i(z)} = H_i(z) \tag{4.8}$$

Where  $Dt$  is the sampling time and:

$$\left\{ \begin{array}{l}
b_3 = 8Lm_a + 4(Rm_a + Lc_a)Dt + 2(Rc_a + Lk_a + k_{em})^2Dt^2 + Rk_aDt^3 \\
b_2 = -24Lm_a - 4(Rm_a + Lc_a)Dt + 2(Rc_a + Lk_a + k_{em})^2Dt^2 + 3Rk_aDt^3 \\
b_1 = 24Lm_a - 4(Rm_a + Lc_a)Dt - 2(Rc_a + Lk_a + k_{em})^2Dt^2 + 3Rk_aDt^3 \\
b_0 = -8Lm_a + 4(Rm_a + Lc_a)Dt - 2(Rc_a + Lk_a + k_{em})^2Dt^2 + Rk_aDt^3 \\
a_3 = m_ak_{em} \left[ \frac{8}{\omega_h} + 4Dt \left( 1 + \frac{2\xi_l\omega_l}{\omega_h} \right) + 2Dt^2 \left( 2\xi_l\omega_l + \frac{\omega_l^2}{\omega_h} \right) + \omega_l^2Dt^3 \right] \\
a_2 = m_ak_{em} \left[ -\frac{24}{\omega_h} - 4Dt \left( 1 + \frac{2\xi_l\omega_l}{\omega_h} \right) + 2Dt^2 \left( 2\xi_l\omega_l + \frac{\omega_l^2}{\omega_h} \right) + 3\omega_l^2Dt^3 \right] \\
a_1 = m_ak_{em} \left[ \frac{24}{\omega_h} - 4Dt \left( 1 + \frac{2\xi_l\omega_l}{\omega_h} \right) - 2Dt^2 \left( 2\xi_l\omega_l + \frac{\omega_l^2}{\omega_h} \right) + 3\omega_l^2Dt^3 \right] \\
a_0 = m_ak_{em} \left[ -\frac{8}{\omega_h} + 4Dt \left( 1 + \frac{2\xi_l\omega_l}{\omega_h} \right) - 2Dt^2 \left( 2\xi_l\omega_l + \frac{\omega_l^2}{\omega_h} \right) + \omega_l^2Dt^3 \right]
\end{array} \right.$$

From Eq. 4.8 it can be obtained the linear difference equation that allows to compute  $\dot{w}_i(k)$ .

$$(b_3z^3 + b_2z^2 + b_1z + b_0) i(z) = (a_2z^3 + a_2z^2 + a_1z + a_0) \dot{w}_i(z) \tag{4.9}$$

$$\begin{aligned}
\dot{w}_i(k) = & \frac{b_3}{a_3}i(k) + \frac{b_2}{a_3}i(k-1) + \frac{b_1}{a_3}i(k-2) + \frac{b_0}{a_3}i(k-3) \\
& - \frac{a_2}{a_3}\dot{w}_i(k-1) - \frac{a_1}{a_3}\dot{w}_i(k-2) - \frac{a_0}{a_3}\dot{w}_i(k-3)
\end{aligned} \tag{4.10}$$

**Voltage term**

$$\text{Substituting } s = \frac{2z-1}{Dt(z+1)}$$

$$\begin{aligned}
H_v(s) &= \frac{\dot{w}_v(s)}{v(s)} = \frac{s^2 m_a + s c_a + k_a}{m_a k_{em} (s^2 + 2\zeta_l \omega_l s + \omega_l^2) \left(1 + \frac{s}{\omega_h}\right)} \\
&= \frac{1}{m_a k_{em}} \frac{k_a + \frac{2c_a z-1}{Dt(z+1)} + \frac{4m_a(z-1)^2}{Dt^2(z+1)^2}}{\frac{8}{\omega_h Dt^3} \frac{(z-1)^3}{(z+1)^3} + \frac{4}{Dt^2} \frac{(z-1)^2}{(z+1)^2} + \frac{8\zeta_l \omega_l}{\omega_h Dt^2} \frac{(z-1)^2}{(z+1)^2} + \frac{4\zeta_l \omega_l}{\omega_h Dt} \frac{z-1}{z+1} + \frac{2\omega_l^2}{\omega_h Dt} \frac{z-1}{z+1} + \omega_l^2} \\
&= \frac{1}{m_a k_{em}} \frac{4m_a Dt(z-1)^2(z+1) + 2c_a Dt^2(z-1)(z+1)^2 + k_a Dt^3(z+1)^3}{\frac{8}{\omega_h} (z-1)^3 + 4Dt \left(1 + \frac{2\zeta_l \omega_l}{\omega_h}\right) (z-1)^2(z+1) + 2Dt^2 \left(2\zeta_l \omega_l + \frac{\omega_l^2}{\omega_h}\right) (z-1)(z+1)^2 + \omega_l^2 Dt^3 (z+1)^3} \\
&= \frac{1}{m_a k_{em}} \frac{4m_a Dt(z^3 - z^2 - z + 1) + 2c_a Dt^2(z^3 + z^2 - z - 1) + k_a Dt^3(z^3 + 3z^2 + 3z + 1)}{\frac{8}{\omega_h} (z^3 - 3z^2 + 3z - 1) + 4Dt \left(1 + \frac{2\zeta_l \omega_l}{\omega_h}\right) (z^3 - z^2 - z + 1) + 2Dt^2 \left(2\zeta_l \omega_l + \frac{\omega_l^2}{\omega_h}\right) (z^3 + z^2 - z - 1) + \omega_l^2 Dt^3 (z^3 + 3z^2 + 3z + 1)} \\
\end{aligned} \tag{4.11}$$

$$= \frac{d_3 z^3 + d_2 z^2 + d_1 z + d_0}{c^3 z^3 + c_2 z^2 + c_1 z + c_0} = \frac{\dot{w}_v(z)}{v(z)} = H_v(z) \tag{4.12}$$

Where  $Dt$  is the sampling time and:

$$\begin{cases}
d_3 = 4m_aDt + 2c_aDt^2 + k_aDt^3 \\
d_2 = -4m_aDt + 2c_aDt^2 + 3k_aDt^3 \\
d_1 = -4m_aDt - 2c_aDt^2 + 3k_aDt^3 \\
d_0 = 4m_aDt - 2c_aDt^2 + k_aDt^3 \\
c_3 = m_a k_{em} \left[ \frac{8}{\omega_h} + 4Dt \left( 1 + \frac{2\xi_l \omega_l}{\omega_h} \right) + 2Dt^2 \left( 2\xi_l \omega_l + \frac{\omega_l^2}{\omega_h} \right) + \omega_l^2 Dt^3 \right] \\
c_2 = m_a k_{em} \left[ -\frac{24}{\omega_h} - 4Dt \left( 1 + \frac{2\xi_l \omega_l}{\omega_h} \right) + 2Dt^2 \left( 2\xi_l \omega_l + \frac{\omega_l^2}{\omega_h} \right) + 3\omega_l^2 Dt^3 \right] \\
c_1 = m_a k_{em} \left[ \frac{24}{\omega_h} - 4Dt \left( 1 + \frac{2\xi_l \omega_l}{\omega_h} \right) - 2Dt^2 \left( 2\xi_l \omega_l + \frac{\omega_l^2}{\omega_h} \right) + 3\omega_l^2 Dt^3 \right] \\
c_0 = m_a k_{em} \left[ -\frac{8}{\omega_h} + 4Dt \left( 1 + \frac{2\xi_l \omega_l}{\omega_h} \right) - 2Dt^2 \left( 2\xi_l \omega_l + \frac{\omega_l^2}{\omega_h} \right) + \omega_l^2 Dt^3 \right]
\end{cases}$$

From Eq. 4.12 can be obtained the linear difference equation that allows to compute  $\dot{w}_v(k)$ .

$$(d_3z^3 + d_2z^2 + d_1z + d_0)v(z) = (c_3z^3 + c_2z^2 + c_1z + c_0)\dot{w}_v(z) \quad (4.13)$$

$$\begin{aligned}
\dot{w}_v(k) &= \frac{d_3}{c_3}v(k) + \frac{d_2}{c_3}v(k-1) + \frac{d_1}{c_3}v(k-2) + \frac{d_0}{c_3}v(k-3) \\
&\quad - \frac{c_2}{c_3}\dot{w}_v(k-1) - \frac{c_1}{c_3}\dot{w}_v(k-2) - \frac{c_0}{c_3}\dot{w}_v(k-3)
\end{aligned} \quad (4.14)$$

#### 4.1.4 S-GUF plate simulation

In this section the expression for the reconstruction of the plate transverse velocity in Eq. 4.5 is tested numerically on the S-GUF plate model, both in frequency and time domain. The discrete formulation derived above is implemented, with a sampling frequency of 20kHz.

In Figure 4.12 are compared the velocity frequency response obtained with the original expression - Eq. 4.1 - with the modified expression - Eq. 4.5 - and that of the real velocity of the plate. Comparing it with all the plots obtained with the SDOF plate model can be recognized two peaks: at 30Hz the actuator resonance and at 85Hz the first mode of the plate. All the following peaks are higher order natural modes of the plate, note that since the actuator is placed at the center of the plate, not all the modes are excitable. As a matter of fact, comparing it with the modes of Figure 3.19, it can be

seen that only the first - 85Hz - the fourth - 209Hz - and the eighth - 370Hz - are present, all others having nodal lines passing through the center of the plate are not excited.

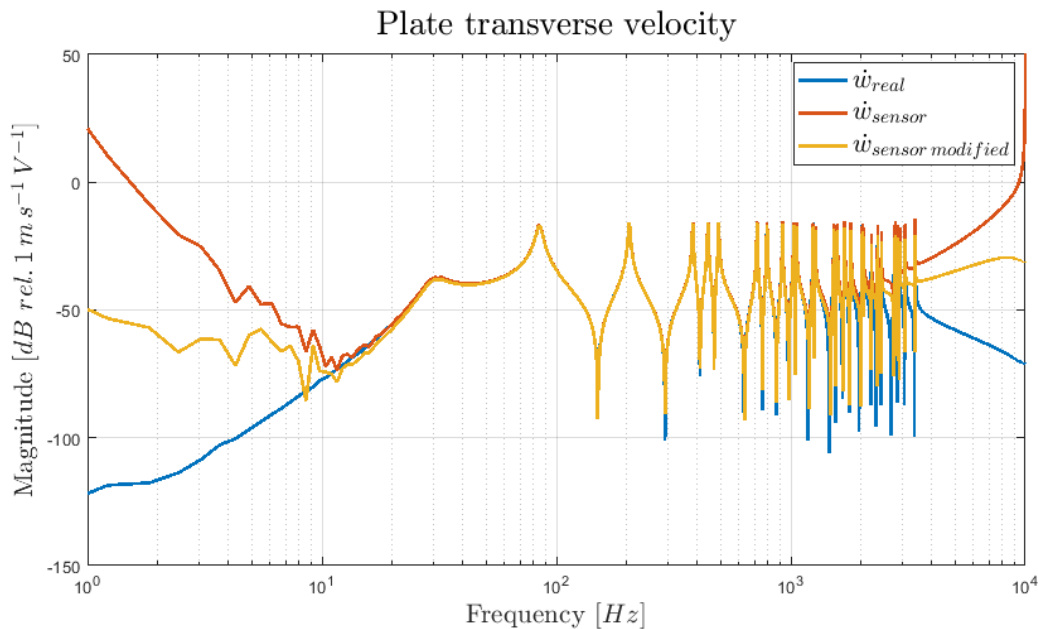


**Figure 4.12:** Comparison of the reconstructed velocity frequency response, obtained both with the modified and the original expression, with the real velocity of the plate.

The poor performances of the original expression for the reconstruction of the plate velocity, are confirmed by the diverging magnitude of the frequency response at both low and high frequency. The modified equation instead still gives a good reconstruction of the velocity in the frequency range of interest, while keeping bounded the magnitude outside.

Considering only the frequency domain response, it is not straightforward to understand if the modification introduced so far are enough to achieve a stable reconstruction. Looking directly at the time history of the velocity can give a much more direct understanding of what Figure 4.12 means.

In Figure 4.13 is depicted the time evolution of the velocity obtained in a 10 seconds simulation. The velocity obtained with the original formulation diverges from the real one. This is the effect of the very low frequency components in Figure 4.12.

From figure 4.14, instead, can be seen that the modified version gives much better results. Therefore the low and high frequency tails of Figure 4.12, although not superimposed to the real velocity, have a magnitude low enough not to affect the velocity in the time domain.

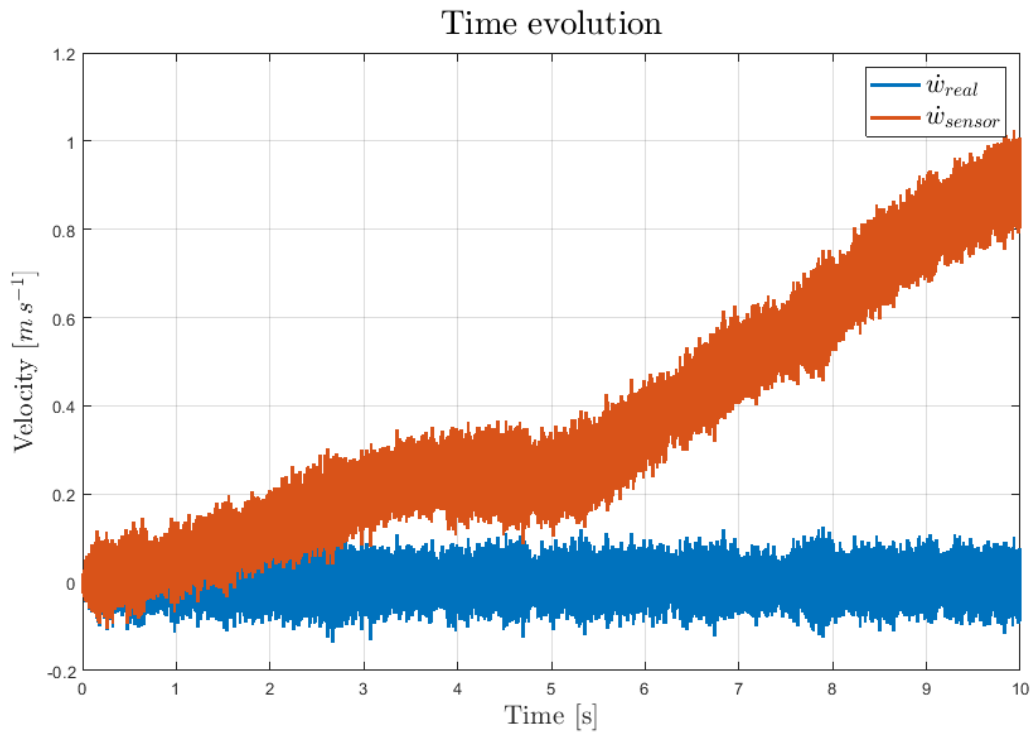


**Figure 4.13:** Comparison of the velocity reconstructed with the original expression and the real transverse velocity of the plate at the actuator location.

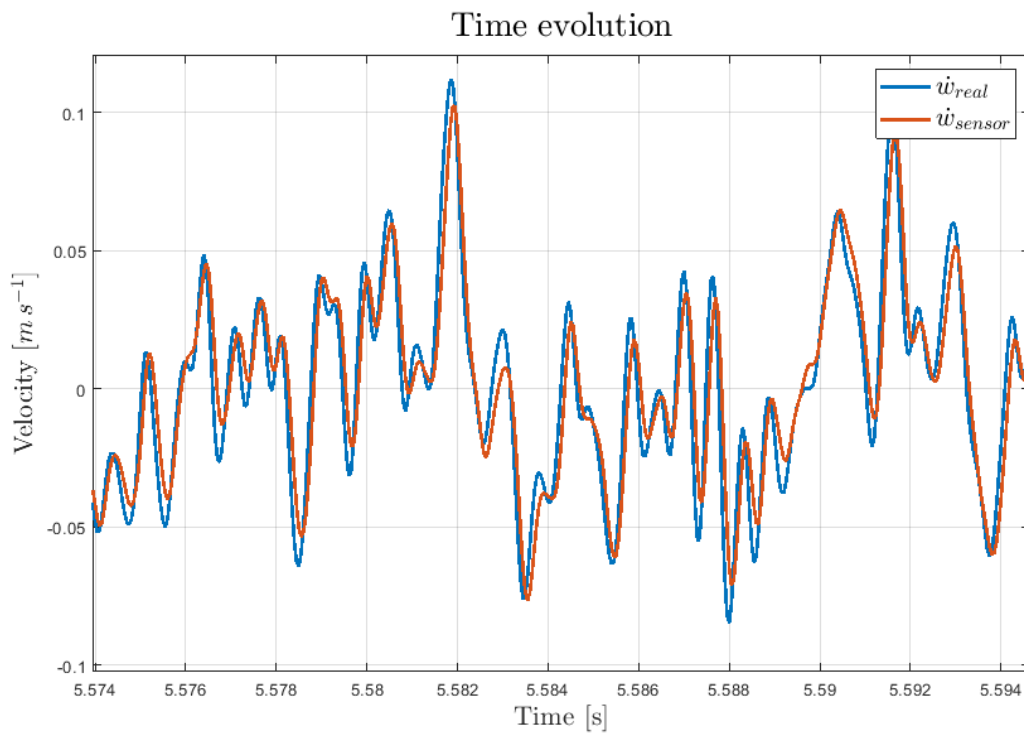


**Figure 4.14:** Comparison of the velocity reconstructed with the modified expression and the real transverse velocity of the plate at the actuator location.



## 4.2 Inertial mass velocity

In this section the reconstruction of the inertial mass velocity is briefly tested. The expression has been derived in Chapter 2 and is reported in Eq. 4.15 for the sake of clarity.

$$\dot{z}(s) = \left[ \frac{(R + sL)(sc_a + k_a) + sk_{em}^2}{s^2 m_a k_{em}} \right] i(s) - \left[ \frac{sc_a + k_a}{s^2 m_a k_{em}} \right] v(s) \quad (4.15)$$

It can be modified in a similar way to what has been done for the transverse plate velocity. The poles in the origin shall be substituted with negative real part complex conjugate poles, but being  $H_i(s)$  already proper, the addition of the high frequency pole is not required.

$$\dot{w}(s) = \left[ \frac{(R + sL)(sc_a + k_a) + sk_{em}^2}{m_a k_{em} (s^2 + 2\xi_l \omega_l s + \omega_l^2)} \right] i(s) - \left[ \frac{sc_a + k_a}{m_a k_{em} (s^2 + 2\xi_l \omega_l s + \omega_l^2)} \right] v(s) \quad (4.16)$$

In Figure 4.15 and 4.16 are depicted the performances of the reconstruction expression respectively in frequency and time domain, compared to the real velocity of the inertial mass of the control actuator. Also in this case the reconstruction is satisfying. It can be noticed that the response is dominated by the slow mode of the actuator 30Hz, while the modes of the plate are present with lower amplitude.

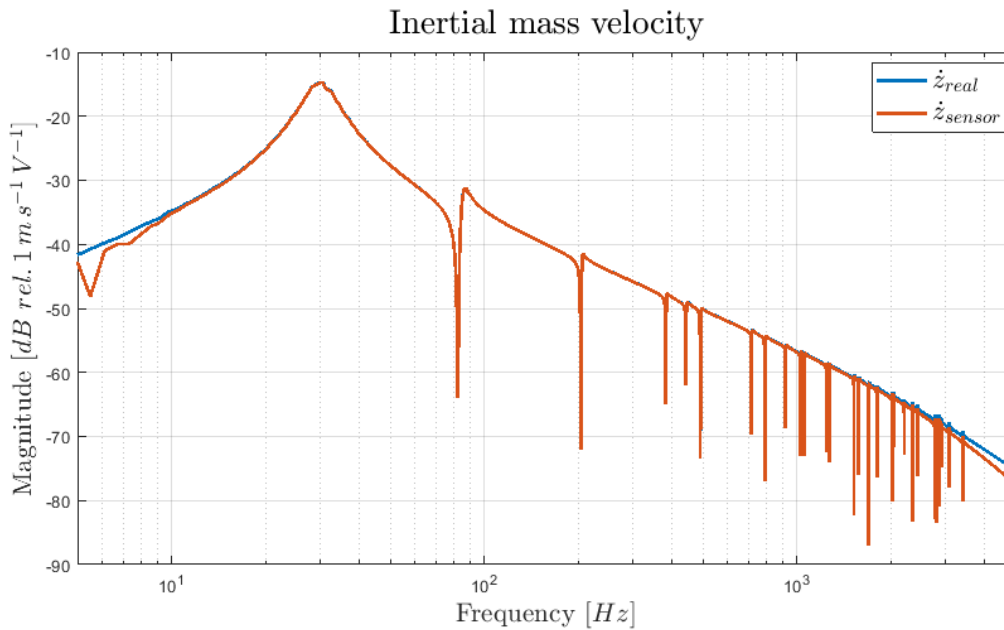


**Figure 4.15:** Comparison of the reconstructed inertial mass velocity frequency response, with the real velocity.

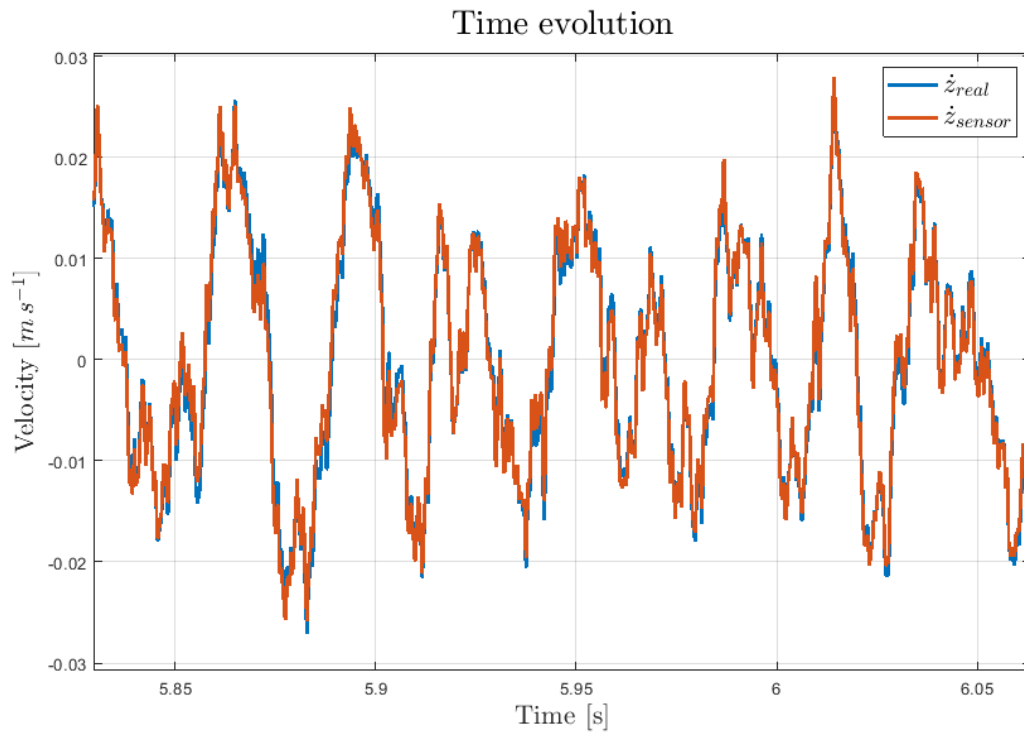


**Figure 4.16:** Comparison of the velocity reconstructed with the modified expression and the real velocity of the inertial mass of the control actuator.

# Chapter 5

## Sensor-actuator model: Experimental Testing

In this section the reconstruction of the velocity derived in Chapter 4 is implemented in a real-time skyhook control logic in laboratory. Filters are added and the basis for future developments are layed.

### 5.1 Control scheme

In Figure 5.1 the experimental setup is depicted. Two inertial actuators are mounted on the thin aluminum plate, one in the center (A) used for the control, and one in a corner (B) used to introduce the disturbance. The disturbance signal generated by the desktop computer is a white noise filtered by an anti-aliasing filter (KEMO filter). Between the control actuator and the power amplifier (LEPAI 2), the current sensor - LPRS 6-NP - and the differential scope - PICO TA043 - are placed, so that current and tension can be acquired for the reconstruction of the transverse plate velocity at the control location. Two accelerometers are also used, one glued on top of the inertial mass, and the second on the lower face of the plate, exactly in correspondence of the actuator A. Indeed, it can be useful to compute the velocity also by pseudo-integration of the acceleration for comparison purposes.

Once tension and current are available, the control action is computed trough the discrete realization of the plate velocity equation derived in Chapter 4. Ahead of doing so, it has been necessary to filter both tension and current signals, both at low and high frequencies.

The low frequency filtering - roughly below  $1\text{Hz}$  - is mandatory to remove acquisition offset from current and voltage measures.

The high frequency filtering is a crucial aspect of the project, indeed the most critical problem and - as thoroughly explained later - still not completely solved.

Both filters are realized as digital elliptic second order filters, but for sure other solution could be considered in future evolution of the design.

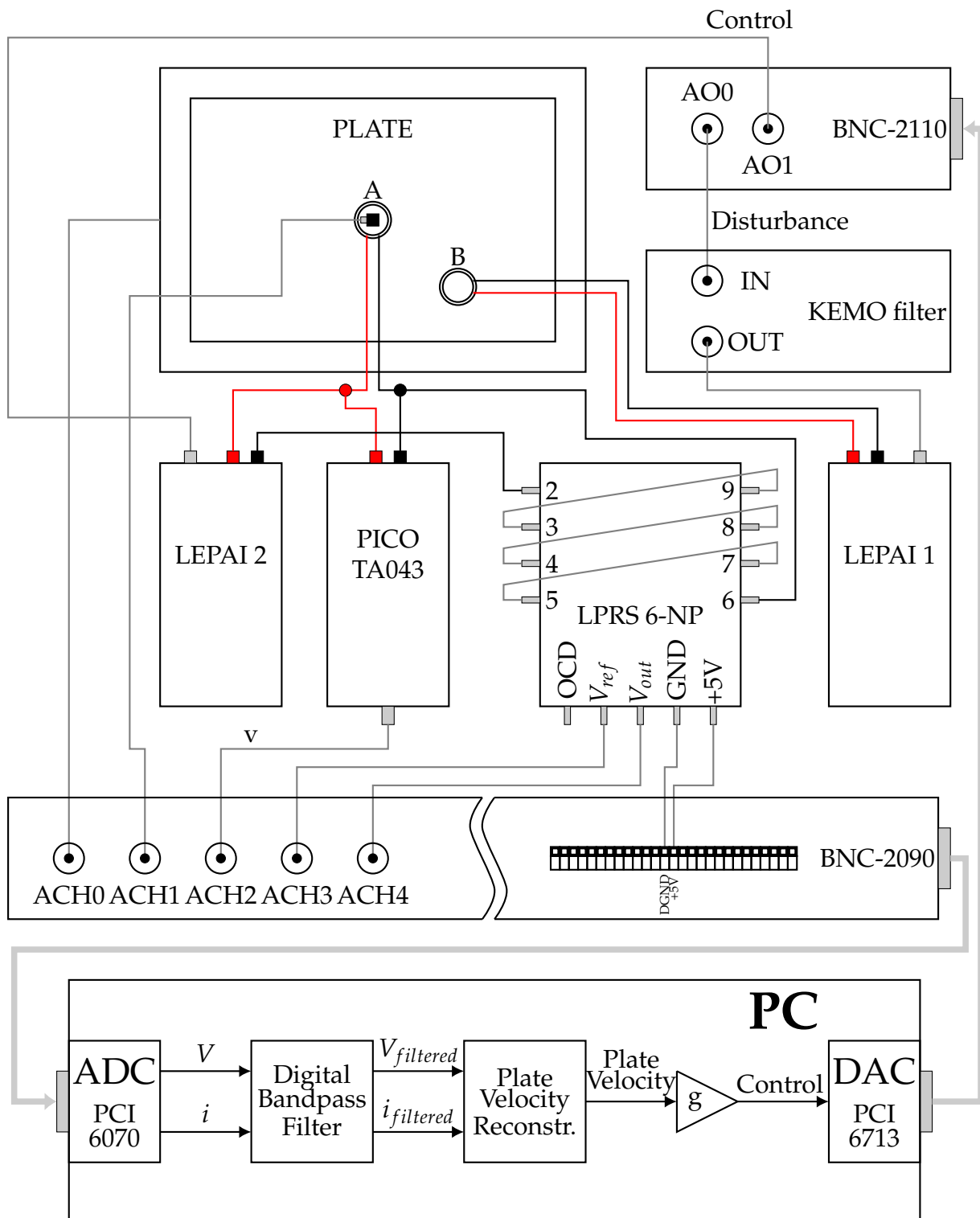


**Figure 5.1:** Scheme of the experimental setup used for the testing of the skyhook control logic with the reconstruction of the plate velocity.

## 5.2 Data acquisition system and real-time control

Before discussing the results of the digital skyhook control strategy, some clarification about the way current and voltage are acquired are needed.

As can be seen in Figure 5.1 and explained above, the desktop PC runs a real-time routine that is responsible for multi-channel acquisition. The acquired data of the present time instant are used to compute the control action to be provided to the actuator at the next time instant. Therefore the PC - at any discrete time instant - has to acquire all channels, carry out the required computations, and send out the results. Of course there is a limitation on the frequency at which the PC can repeat the cycle just described. As a matter of fact, it has been checked that with the configuration in Figure 5.1, the maximum sampling rate is about 15kHz.

The *data acquisition system* (DAQ) - namely the *analog to digital converter* (ADC) and the *digital to analog converter* (DAC) in Figure 5.1 - works on  $2^{12}$  levels. This means that input and outputs can assume only 4096 well defined values, any signal falling between two level is approximated to the nearest. What just described holds for both ADC and DAC, meaning that the signal to be acquired is mapped on one of the 4096 fixed input levels. In the same way the control action computed from current and voltage is sent out with the nearest value among the 4096 fixed output levels. The only difference between input and output boards is the range on which the  $2^{12}$  levels are distributed. The output range is fixed at  $\pm 10V$  while the input range can be selected among seven settings from  $\pm 10V$  to  $\pm 0.1V$ , with the aim of having the best resolution in the specific operating condition.

As seen in Chapter 3 the current sensor maps the current to be measured in a voltage, that can be directly acquired with the ADC. Such voltage, proportional to the original current, is given as:

$$V_{out} = V_{ref} + 0.625 \frac{N_p \cdot I}{I_{PN}}$$

where  $I_{PN} = 6A$  and  $N_p = 4$ .  $V_{ref}$  is about 2.5V, although it can have small fluctuations in time and has to be acquired to increase the accuracy. From what has been said it's evident that the data acquisition system shall have at least a range including +2.5V, the nearest being  $\pm 5V$ .

The accelerometers can be acquired too with a  $\pm 5V$  range - as a matter of fact their output falls exactly between this values.

Such range is surely more than enough to perform the measure of the voltage. The maximum voltage that the power amplifier is able to provide to the speaker is about  $\pm 12V$  at saturation - condition from which it has to be kept away. Having in mind that the differential probe PICO TA043 reduces the voltage by a factor of ten, a limit of  $\pm 1.2V$  is obtained, falling well inside the acquisition range.

Unfortunately, as will be seen later, in operating conditions the voltage value - dependent on the control gain - is much smaller than  $\pm 12V$ : with  $g = 10$  it does not exceed  $\pm 1V$ , becoming  $\pm 0.1V$  after the differential probe - meaning that only the 2% of the 12 bits resolution is used. The same is true for the current. Although  $V_{out}$  oscillates around 2.5V, the amplitude of such an oscillation is only about one fifth of the voltage

since the electrical resistance is about  $5\Omega$  - meaning  $\pm 0.2A$  - that the current sensor maps to  $\pm 0.08V$ , again only the 1.6% of the resolution is used.

About the resolution of the output signal, similar conclusions can be drawn. In the previous example where a control gain of 10 was supposed, the control action happens to be about  $\pm 0.2V$ . Considering that the output range is fixed and equal to  $\pm 10V$ , again only the 2% of the range is exploited.

Such a poor resolution causes a bad signal to noise ratio. As will be explained later, very little can be done to improve the situation without a proper preconditioning of the signal to be acquired. Therefore all experiments are performed in the aforementioned situation, and some guidelines for future development are drawn at the end.

## 5.3 Filters

This section addresses the need of filtering current and voltage signals, as anticipated at the beginning of this chapter. The filters described in the following are elliptic filters, chosen for their steep transition band and for the nearly linear phase.

All filters are digitally implemented in the real-time software running on the laboratory PC and their coefficients are obtained through the MATLAB function `ellip`, that receives as inputs the desired order, the cutting frequency, the required attenuation and the pass-band maximum ripples.

### 5.3.1 Low frequency filtering

Figure 5.2 shows the velocity frequency response, computed with and without the high-pass filter. Comparing the latter with the one obtained by pseudo-integration of the plate acceleration, the need of an high-pass filter is rather evident. The excess in low frequencies components is due to different phenomena:

- A poor signal to noise ratio in the current and voltage signals at low frequencies, that is worsened due to the characteristics of the velocity reconstruction described in Chapter 4.
- The offset in the acquisition of the signals that introduces a DC component, affecting the very low frequency range.
- The low frequency oscillation of the baseline for the current measurement. Although both  $V_{out}$  and  $V_{ref}$  are acquired to improve precision, it cannot be excluded that some oscillation may survive.

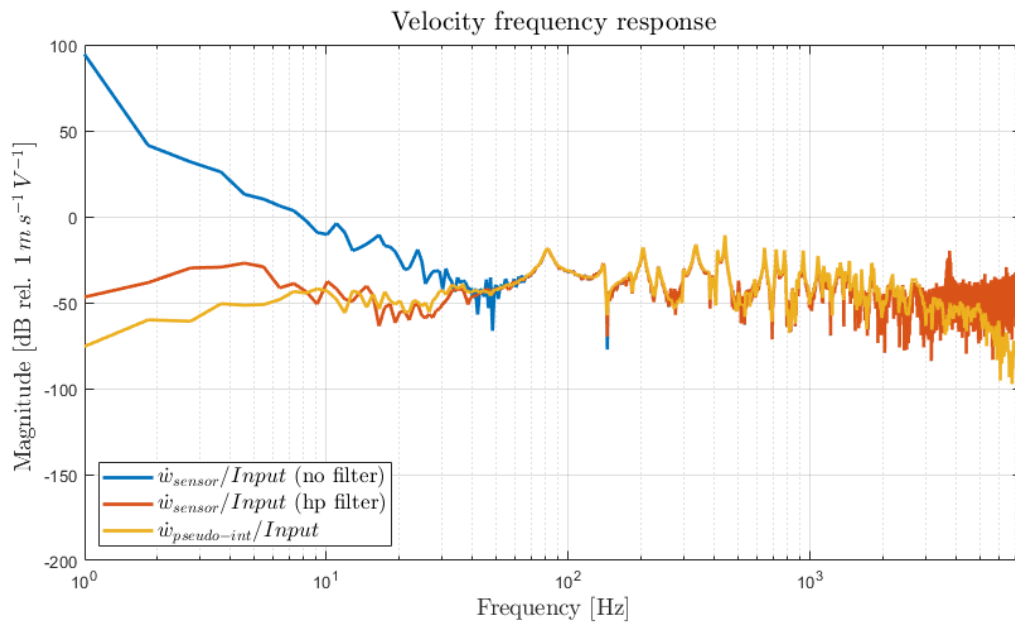


**Figure 5.2:** Velocity frequency response: comparison filtered and unfiltered, with the one obtained by pseudo-integration of the acceleration.

In Figure 5.2 it is also depicted the velocity frequency response when filtered current and voltage are used in the reconstruction. In the low frequencies range the plot is much more similar to that of the pseudo-integrated acceleration, while high frequencies are not affected. The difference is even more striking looking at the reconstructed transverse plate velocity in time domain, Figure 5.3.

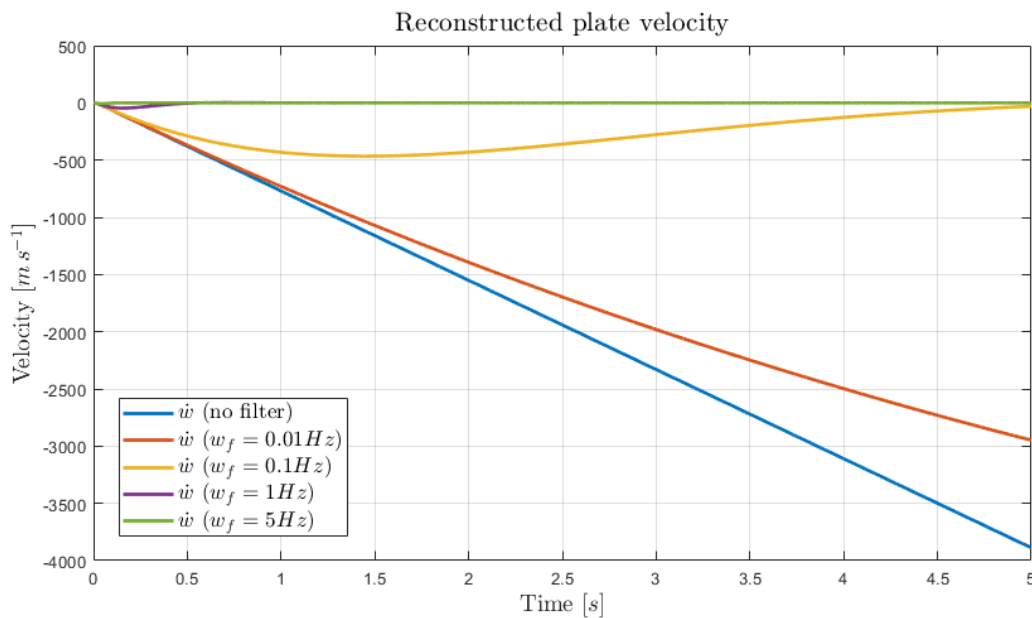


**Figure 5.3:** Effect of the filter cutting frequency on the transient of the velocity.

Without filters, the velocity diverges due to the acquisition offsets of current and volt-

age. The effect of the filter is indeed to bring to zero the offset in current and voltage signals, in a time that depends on the cutting frequency of the filter (the higher the cutting frequency, the faster the filtering action, see Figure 5.4). During the transient of the filter, an offset is still present in the filtered voltage and current signals, still causing the error to build up in the reconstructed velocity. But since the offset is now going to zero in few seconds, the filtering action built-in in the velocity reconstruction formula discussed in Chapter 4, is able to promptly bring the error to zero. Figure 5.2 shows the different transient time for the reconstructed velocity, the higher the cutting frequency of the filter the lesser the maximum error reached, the lesser the settling time.

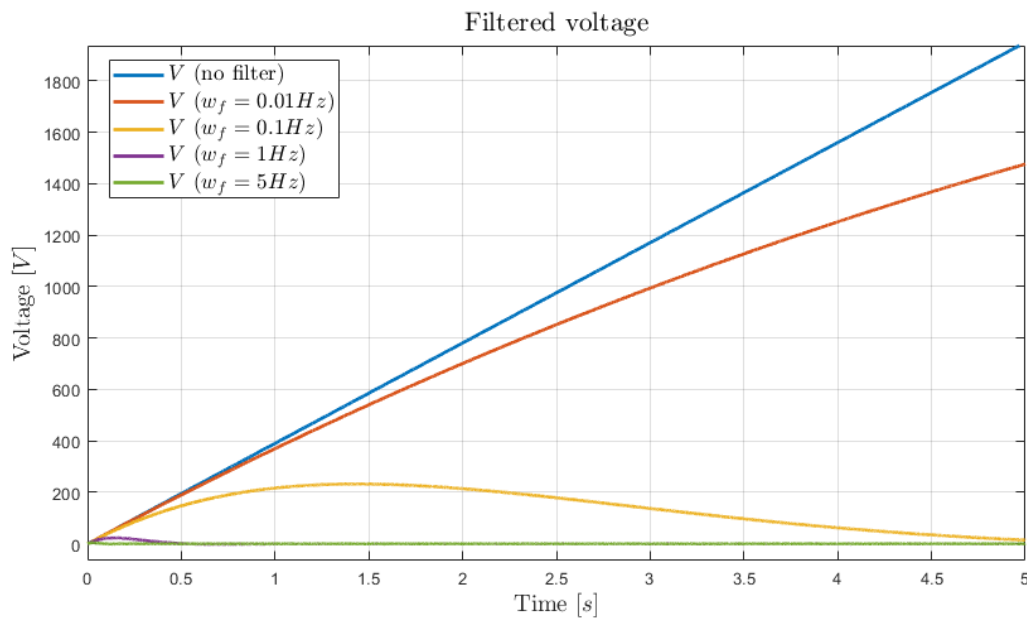


*Figure 5.4: Effect of the filter cutting frequency on the transient of the voltage.*

The choice of the filter cutting frequency shall be a compromise between velocity of the response - that would require the highest possible cutting frequency - and the preservation of a good reconstruction of the velocity - that requires a cutting frequency lower than the frequency range of interest. The filter implemented in the following is depicted in Figure 5.5 and has a cutting frequency around  $5Hz$ .

The non infinitesimal response time of the filter would impose to wait the end of the transient in the filtered current and voltage, before starting to compute the velocity in order to avoid the error to build up. But thanks to the filtering action supplemented by the negative real part poles in the velocity reconstruction transfer functions, it's possible to avoid this step, simplifying the implementation. The abovementioned poles does not influence the response once the transient is ended, but they simplify switching on the system, avoiding having to wait for the filter's transient to end.



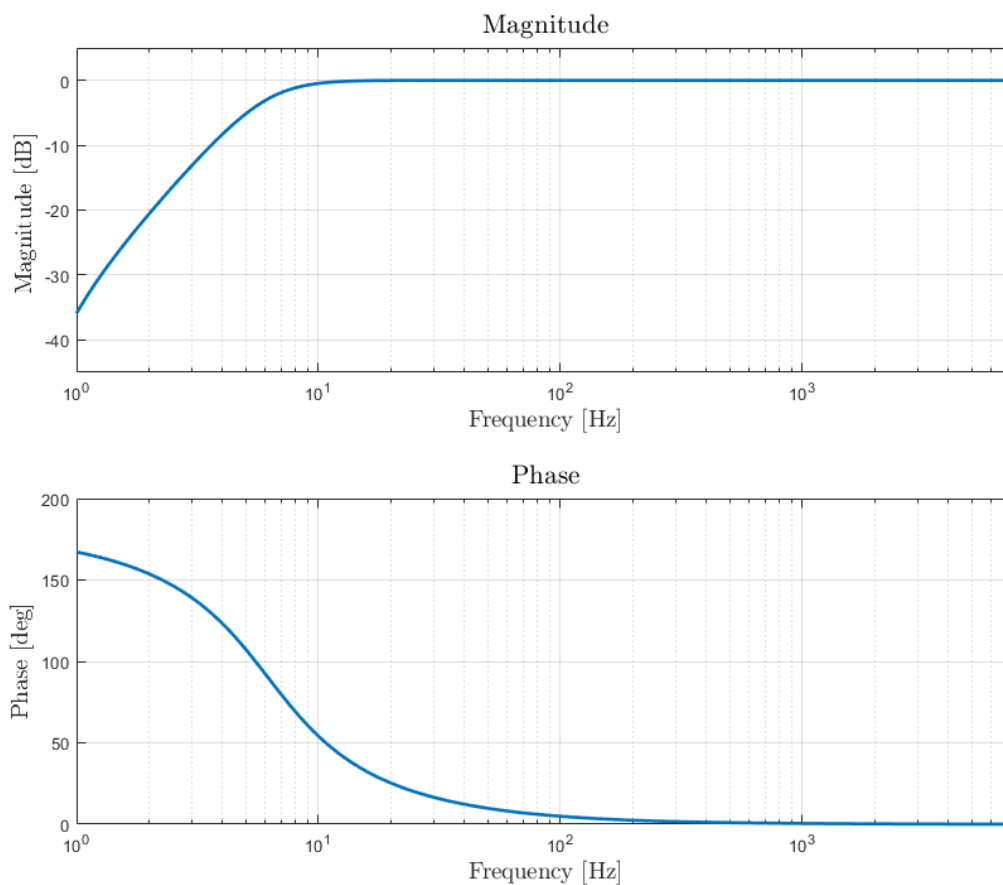


*Figure 5.5: High-pass filter for current and tension.*

### 5.3.2 High frequency filtering

The low resolution achievable in the measures of current and voltage described above leads to a poor signal to noise ratio at all frequencies. This problem is particularly evident in the high frequency range because - as it will be explained below - it's worsened by some interaction between ADC and DAC. To catch this last phenomenon, although the following considerations are made about the open loop case, the system will always be connected in closed loop, with a control gain equal to zero. Indeed in theory the two conditions are equivalent, but since in the closed loop a new source of noise arises, it would be misleading to make an analysis of the pure open loop case, because this additional error would be missed and it would become more difficult to catch it analyzing directly the closed loop control performances. Figure 5.6 shows the poor correspondence at high frequency of the transverse plate velocity obtained from current and voltage, with that obtained by pseudo-integration of the acceleration. Both are obtained in open-loop, without a low-pass filter. Looking at Figure 5.6 can be seen that the approximation is good at least up to 2kHz, after that the noise in the reconstructed velocity gets more and more evident. Moreover there are two peaks - at 3750Hz and 7500Hz - quite difficult to comprehend.

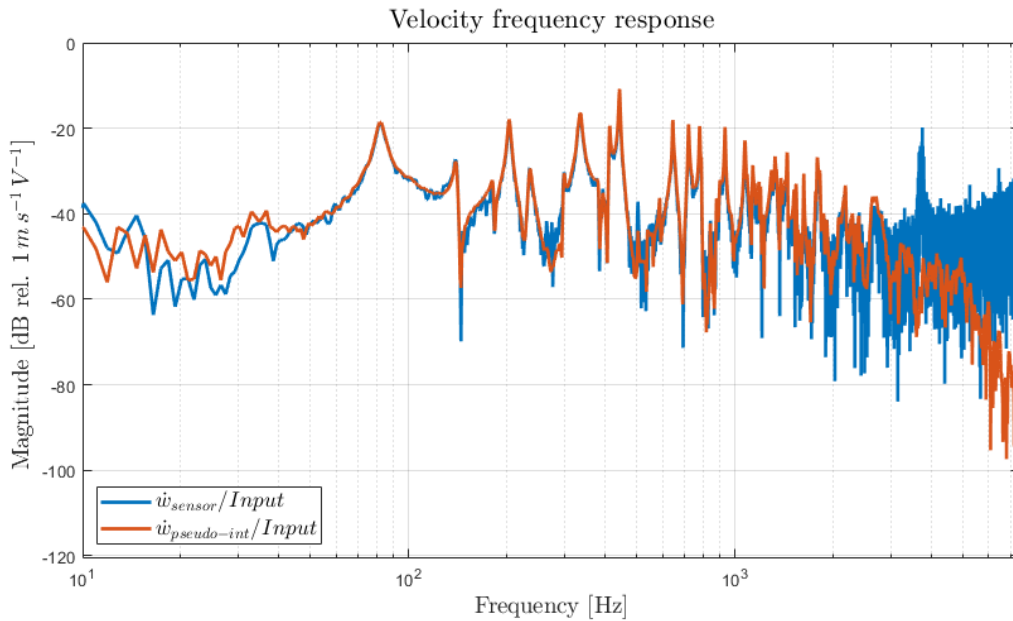


**Figure 5.6:** Comparison of the velocity frequency response for the reconstructed plate velocity and the one obtained by pseudo-integration of the acceleration.

While the noise is easily explained by the considerations made above about the low resolution of the measures, to understand where the two peaks come from, additional discussion is needed.

The velocity is computed acquiring the voltage applied to the control actuator and the current flowing into it. But the control action - simply a multiple of the computed velocity - is then applied as a driving voltage to the control actuator. Both operations - acquisition and sending the control action to the actuator - are performed with the same sampling frequency, in this case  $15\text{kHz}$ . It will be now taken in exam a peculiar case that makes the meaning of the peaks rather evident. Figure 5.7 reports a short time history of the acquired voltage, when the system has a control gain equal to zero (equivalent to open loop). In this conditions the voltage applied to the actuator is zero, and so it should be the voltage acquired. It is not so for different reasons:

- There's an offset of about  $150\text{mV}$ . Although it could seem huge, it has to be remembered that the voltage is acquired after its amplitude being reduced by a factor of ten with the differential probe PICO TA043. Therefore the offset right after acquisition is ten times smaller,  $15\text{mV}$ . Probably, it could be reduced calibrating the probe, but in any case it does not represent a problem thanks to the high-pass filter introduced in the previous section.
- The value of the voltage should be constant but it is not acquired on a fixed level. It oscillates taking at least the first two levels - and looking at longer time scales it reaches also the forth - on both side of the mean value, introducing some high frequency oscillations. In Figure 5.7 are highlighted two patterns that frequently repeat on the whole time history, having period of two and four sampling times, meaning frequencies of  $7500\text{Hz}$  and  $3750\text{Hz}$ .

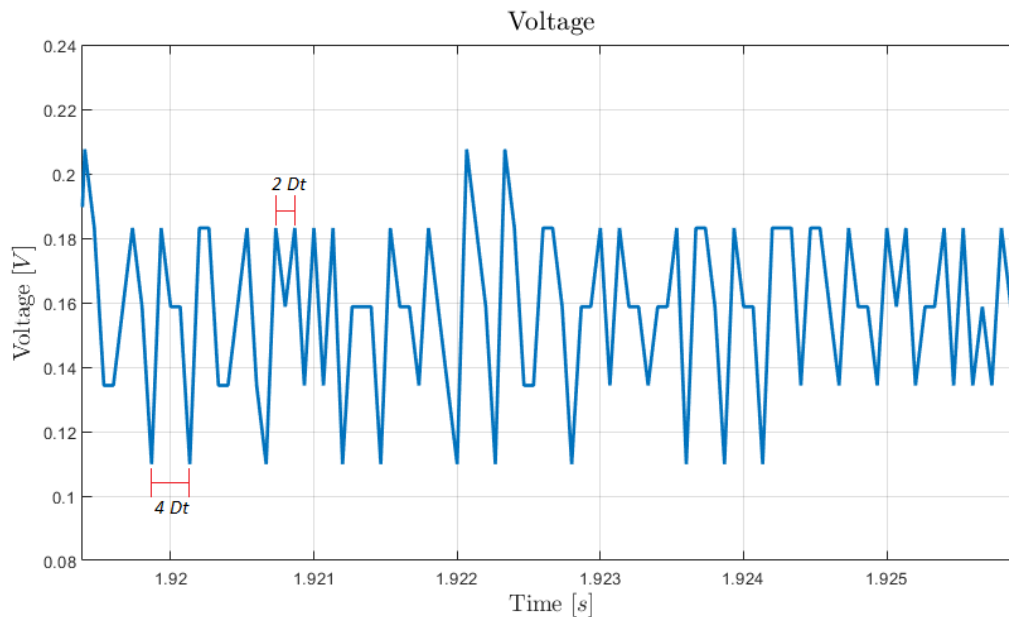


*Figure 5.7: Voltage to the control actuator acquired when the control gain is zero.*

This explains the presence of the two peaks at those frequencies, but with some additional consideration also the relative magnitude of the peaks above the underlying noise can be justified. Remembering that the ADC uses 12 bits, 4096 levels, and that the acquisition range is overall  $10V$  wide, the between-level amplitude is  $2.44mV$ . The signal, after being acquired, has to be multiplied by a factor of ten to give the voltage, so a distance between two levels of  $24.4mV$  is obtained, in good agreement with the steps of Figure 5.7. As said above the noise encompasses four levels on both sides of the average value. This means that it has an amplitude 8 times larger than the resolution of the ADC, therefore shall be 8 times larger than the noise floor. A factor of 8 is equivalent to  $18dB$ , which is more or less the amount by which the peaks in Figure 5.6 stand out from the base noise.

The case just analysed is peculiar, but the conclusions drawn are general. In fact the noise at  $3750$  and  $7500Hz$  is due to the fact that those frequencies are constantly fed back from the control to the acquisition, and then are used to compute the new control action, entering in a loop that amplifies them about eight times. In fact it will be seen that such peaks are present also with higher control gains, and will also be the cause of control spillover.

Having understood that the high frequency noise comes from the poor acquisition of current and tension, it's straightforward to suppose that filtering the signals after acquisition could improve the signal to noise ratio at high frequency. In Figure 5.8 a second order elliptic filter has been added, with cutting frequency of about  $1kHz$  (Figure 5.9). The reconstructed velocity remains good in the range of interest, the high frequency noise is reduced at a level even lower than in the reference curve and the two peaks are largely reduced too.

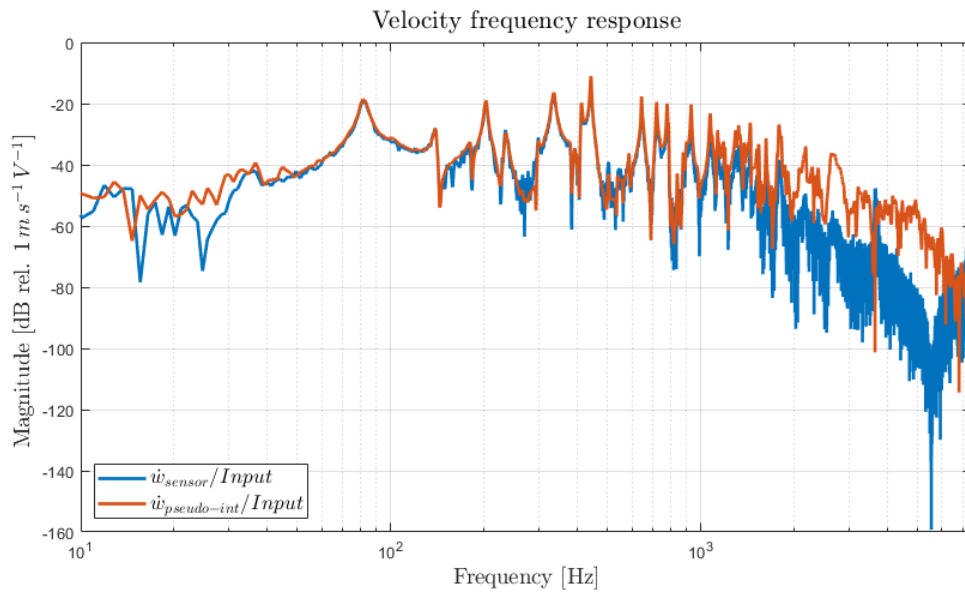


**Figure 5.8:** Comparison of the velocity frequency response for the reconstructed plate velocity when voltage and current are filtered, with the velocity obtained by pseudo-integration of the acceleration.

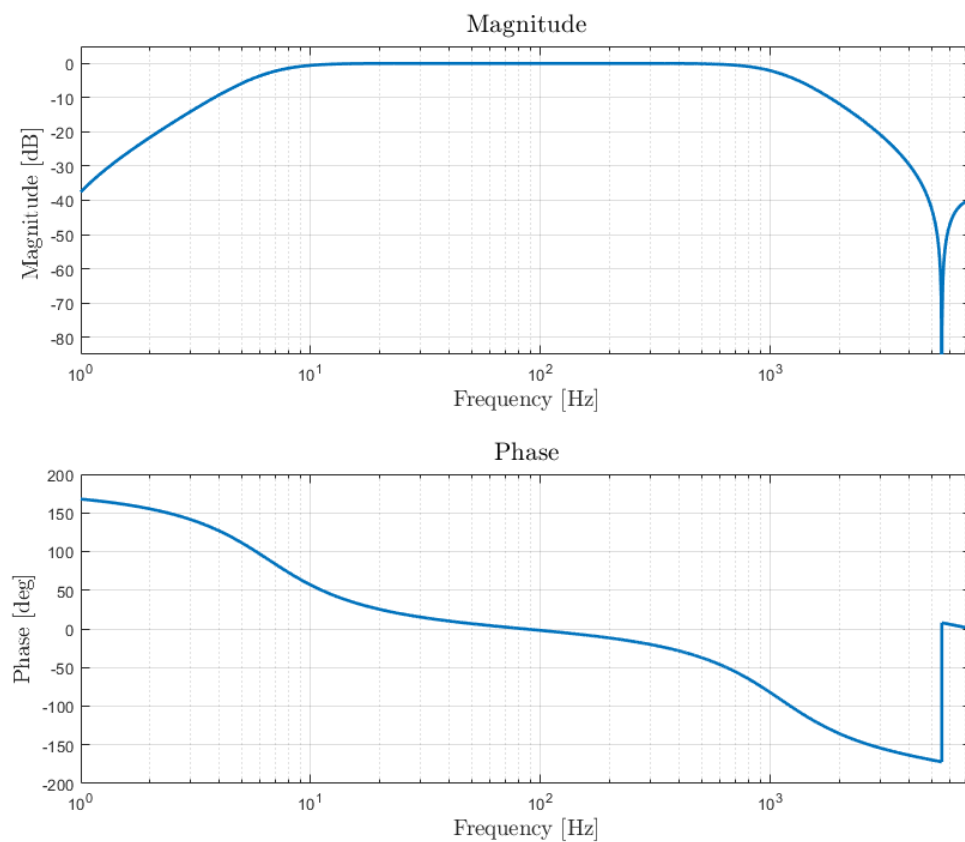


**Figure 5.9:** Band-pass filter for current and tension.

One could think to use a filter having an arbitrarily high order, but has to be kept in mind that the phase lag introduced by the filter translates in a delay of the computed velocity with respect to the real one, therefore in a delay of the control action.

Up to now the disturbance applied to the plate has been a white noise, without any limitation in frequency. One could be brought to think that filtering the disturbance at high frequency could bring some improvements to the situation just described. Figure 5.10 shows the effect of filtering the disturbance at 800Hz. The velocity obtained by pseudo-integration of the acceleration is indeed filtered, in fact if the disturbance has no components at high frequency, the same should apply to the acceleration of the plate, therefore also to the velocity. On the contrary, there are no effects on the velocity obtained from current and voltage, as an additional proof that in this case the noise is due only to the poor acquisition of the electrical quantities. Nevertheless in the following the disturbance filtering will be used sometimes, to avoid high frequency modes of the structure to be excited.

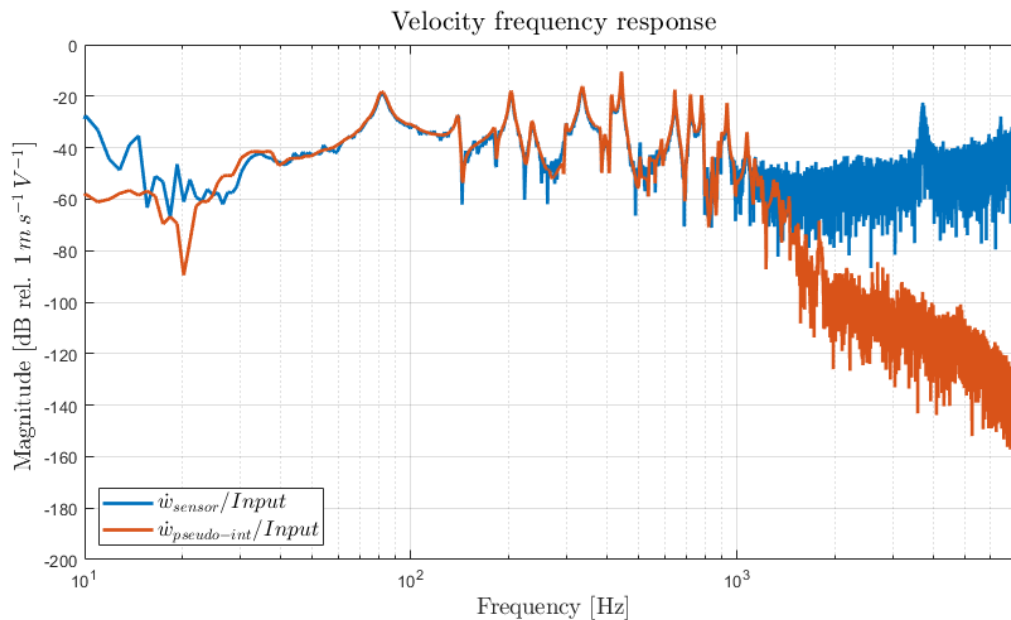


**Figure 5.10:** Comparison of the velocity frequency response for the reconstructed plate velocity and the pseudo-integration acceleration, when the disturbance is filtered.

## 5.4 Closed loop control

In this section the performances of the skyhook control, when the transverse plate velocity reconstructed from current and voltage is used, are analyzed.

Figure 5.11 reports, for comparative purposes, the performances of the control system - in terms of the plate acceleration frequency response at the control point - when the feedback action is determined from the velocity obtained by pseudo-integration of the transverse plate acceleration.

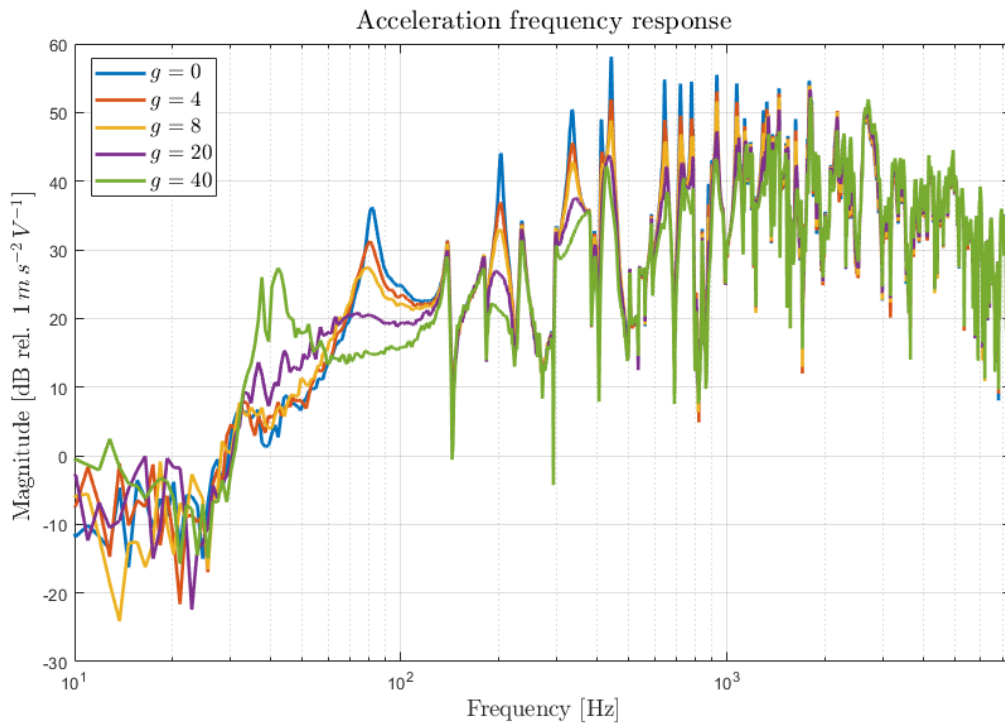


**Figure 5.11:** Acceleration frequency response at different control gains, when the pseudo-integration method is used.

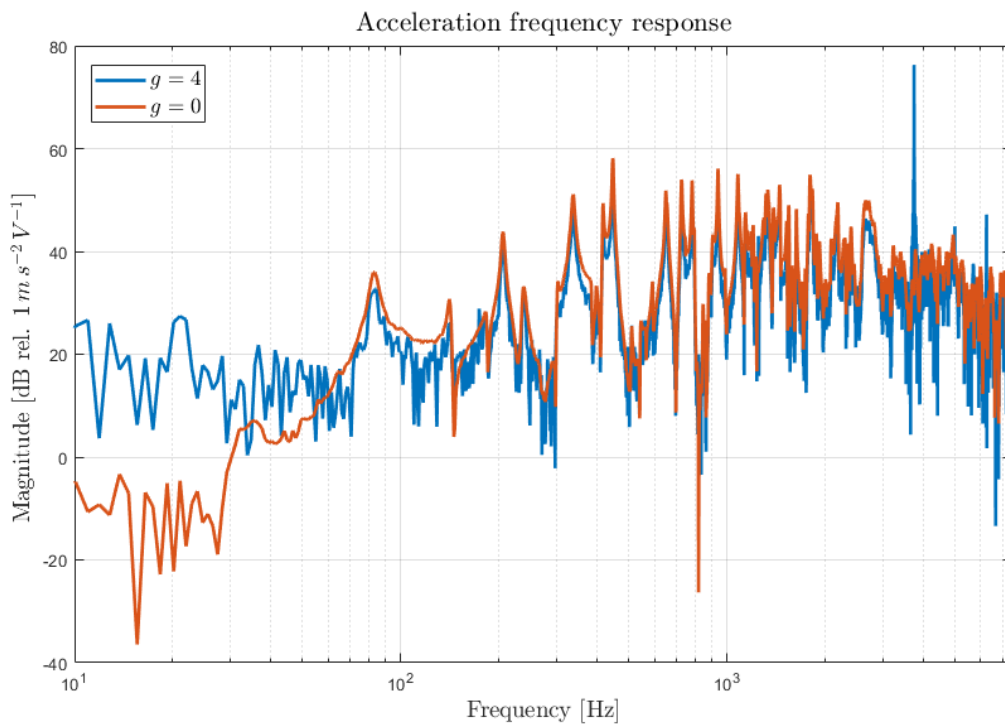


**Figure 5.12:** Acceleration frequency response at different gains, if no filtering of current and voltage is introduced.

All the following plots represent the response of the system in terms of the transverse plate acceleration, when the control gain is computed from the velocity reconstructed by current and voltage.

Figure 5.12 shows what happens if the unfiltered current and voltage are used. A control gain of 4 is enough to make the plate ringing at 3750Hz due to the amplification of the noise.

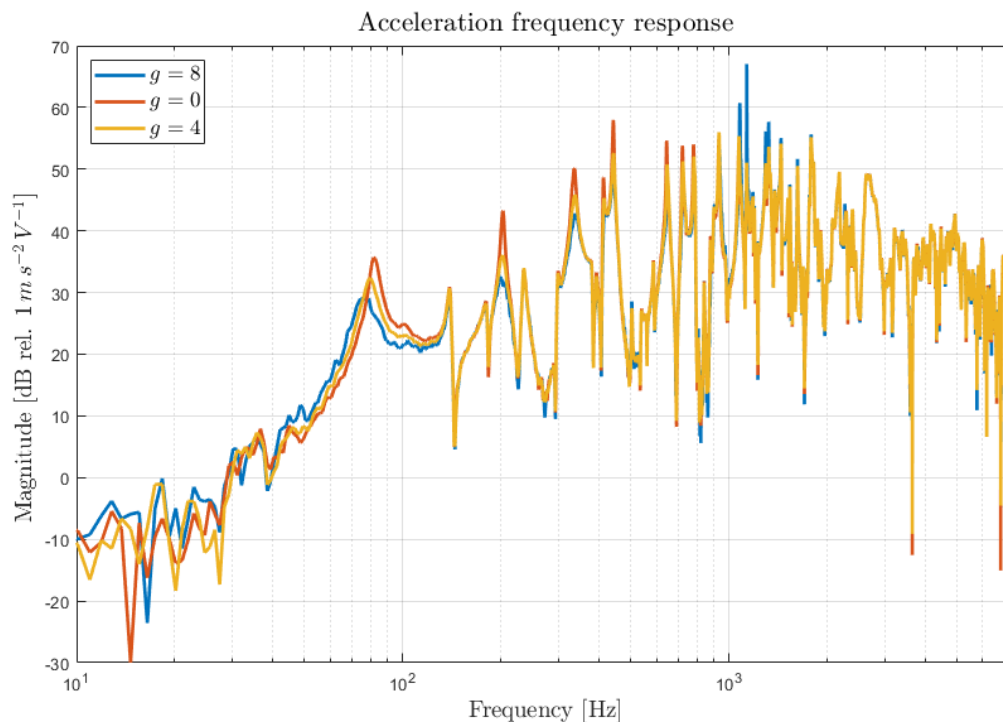


**Figure 5.13:** Acceleration frequency response at different gains, if band-pass filtering of current and voltage is introduced.

If the band-pass filter described in the previous section is introduced, the control performance are improved. Figure 5.13 shows the acceleration frequency response for different control gains, until instability arises. Note that at frequencies lower than 800Hz (filter's cutting frequency), the skyhook control, with low gains, has performances comparable to those in Fig. 5.11. However when the gain reaches 8, there's an amplification of some natural frequencies of the plate in the range from 1000 and 1500Hz. This range coincides with the initial portion of the transition band of the filter, Figure 5.14.

The reason is that the filter introduces a phase lag in current and voltage, causing the reconstructed velocity to be delayed with respect to the real one, causing, in turn, the control action to be applied too late. If the filter introduces a phase lag larger than  $90^\circ$  at high frequencies, the system becomes unstable. This can be understood imagining a control force acting on the plate more and more delayed with respect to the plate velocity. With  $0^\circ$  delay the force always opposes the instantaneous velocity, with the effect of reducing it. If the delay is increased there will be some instants - after the velocity

of the plate has changed sign, but before the control force has changed its - when the force pushes the plate in the same direction it is already moving. If the fraction of time in which the control force works to increase the speed of the plate is small, than the control performance are reduced but the system remains stable. When such a fraction exceeds 50%, than the control action passes the most of the time working in the wrong direction. As it is easy to imagine, this condition is verified if the control is delayed more than  $90^\circ$  with respect to the plate velocity.

The instability in Figure 5.13 arises in a frequency range where the filter phase lag is larger than  $90^\circ$  but the filtering action has not yet occurred - note that indeed the filter's gain is less than  $-10dB$ .

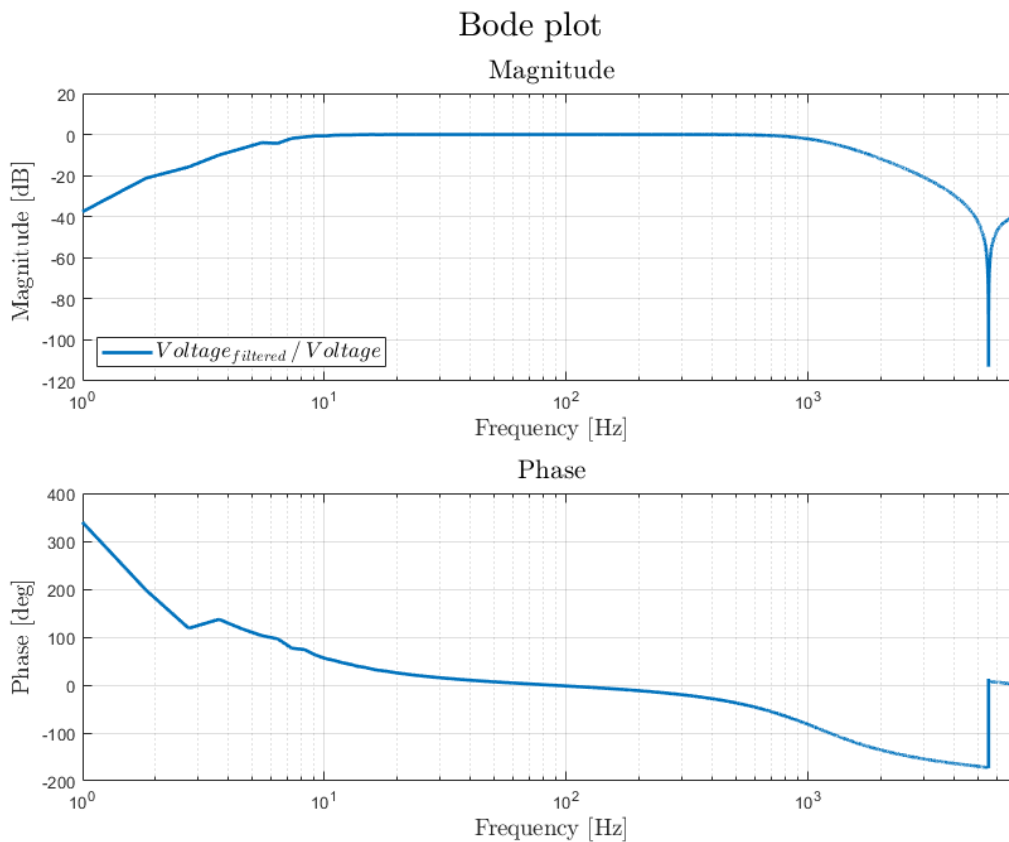


*Figure 5.14: Band-pass filter transfer function.*

The logical conclusion would be to use a first order filter, so to limit the maximum phase lag to  $90^\circ$ , but unfortunately there's not enough separation between the noise to be filtered and the band of interest. Therefore a second order filter has to be used, although with an higher sampling frequency the first order filter could be reconsidered.

In Figure 5.15 a second filter, again elliptic but with two separate high frequency poles, is proposed. Note that the  $-90^\circ$  phase are reached at higher frequencies. Figure 5.16 shows the acceleration response obtained with this new filter at different gains. Although it has been possible to increase only slightly the maximum gain, it's evident



that the instability has moved to higher frequency, supporting the explanation given above. With gain equal to 10, three peaks arise from 1500Hz to 2000Hz. Please note that the first two peaks were present also at lower gains, meaning they are modes of the structure excited by the control action due to the high phase lag, while the third peak - around 2000Hz - is present only at gain equal 10. It has been verified with an oscilloscope that the last peak is an alias frequency of some noise at 13kHz, mirrored about the Nyquist frequency 7500Hz, whose origins are not clear.

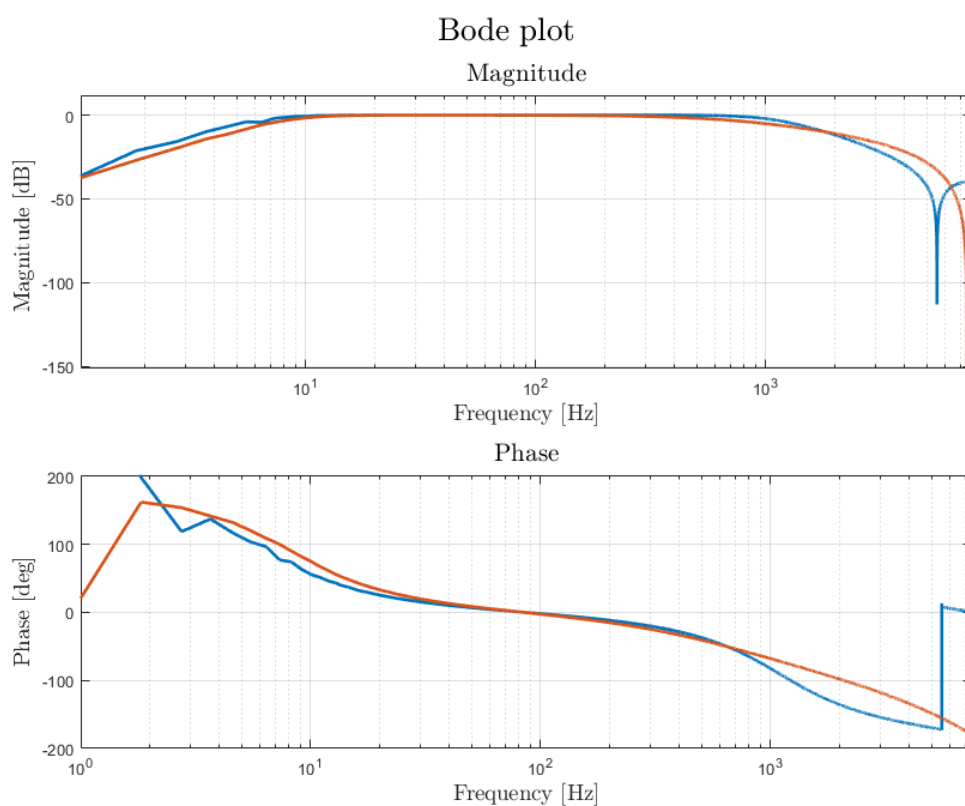


*Figure 5.15: Comparison of the two band-pass filter transfer function.*

In Figure 5.17 the disturbance is filtered to reduce the control spillover. The effect on the modes of the plate is good, but no effect on the peak due to the aliasing is obtained. Indeed the 13kHz signal is probably due to some dynamics of the acquisition system, therefore filtering the disturbance can't have any effect on it.

Any further attempt with slightly different filters have brought to similar results.

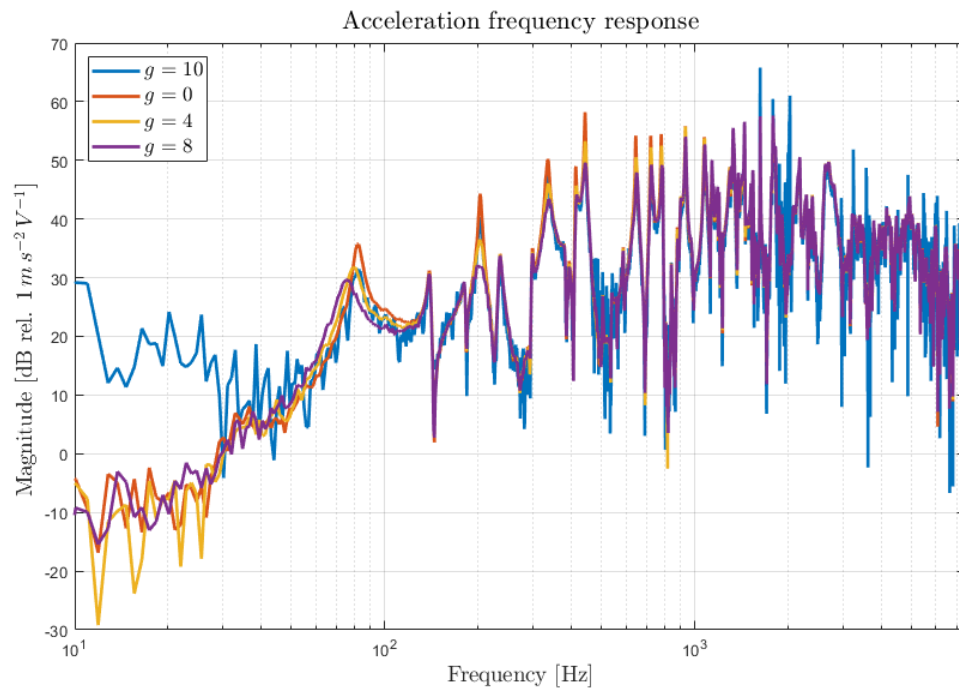


**Figure 5.16:** Acceleration frequency response at different gains, if the second band-pass filter for current and voltage is used.

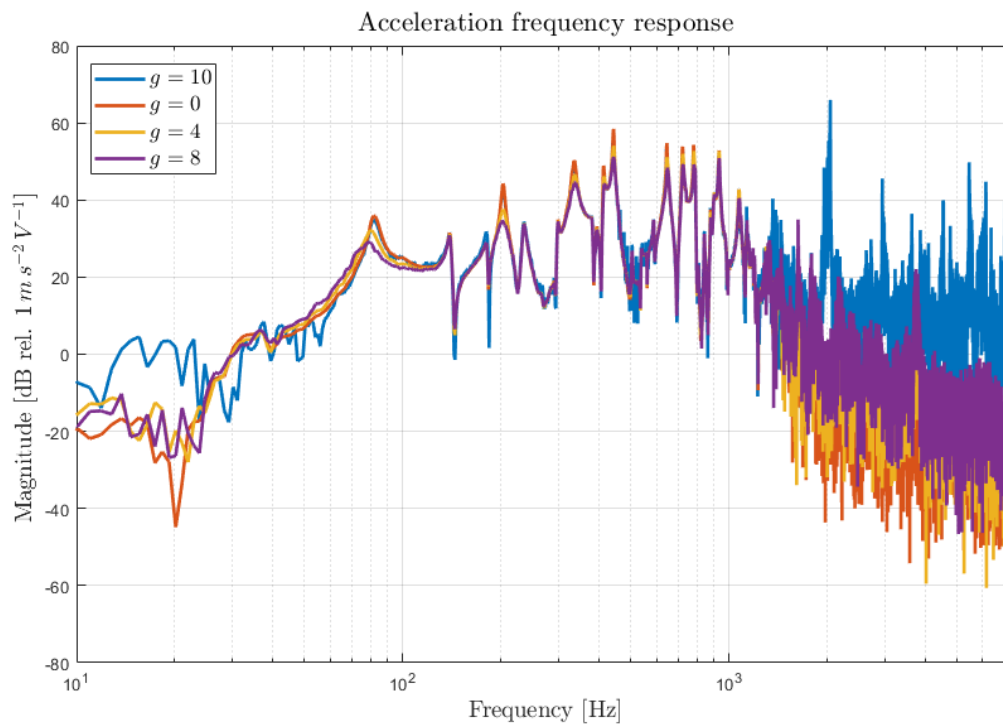


**Figure 5.17:** Acceleration frequency response at different gains, if the second band-pass filter for current and voltage is used and if the disturbance is filtered.

Figure 5.18 shows a comparison between the real and the reconstructed transverse plate velocity. Note that the latter is highly noisy and slightly delayed with respect to the former.

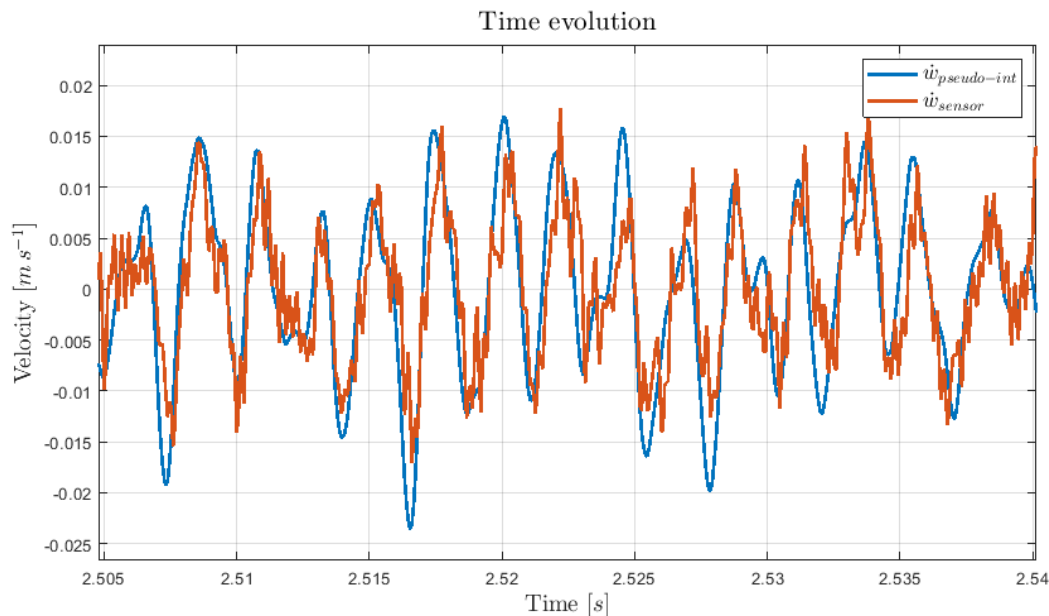


**Figure 5.18:** Comparison between the real and the reconstructed transverse plate velocity in time domain.

## 5.5 Double loop control logic

The tests presented in this chapter made clear that the first instability to manifest when the control gain is increased, happens at high frequency. This is a different result with respect to that obtained basing the feedback loop on the plate velocity computed by pseudo-integration of the acceleration - Figure 5.11 - where the instability arises, at higher gains, due to interaction of the first mode of the structure with the actuator dynamics.

In the work by Di Girolamo [11] two ways to reduce the low frequency instability are presented, one of them consisting on a local feedback on the inertial device, to modify the actuator dynamics in the range of frequency where the instability arises. This control loop is based on feeding back to the actuator a quantity proportional - through a local gain  $g_l$  - to the inertial mass velocity, in order to artificially increase the damping of the actuator itself.

Such additional control logic usually would add complexity to the implementation, since another accelerometer would be required to be placed on the inertial mass of the actuator. Thanks to the self-sensing approach instead, no hardware has to be added, and the inertial mass velocity can be computed from the very same current and voltage measurements used to compute the transverse plate velocity.

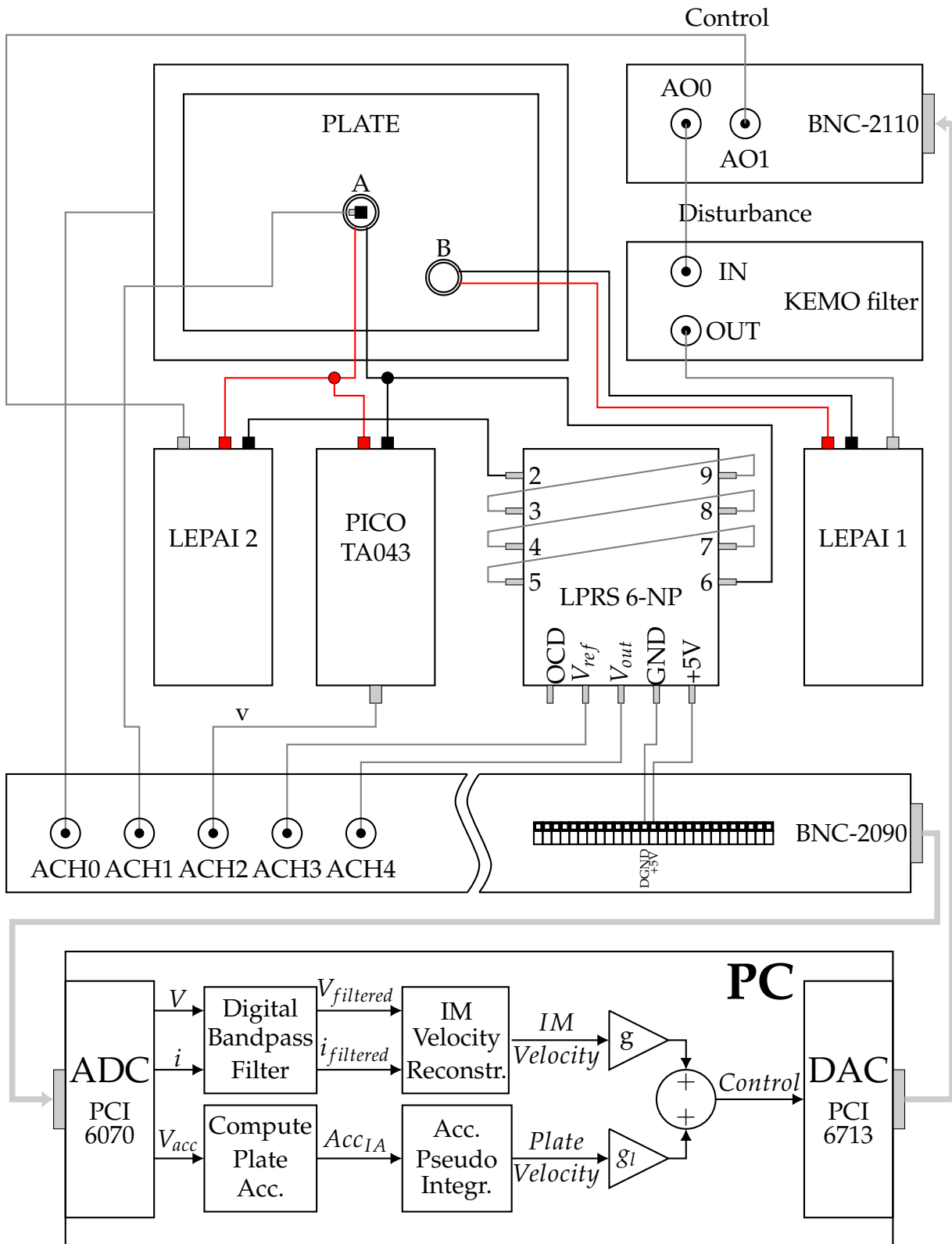
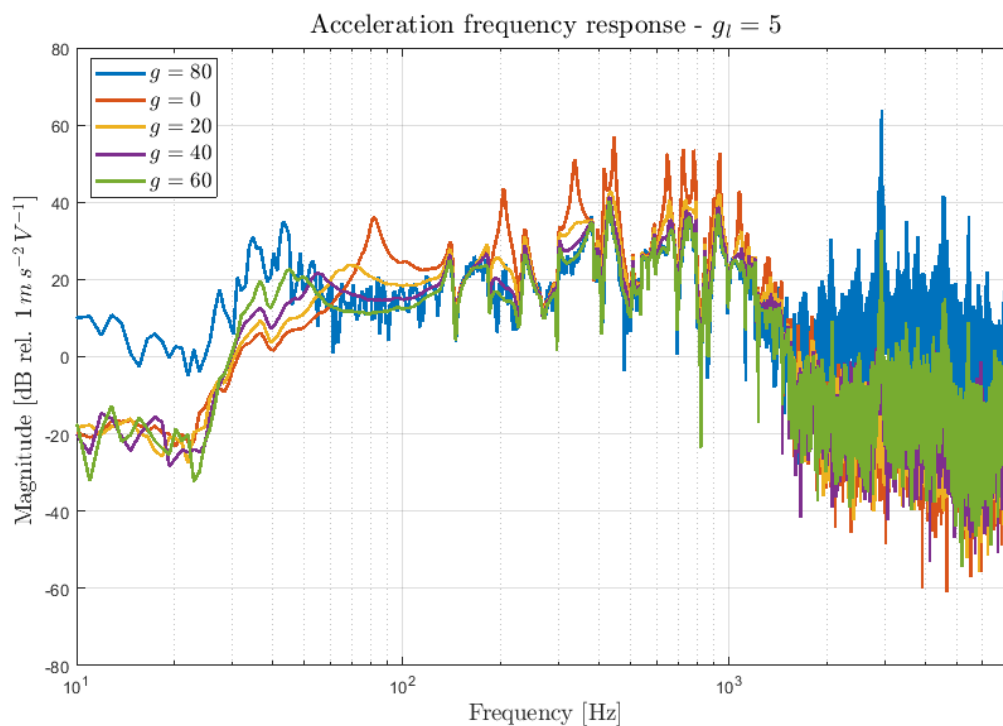


Figure 5.19: Experimental setup used to test the inertial mass velocity reconstruction.

In this section the reconstruction of the inertial mass velocity is tested in the control logic just described. It would be futile to test it on a control logic where the plate velocity is obtained through reconstruction too, because, for the problems described before, it would be impossible to reach gains high enough to require the local feedback loop. Therefore, in the following, only the inertial mass velocity is computed from current and tension, while the transverse plate velocity is obtained by pseudo-integration of the acceleration, as in Figure 5.19.

As it can be expected also the reconstruction of the inertial mass velocity suffers the same issues described before, making it impossible to use high local gains. Indeed it has been seen that  $g_l = 10$  give rise to control spillover at high frequency, therefore the local gain is limited to 5 in the following.

In Figure 5.20 it is shown the acceleration frequency response of the plate at the control location, for the double loop control system with different control gains.



**Figure 5.20:** Acceleration frequency response for different control gains and a local gain of 5.

Comparing it with Figure 5.11 it can be seen that has been possible to increase the gain. With  $g = 40$  - the previous limit for the onset of instability - the control still works well, at 60 high frequency noise starts to be amplified and at 80 instability is reached simultaneously at high and low frequency. Since the control spillover at high frequency is due to the issues of the velocity reconstruction, it could have been expected that limiting the local gain on the reconstructed inertial mass velocity, and increasing only the control gain on the plate velocity obtained by pseudo-integration, it would not have led to high frequency spillover. This is not true because, even if the disturbance is filtered and does not have much power in the high frequency band, when the control -

carrying a signal proportional to the reconstructed inertial mass velocity - is applied, the plate receives some of the high frequency noise due to the velocity reconstruction. Such a noise is picked up by the accelerometer entering in the transverse plate velocity after the pseudo-integration. The result is that the high frequency noise is amplified also by the control gain, causing instability to be reached simultaneously at low and high frequency, inducing quite unpredictable vibrations to the plate.

## 5.6 First order low-pass filter

As previously said, one way to improve the control performances without having to change dramatically the experimental setup, could be to use a first order filter for filtering current and voltage, in order to keep the control action delay below  $90^\circ$ . To do so, there must be enough distance between the frequency range of interest and the high frequency noise to be canceled. In the setup discussed above such condition is far to be true, since the upper limit of the range of interest has been fixed to  $1kHz$  and the first noise peak is  $3750Hz$ . In this section a test using a first order filter is presented, to demonstrate the above hypothesis under restricted conditions, in order to draw some guidelines for future developments.

Removing from the real-time software all not essential functions, it has been possible to increase the sampling frequency to  $20kHz$ , moving toward higher frequency also the acquisition noise. Since the frequency separation is still limited, the low-pass filter is designed with a lower cutting frequency, reducing the working bandwidth of the control system. In Figure 5.21 is depicted the bode plot of the designed filter, composed of the usual second order elliptic high-pass filter with  $5Hz$  cutting frequency, in addition to the new first order elliptic low-pass filter with a  $300Hz$  cutting frequency.

Figure 5.22 shows the performance of the closed loop control system in terms of acceleration frequency response, when the transverse plate velocity used in the feedback loop is reconstructed from current and voltage filtered as described above. Comparing it with Figure 5.17 it can be noticed a substantial improvement. While before  $g = 10$  was enough to reach instability, now the control remains stable even with  $g = 20$ , achieving good performances at least on the first two structural modes -  $86Hz$  and  $205Hz$ , while on higher order modes the magnitude reduction is slightly compromised since the reconstructed velocity is filtered at  $300Hz$ . The instability is reached with  $g = 30$ , simultaneously at low and high frequency. Indeed the high frequency noise is still present, although reduced. Moreover it has to be considered that in addition to the delay due to the filter, it is also present a fixed delay due to the fact that the control action provided to the plate is computed with the plate velocity of the previous time instant, therefore the control spillover is still possible even with a first order filter if the sampling frequency is too low.

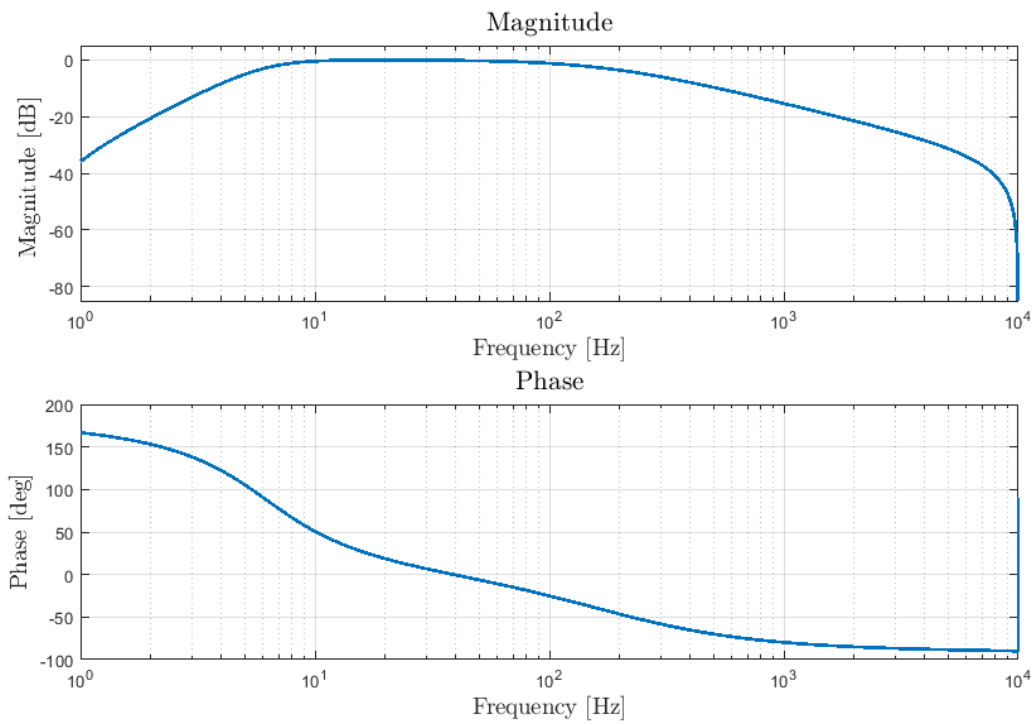


**Figure 5.21:** Bode plot of the band-pass filter, composed by a first order low-pass in addition to a second order high-pass.

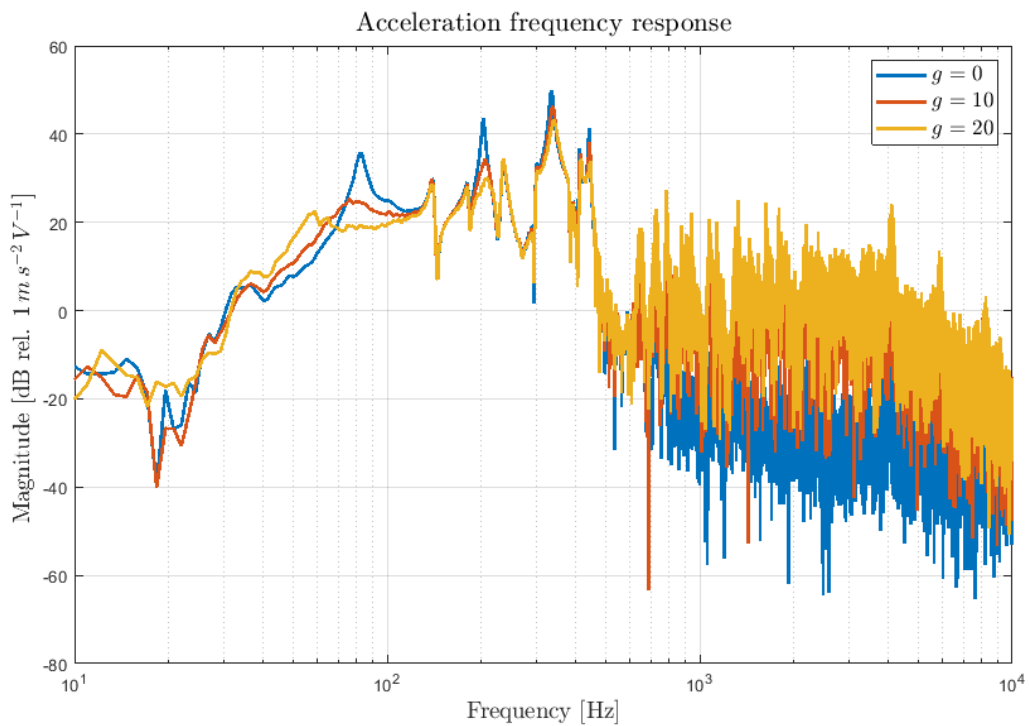


**Figure 5.22:** Acceleration frequency response with a first order filtering of current and voltage.

Given the awful resolution with which current and voltage are acquired, this can be considered a good result, and for sure gives clear indications on the direction that future works should take. In this last test the frequency separation between the filter's cutting frequency and the noise frequency was little more than a decade, if the noise were reduced by preconditioning of current and voltage it is straightforward that such separation could be reduced.



# Chapter 6

## Conclusions

The work presented in this thesis is intended as a preliminary study for the development of active devices based on the self-sensing inertial actuator concept, to be used to achieve vibroacoustic control of generic vibrating panels. The basic concept is to damp the vibration of a generic structure installing a device providing a control action proportional to the transverse structural velocity, obtaining a skyhook control system. The innovative idea is to derive an expression to reconstruct the transverse plate velocity and the inertial mass velocity adopting electrical measures only, without any need for accelerometers. The system is digitally implemented, looking toward future evolution in the direction of a multi-actuator decentralized control system that would greatly benefit from a digital implementation.

The first part of this work, described in Chapters 2 and 3, concerned the development of a mathematical model of the experimental setup, having a dual function. Firstly to allow the analytical derivation of an expression for the velocities, depending only on the voltage applied to the inertial device and on the current flowing in it, secondly to build models of the physical components - plate, power amplifier and vibration speaker - to be used to numerically simulate the experimental setup. The configuration under analysis is composed by a rectangular thin aluminum plate and a low cost vibration speaker used as inertial actuator, driven by a cheap power amplifier. The actuator is modelled as a simple mass-spring-damper system, whose parameters have been obtained through experiments on each device. Similarly a simple high-pass filter-like model, describing the power amplifier, has been obtained. The plate has been modelled at two levels of detail, firstly using a single degree of freedom model to gain some insight into the dynamic system under analysis, keeping as simple as possible the numerical simulation, secondly with a complete flexible description based on the S-GUF formulation, to analyze the system behaviour reproducing the real operating conditions.

The sensor-actuator expression for the velocity is based on the lumped parameter model of the inertial actuator, therefore suffers for any uncertainty of the model. In Chapter 4 the velocity reconstruction is tested numerically and some modifications are introduced, to solve stability related issues. The first problem is about one of the transfer functions not being proper. A static residualization of the actuator's electric dynamic is first proposed to reduce the order of the numerator, but this has led to even

worst results because of the high sensitivity of the reconstruction expression to non symmetric modifications of the transfer functions. Therefore the expression has been made proper by adding a pole at high frequency to both transfer functions. The second issue is the presence of two poles in the origin, solved moving the poles to the negative half of the complex plane. The final formulation gives a good reconstruction of the velocities - both transverse plate and inertial mass - in the frequency range of interest - 20Hz to 1kHz - keeping a good noise rejection outside.

The last part of this work was about the experimental testing of the sensor-actuator model. In Chapter 5 are discussed the results obtained digitally implementing the reconstruction of the velocity on a real-time skyhook control. The main problem concerned the resolution of the acquisition system, since the electrical quantities to be acquired oscillate with small amplitude around different baselines, the acquisition range has to be kept wide enough to acquire both, leading to a poor signal to noise ratio. Different filters has been introduced and tested to remove the noise at both low and high frequency. Good performances are obtained at low frequency, while high frequency filtering proved to be a challenging task. If the filtering action is too weak, the noise is not rejected and is amplified through the control gain. If it is too strong, the phase lag exceeded the phase margin, causing control spillover instability. If a first order low-pass filter is used, the stability of the control system is granted. Unfortunately the distance of the noise to be filtered from the frequency range of interest is not high enough to use a first order filter. A test has been presented where the working band of the control system has been limited to 300Hz, demonstrating that the first order filter gives indeed far better performances.

## 6.1 Future work

A lot of work has yet to be done on the self-sensing model of the actuator, before achieving the same performances that can be obtained with a sensor/actuator collocated pair. The numerical analysis demonstrated that, with the proposed modification to the reconstruction's transfer functions, stability can be theoretically achieved even in non ideal conditions. However, the real-time testing performed with a partially inadequate acquisition method showed how any segment of the control system, and not only the reconstruction equation, is vital to achieve good performances. In particular, the signal to noise ratio in the acquired quantities plays a primary role in the good reconstruction of the velocity. Therefore in future works more efforts shall be made in its improvement. In almost all reference works about sensor-actuators, a fully analogical control system was used. Of course moving to a similar architecture could greatly improve the signal to noise ratio, since it would remove its main source, the digital conversion. However, for the premises on the device that is being designed, a fully analogical approach could introduce great hardware complexity if a multi actuator decentralized architecture or more complex control logic were to be considered for future developments. A compromise solution could be to keep a digital implementation for the velocity reconstruction and for the feedback loops, while introducing an analog preconditioning of the signals to be acquired. In this way the acquisition of current and voltage could be made with a far better resolution while keeping the hardware

---

complexity independent on the control logic adopted. An example of a preconditioning circuit for current and voltage can be find in [33], where the current and voltage channels are preamplified in order to better exploit the resolution of the acquisition system. If a good enough signal to noise ratio were obtained, it might not even be necessary anymore the high frequency filtering presented in Chapter 5, or at least should be enough to use a first order filter as proposed in the last test.



# Bibliography

- [1] R. Kim, L. Fritschi, A. Brown, D. Schewla, and S. Kephelopoulos., "Burden of disease from environmental noise," in *Tech. rep. World Health Organization*, 2011. 1
- [2] E. Kerns, E. Masterson, C. Themann, and G. M. Calvert, "Cardiovascular conditions, hearing difficulty, and occupational noise exposure within us industries and occupations," *American Journal of Industrial Medicine* 61.6, pp. 477–491, 03/12/2018. 1
- [3] T. Münzel, F. Schmidt, S. Steven, J. Herzog, A. Daiber, , and M. Sørensen, "Environmental noise and the cardiovascular system," *Journal of the American College of Cardiology* 71.6, pp. 688–697, 2018. 1
- [4] K. Genuit, "Vehicle interior noise – combination of sound, vibration and interactivity," in *Head acoustic GmbH, Sound and Vibrations*, 2009. 1
- [5] D. Mead, *Passive Vibration Control*. John Wiley, 1998. 1
- [6] F. Fahy, *Fundamentals of noise and vibration control*. E FN Spon London, 1998. 1
- [7] F. Fahy and JohnWalker, *Advanced applications in acoustics, noise and vibration*. CRC Press, 2004. 1
- [8] P. Gardonio, "Review of active techniques for aerospace vibro-acoustic control," *Journal of Aircraft* 39.2, pp. 206–214, 04/12/2018. 1
- [9] R. Boulandet, A. Pelletier, P. Micheau, and A. Berry, "Active vibration control using self-sensing actuators: an experimental comparison of piezoelectric and electromagnetic technologies," in *Proc. of the ASME 2014 International Mechanical Engineering Congress Exposition*, (Montréal, Canada), November 14-20 2014. 1, 3, 14
- [10] R. Boulandet, M. Michau, P. Micheau, and A. Berry, "Aircraft panel with sensorless active sound power reduction capabilities through virtual mechanical impedances," *Journal of Sound and Vibration* 361, pp. 2–19, 2016. 1, 3, 14
- [11] D. D. Girolamo, "Active damping controllers with proof-mass electrodynamic actuators: design, analysis and experiments," Master's thesis, Politecnico di Milano, April 2018. 2, 18, 29, 37, 46, 50, 52, 53, 54, 95

- [12] P. Gardonio, "Smart panel with multiple decentralized units for the control of sound transmission. part i: theoretical predictions," *Journal of Sound and Vibration* 274, pp. 163–192, July 2004. 2
- [13] F. Fahy and J. Walker, *Fundamentals of Noise and Vibration*. E FN SPON, 1998. 3
- [14] W. P. Engels, O. N. Baumann, S. J. Elliott, and R. Fraanje, "Centralized and decentralized control of structural vibration and sound radiation," *Journal of the Acoustical Society of America* 119, 2006. 3
- [15] M. Baudry, P. Micheau, and A. Berry, "Decentralized harmonic active vibration control of a flexible plate using piezoelectric actuator–sensor pairs," *Journal of the Acoustical Society of America* 119, 2006. 3
- [16] M. J. Balas, "Direct velocity feedback control of large space structures," *Journal of Guidance, Control, and Dynamics*, 1979. 3
- [17] S. J. Elliott, P. Gardonio, T. C. Sors, and M. J. Brennan, "Active vibroacoustic control with multiple local feedback loops," *The Journal of the Acoustical Society of America*, 2002. 3
- [18] P. Gardonio, E. Bianchi, and S. Elliott, "Smart panel with multiple decentralized units for the control of sound transmission. part i: theoretical predictions," *Journal of sound and vibration*, 2004. 3
- [19] P. Gardonio, E. Bianchi, and S. Elliott, "Smart panel with multiple decentralized units for the control of sound transmission. part ii: design of the decentralized control units," *Journal of sound and vibration*, 2004. 3
- [20] P. Gardonio, E. Bianchi, and S. Elliott, "Smart panel with multiple decentralized units for the control of sound transmission. part iii: control system implementation," *Journal of sound and vibration*, 2004. 3
- [21] N. W. Hagood and E. H. Anderson, "Simultaneous sensing and actuation using piezoelectric materials," in *Proc. SPIE 1543 Active and adaptive optical components*, 1991. 3
- [22] J. J. Dosch, D. J. Inman, and E. Garcia, "Self-sensing piezoelectric actuator for collocated control," *J. of Intel. Mat. Syst. and Struct.*, 1992. 3
- [23] J. S. Vipperman and R. L. Clark, "Implementation of an adaptive piezoelectric sensor/actuator," *Am. Inst. of Aeronautics and Astronautics*, 1996. 3
- [24] J. S. Vipperman and R. L. Clark, "Multivariable feedback active structural acoustic control using adaptive piezoelectric sensor/actuators," *J. Acoust. Soc. Am.*, 1999. 3
- [25] S. O. R. Moheimani, "A survey of recent innovations in vibration damping and control using shunted piezoelectric transducers," *IEEE Trans. Control Syst. Tech.*, 2003. 3
- [26] D. Leo and D. Limpert, "A self-sensing technique for active acoustic attenuation," *Journal Sound and Vibration*, 2000. 3

- [27] B. Hanson and M. Levesley, "Self-sensing applications for electromagnetic actuators," *Sensors and Actuators A: Physical*, 2004. 3
- [28] A. Pelletier, P. Micheau, and A. Berry, "Harmonic active vibration control using piezoelectric self-sensing actuation with complete digital compensation," *Journal of Intelligent Material Systems and Structures*, November 2017. 3
- [29] A. Preumont, *Mechatronics - Dynamics of Electromechanical and Piezoelectric Systems*. Springer, 2006. 6
- [30] H. Olson, *Music, Physics and Engineering*. Dover Publications, 1967. 19
- [31] M. D'Ottavio, L. Dozio, R. Vescovini, and O. Polit., "The ritz – sublaminated generalized unified formulation approach for piezoelectric composite plates," *International Journal of Smart and Nano Materials* 9.1, pp. 34–55, 2018. 19
- [32] O. Faccini, "Vibroacoustic control of plates with self-tuning decentralized feedback loops," Master's thesis, Politecnico di Milano, 2018. 46, 53
- [33] F. Romani, "Power consumption analysis of an electromechanical inertial mass actuator using a custom designed measurement board," Master's thesis, Università di Pisa, 2017. 103